MODELING OF PLASMA DYNAMICS DURING PULSED ELECTRON BEAM ABLATION OF GRAPHITE

by

Muddassir Ali

A thesis submitted in partial fulfillment
of the requirements for the degree of
Doctor of Philosophy (PhD) in Natural Resources Engineering

The Faculty of Graduate Studies
Laurentian University
Sudbury, Ontario, Canada

THESIS DEFENCE COMMITTEE/COMITÉ DE SOUTENANCE DE THÈSE
Laurentian Université/Université Laurentienne
Faculty of Graduate Studies/Faculté des études supérieures

Title of Thesis Titre de la thèse	MODELING OF PLASMA DYNAMICS DURING PULSED ELECTRON BEAM ABLATION OF GRAPHITE
Name of Candidate Nom du candidat	Ali, Muddassir
Degree Diplôme	Doctor of Philosophy
Department/Program Département/Programme	Natural Resources Engineering
Date of Defence Date de la soutenance	July 26, 2017

APPROVED/APPROUVÉ

Thesis Examiners/Examinateurs de thèse:

Dr. Redhouane Henda
(Supervisor/Directeur(trice) de thèse)

Dr. John Ashley Scott
(Committee member/Membre du comité)

Dr. Andrew McDonald
(Committee member/Membre du comité)

Dr. Brahim Chebbi
(Committee member/Membre du comité)

Dr. John Preston
(External Examiner/Examinateur externe)

Dr. Mohamed Azzouz
(Internal Examiner/Examinateur interne)

Approved for the Faculty of Graduate Studies
Approuvé pour la Faculté des études supérieures
Dr. David Lesbarrères
Monsieur David Lesbarrères
Dean, Faculty of Graduate Studies
Doyen, Faculté des études supérieures

ACCESSIBILITY CLAUSE AND PERMISSION TO USE

Abstract

Recent advances in the field of plasma nanofabrication suggest that plasma-based technologies may replace many of the conventional chemical and thermal routes in the synthesis of nanomaterials (with at least one dimension below 100 nm) and thin films. In contrast to the conventional processing routes, where only neutral species are involved, a plasma is made up of energetic species including ions, electrons, and excited molecules in addition to neutrals. Due to the highly energetic nature of interactions among these species and with other surfaces (substrates), a plasma allows for the formation of materials at higher rates even though their concentrations might be low as compared with those of neutral species in non-plasma based methods. While the mechanisms of the various interactions in a plasma are undoubtedly complex and require a fundamental understanding, they offer new opportunities for material nanofabrication.

Pulsed electron beam ablation (PEBA) has recently emerged as a novel and promising technique for high quality thin films growth. Pulsed electron beam film deposition consists of many physical processes including target material heating, target ablation, plasma plume expansion, and film growth on a substrate. Electron beam ablation is a complex process, which comprises heating, phase change, and removal of a fine fraction from the target surface. Ablation strongly affects the space distribution, composition, mass transfer processes, which in turn has a critical bearing on the structure, stoichiometry and properties of thin films. Plasma plume expansion into an ambient gas is a fundamental issue in PEBA as the quality of thin films deposited onto the substrate depends on the composition, energy and density of particles ejected from the target.

A one-dimensional heat conduction model is presented to investigate the heating and ablation of a graphite target upon interaction with a polyenergetic electron beam. The effect of electron beam

efficiency, power density, accelerating voltage, and Knudsen layer just above the target surface during ablation are taken into account in the model. Phase transition induced during ablation is considered through the temperature dependent thermodynamic properties of graphite. The temperature distribution, surface receding velocity, melting depth, ablation depth, and ablated mass per unit area are numerically simulated. Upon ablation, plasma expansion, induced by interaction of a nanosecond electron beam pulse (~100 ns) with a graphite target in an argon atmosphere at reduced pressure, was investigated by solving gas-dynamics equations. The spatio-temporal profiles of the temperature, pressure, velocity, and density of the plasma plume are numerically simulated for a beam efficiency of 0.6 and accelerating voltage of 15 kV. Each model is validated by comparing some of the obtained simulation results with experimental data available in the literature.

Acknowledgements

All praise is due to God Almighty, the creator of all human beings, source of all knowledge and wisdom. He is the one who provided me potential, courage and hope for achieving the destination.

My deepest gratitude and appreciation goes to my respected supervisor Dr. Redhouane Henda for giving me an opportunity to work on this novel research project. While this project has been quite a challenging endeavor, it has offered me unique learning opportunities. My supervisor's inspiring guidance, remarkable suggestions, constant encouragement and friendly discussions have enabled me to bring this project to fruition. I am highly grateful to him for his critical assessment of the reports, manuscripts of research articles, and thesis, and for suggesting several beneficial improvements. I am blessed to have had the privilege and honour of working under his supervision.

I would like to appreciate other committee members of my doctoral degree for their critical assessment of my comprehensive examination reports and thesis, and for providing professional advice. Furthermore, I would also like to acknowledge the persistent help of the graduate coordinators throughout my doctoral program.

I would as well like to thank you all my colleagues at the laboratory and university for their continuous support, inspiration and beneficial guidance during these years.

Last but not least, I wish to express my sincere gratitude to my parents for providing me financial and moral support throughout these years. They made several sacrifices in accomplishing this milestone and were constantly there to provide necessary help and assistance. It provides me immense honour and privilege to dedicate this thesis to them.

Table of Contents

List of Tables

List of Figures

List of Symbols

A	atomic weight of the target material (g/mol)
C_p	specific heat capacity of the target material $(J/kg\ K)$
C_{p_l}	liquid phase specific heat capacity of the target material $(J/kg\ K)$
C_{p_s}	solid phase specific heat capacity of the target material $(J/kg\ K)$
C_{p_v}	vapor phase specific heat capacity of the target material $(J/kg\ K)$
c	thermal expansion along the c-axis (Å)
D	diffusion coefficient of the liquid (m^2/s)
d	distance between the beam tube output and target surface (mm)
d_b	diameter of the beam (m)
d_l	distance between two adjacent crystalline layers (Å)
d_p	diameter of target particle in the ablated plume (m)
f	fraction of collisions among the crystal
E	instantaneous electron energy (eV)
$E_{A,B,C}$	average energy for each group of electrons (keV)
E_p	total specific energy of the ablated plume (J/kg)
e	elementary electric charge (C)
e_o	charge of an electron (C)
g_0	degeneracy factors of a neutral atoms
g_1	degeneracy factors of a singly ionized (C^+)
g_2	degeneracy factors of a doubly ionized atoms (C^{2+})
$h_{A,B,C}$	most probable penetration depth by each group of electrons (m)
$I_{A,B,C}$	beam current for each group of electrons (A)
IP_1	first ionization energy of carbon (eV)
IP_2	second ionization energy of carbon (eV)
J	mean ionization energy (eV)
k	thermal conductivity of the target material $(W/m\ K)$
k_a	thermal conductivity of the target material along the a-axis $(W/m\ K)$
k_B	Boltzmann constant (J/K)
k_c	thermal conductivity of the target material along the c-axis $(W/m\ K)$
k_l	liquid phase thermal conductivity of the target material $(W/m\ K)$
k_s	solid phase thermal conductivity of the target material $(W/m\ K)$
k_v	vapor phase thermal conductivity of the target material $(W/m\ K)$

k_z	variable depending only on Z
L	the characteristic length of the target material (m)
L_d	length of the heat diffusion (m)
L_m	latent heat of fusion (kJ/kg)
L_s	distance between target surface and substrate surface (m)
L_v	latent heat of vaporization (kJ/kg)
l	thickness of the target material (m)
l_e	mean-free path of the electrons (m)
M	Mach number
m	average mass of target particle (kg)
m_e	effective mass of the electron (kg)
N_A	Avogadro's number $(1/mol)$
N_D	Debye number
n_a	number density of neutral atoms $(1/m^3)$
n_e	number density of electrons $(1/m^3)$
n_i	number density of species i $(1/m^3)$
n_p	number density of the ablated plume $(1/m^3)$
P	total pressure of the ablated plume (Pa)
P_g	pressure of the background gas (Pa)
P_k	pressure of the particles leaving the Knudsen layer (Pa)
P_0	normal atmospheric pressure (Pa)
$P_s(T_s)$	saturated vapor pressure just above the target surface (Pa)
Q	heat source (W/m^3)
Q_A	activation energy of the atoms for diffusive motion in the liquid (kJ/kg)
Q_{ei}	effective electron-ion momentum transfer collision cross-section (m^3/s)
Q_S	surface power density delivered by the heat source (W/m^2)
q	heat flux due to conduction (W/m^2)
R_g	gas constant of the vapor $(J/kg\ K)$
r	radius of the beam spot on the target surface (m)
S_a	beam spot cross-sectional area on the target surface (m^2)
s	distance travelled along the electron trajectory (m)
T_b	boiling temperature under P_0 (K)
T_e	electron temperature (K)
T_k	temperature of the particles leaving the Knudsen layer (K)
T_m	melting temperature of the target material (K)

T_{mi}	melt interface temperature (K)
T_p	temperature of ablated plume (K)
T_{pt}	temperature of phase transition (K)
T_S	surface temperature (K)
T_{sb}	sublimation temperature of the target material (K)
t_m	time required by the target surface to attain the melting point (s)
t_{sb}	time required by the target surface to attain the sublimation point (s)
u	velocity of the ablated plume (m/s)
u_m	melting front velocity (m/s)
$u(t)$	surface recession velocity (m/s)
x	distance from the target surface along the incident beam direction (m)
x_e	partial fraction of electrons in ablated plume
x_0	partial fraction of neutral atoms
x_1	partial fraction of singly charged ions (C^+)
x_2	partial fraction of doubly charged ions (C^{2+})
Z	atomic number of the target material
Z_i	charge state of species i

Greek letters

α	Degree of ionization
α_s	Solid phase thermal diffusivity of the target material (m^2/s)
β	Back flux coefficient
ΔE	Highest energy value for the considered electronic transitions (eV)
$\mathcal{E}$	Specific internal energy (J/kg)
ϵ	Electric field (V/m)
ε_0	Permittivity of free space (F/m)
γ_v	Specific heat ratio
κ_p	Thermal conductivity of the ablated plume particles $(W/m\ K)$
κ_e	Thermal conductivity of the electrons $(W/m\ K)$
η	Efficiency factor
Λ	Average length of the diffusive jump of atoms in the liquid (Å)
Λ_i	Coulomb logarithm of species i
λ_D	Debye length (m)
μ_m	Kinetic melting coefficient $(m/s\ K)$

μ_p	Viscosity of the ions and atoms in the ablated plume (kg/ms)
$\bar{\nu}$	Effective electron collision frequency $(1/s)$
ν_D	Frequency of atoms on the order of the Debye frequency $(1/s)$
ν_e	Speed of electrons (m/s)
ρ	Density of the target material (kg/m^3)
ρ_g	Density of the background gas (kg/m^3)
ρ_k	Density of the particles leaving the Knudsen layer (kg/m^3)
ρ_l	Liquid phase density of the target material (kg/m^3)
ρ_p	Overall density of the ablated plume (kg/m^3)
ρ_s	Solid phase density of the target material (kg/m^3)
ρ_v	Vapor phase density of the target material (kg/m^3)
σ	Electrical conductivity $(1/\Omega m)$
τ	Duration of the electron beam pulse (s)
$\bar{\bar{\tau}}$	Viscous shear stress tensor (Pa)
τ_e	Relaxation time (s)

Subscript

A	Group A electrons
a	Neutral atoms
B	Group B electrons
C	Group C electrons
D	Debye
e	Electrons
l	Liquid phase of the target material
m	Melting
mi	Melting interface
S	Target surface
s	Solid phase of the target material
v	Vaporization

List of Abbreviations

AES	Auger Electron Spectroscopy
BSE	Backscattered Electrons
BTE	Boltzmann Transport Equation
CS	Channel-spark
FEM	Finite Element Method
FWHM	Full Width at Half Maximum
IB	Inverse Bremsstrahlung
KL	Knudsen layer
LTE	Local thermal equilibrium
MC	Monte Carlo
OES	Optical Emission Spectroscopy
PEBA	Pulsed Electron Beam Ablation
PEBS	Pulsed Electron Beam Source
PI	Photoionization
PLA	Pulsed Laser Ablation
SEM	Scanning Electron Microscopy
SE	Secondary Electrons
TEM	Transmission Electron Microscopy
THC	Transient Hollow Cathode

Chapter 1

1 Introduction

1.1 Background

A layer of material thickness ranging from a few nanometers to a few micrometers is known as "thin film". Thin films possess very unique properties when compared with those of the bulk materials from which they are synthesized. This is mostly due to strong interfacial effects and the fact that their properties depend on the technique of preparation. Unique properties that thin films exhibit are mainly due to atomic growth process and size effects, including with quantum size effects, characterized by multilayer, crystalline orientation, and thickness aspects. Thin films have gained importance and significance in a variety of technologically important industrial applications (Figure 1.1). Examples include wear- and corrosion-resistant coatings, which have the ability to extend the life duration of a large number of products and devices; electrically and optically active coatings as well as magnetic thin films, which can be conveniently engaged in sensors and actuators; photovoltaic cells, which are capable of generating solar energy; bio-medical coatings, which are used as replacements for damaged tissue; and chemically-active coatings, which can find use as nano-catalysts. Graphite is one of the natural occurring allotropes of carbon, which exhibits excellent heat conductive properties, high strength to density ratio at high temperatures, and capacity to absorb energy in large amounts without fracturing or melting. In recent years, graphite has received a considerable amount of attention as a key material in the area of sustainable technologies, such as photovoltaics, fuel cell, electric automobiles, and energy storage (Chung, 2002; Mantell, 1968; Pappis and Blum, 1961; Pierson, 1994).

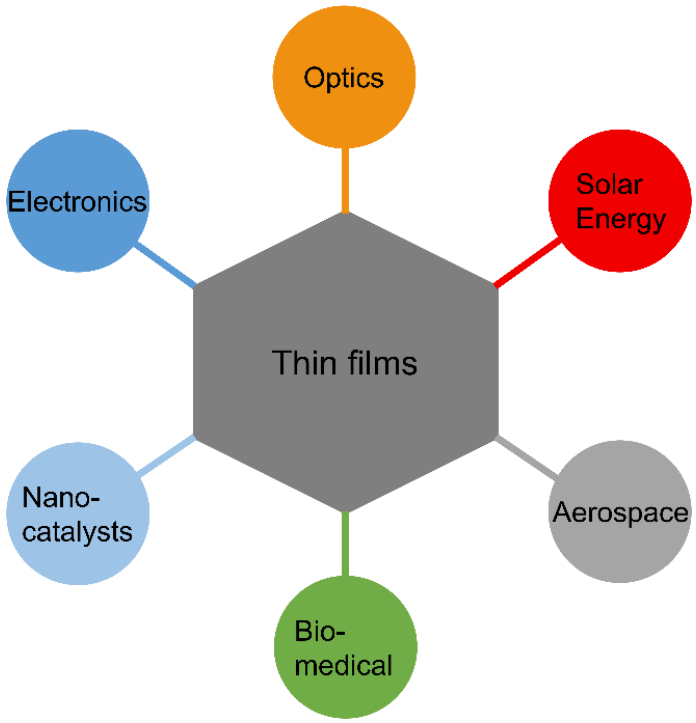

Figure 1.1: Major technological applications of thin films.

Bombardment of a material surface by energetic particles for thin film deposition is a well-established phenomenon. In 1938, for the first time, surface bombardment was put forward for film density improvement (Strikovski et al., 2010). A few decades later, this energetic particle process has evolved into what is known as ion plating (Mattox and McDonald, 1963). Ever since, numerous methods have been developed to generate highly energetic process conditions. These methods consist of magnetron sputtering, plasma-assisted film deposition methods, and ion-beam-assisted deposition (Colligon, 1995). In all these energetic condensation processes, a common associated factor is that the surface of film deposition is under continuous bombardment by an energetic particle stream as it receives the required material for film deposition (Figure 1.2).

Electron beams are extensively functional in numerous application areas as technological tools. In the field of materials science and engineering, electron beams are mainly engaged in three areas,

which include analysis of materials (via AES, TEM, SEM, etc.), surface modification of materials (Zou et al., 2006), and growth of thin films (Nakanishi et al., 1999). Although surface characterization may employ intense electron sources and has triggered much research into the investigation of the interactions of an electron beam with solid materials, deposition of thin films aided by an electron beam is still restricted to a few preparation methods. This seems to be due to two main causes: first, the technology involves complex processes, and, second, it is difficult to develop an electron beam that is adequately intense and stable to be beneficial in materials processing. Just over a decade ago, a new kind of discharge (channel spark) was developed and has allowed the production of very powerful pulsed electron beams.

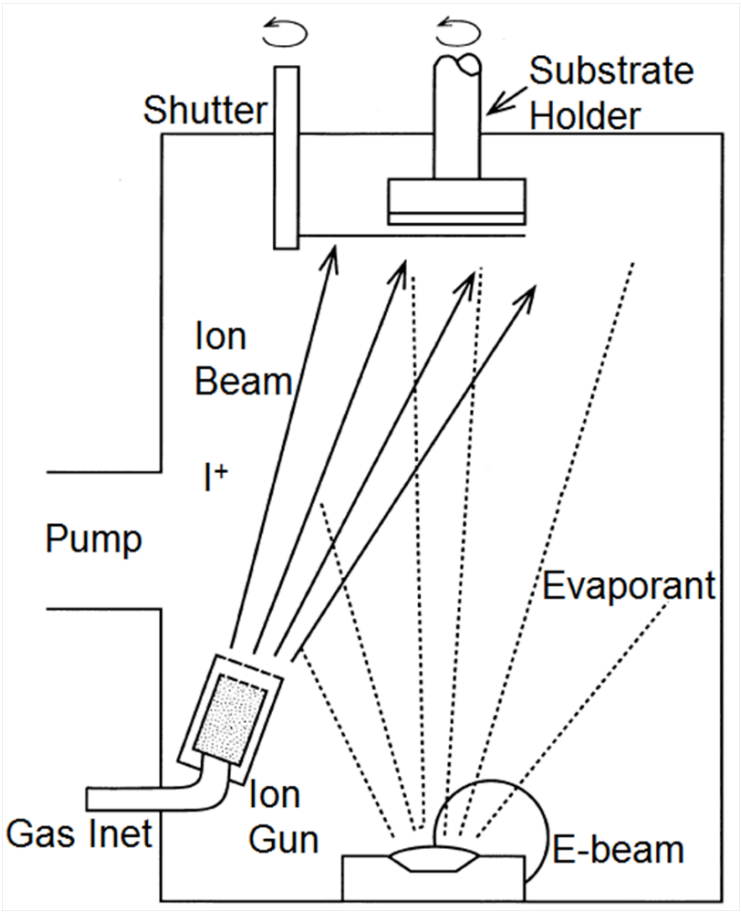

Figure 1.2: A schematic illustration of a conventional vacuum-based ion plating process. (Reprinted with permission from: Mattox, 2000. © 2000, Elsevier.)

Just over a decade ago, a new kind of discharge (channel spark) was developed and has allowed the production of very powerful pulsed electron beams. The discharge is generated inside a transient hollow cathode and the beam is channelled out via a dielectric channel in the direction of the anode. This type of discharge generates a powerful pulse (a few 100 A in electron beam current) of mid-energetic electrons (< 20 keV) to be concentrated over a few tens of nanoseconds on a small spot (~mm^2) of a target surface. These beam properties give rise to a very high volume of power (~10 MW) delivered to the target surface, almost similar to what has been observed in the well-established deposition method of target surface ablation, specifically, pulsed laser ablation (PLA) (Venkatesan et al., 2005). These similitudes have prompted the employment of these discharges for the ablation of a material target to grow high quality thin films. By similarity, the channel-spark-based method is known as pulsed electron beam ablation (PEBA) (Müller et al., 1995).

A pulsed laser in PLA quickly vaporizes a fine portion of a target material, giving an energetic plasma flux stream under extremely non-equilibrium conditions. This non-equilibrium erosion of

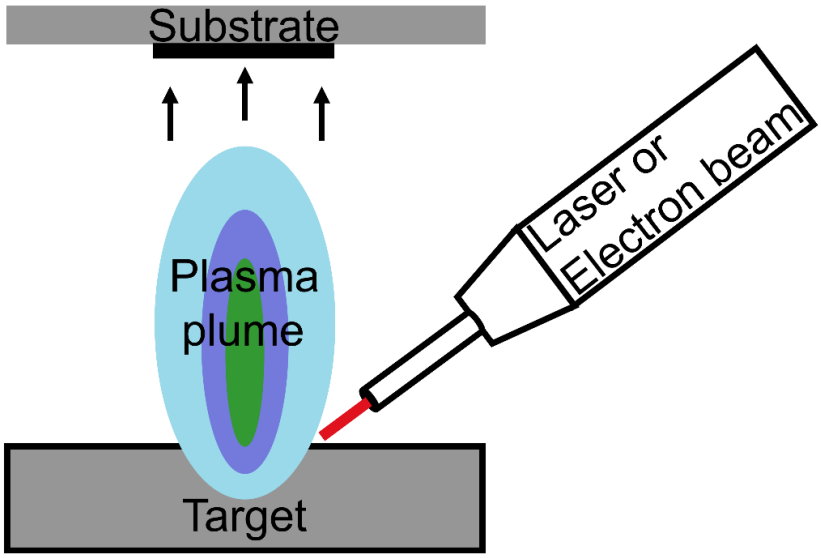

Figure 1.3: Schematic illustration of pulsed laser/electron beam ablation process.

material is known as ablation. Conditions involved in thin film growth are intricately associated with and governed by the conditions of the plasma flux formation and its expansion in a process background gas. The overall physics and ablation mechanism in PEBA is very similar to those in PLA, however, a substantial difference exists in the nature of the pulse energy source and of the interactions of the energetic beam with the target and expanding plasma. The energy for ablation in PEBA process is supplied to the surface of a target by pulsed electrons instead of photons as in PLA. The fundamental mechanisms underpinning the interactions of the electron beam with a target as well as with the evaporant it produces have subtle differences with the mechanisms of photon-matter interactions (Strikovski et al., 2010). In both cases, i.e., by the pulsed laser beam and the pulsed electron beam, a dense plasma is generated at the target surface. The principal precursor material for thin film growth is this highly dense plasma. The thick, strongly ionized, and high temperature plasma flux stream above the target surface expanding in a vertical direction to the target surface is known as the plasma plume. A schematic representation of the pulsed laser/electron beam ablation process is shown in Figure 1.3. Though PLA is a well-established technique, PEBA is still a developing technology.

It is well-recognized that PEBA has recently emerged as a potential substitute for PLA as a powerful technique for the fabrication of thin films (Jiang et al., 1994; Muller et al., 1995). PEBA technique presents many promising advantages over PLA. Among these are the high electrical-electrical efficiency (~30%), efficient energy absorption for all materials (even materials that are transparent or reflecting to photons), relatively safe compared to excimer lasers (no formation or risks of leaks of toxic gases, such as F or Cl), and low capital cost of electron beam generator compared to lasers (Gilgenbach et al., 1999; Kovaleski et al., 1998; Müller et al., 1995). Growth of thin films via this technique is a complex phenomenon, which goes through many fundamental

processes all the way from the generation of intense electron pulses to the irradiation of a target material to the ablation and transfer of the material in the form of a plasma plume to a substrate through expansion in a background gas. The key processes responsible for the growth of thin films during PEBA are electron beam ablation of a target material and plasma plume expansion in a background gas towards a substrate. Electron beam ablation is one of the most crucial stages to preserve fabricated films stoichiometry relatively to ablated target. The plasma plume expansion is also an important stage since the characteristics of the fabricated films are critically dependent on the nature and energy of the ablated particles. Although PEBA technique has been extensively applied over the past few years, there is still no complete model to account for the fundamental processes, which are directly involved in the deposition of thin films. Therefore, comprehensive mathematical models for the ablation of a target surface and expansion of plasma plume in a background gas are required in order to fully understand the complex deposition process and eventually optimize and control the relevant deposition parameters in PEBA.

1.2 Literature Review

1.2.1 Modeling of Pulsed Energy Beam Ablation

In PLA, when the solid surface of the target is hit by a high power density laser beam, the target surface absorbs the energy and a sudden rise of temperature ensues, leading to a rapid ablation of the target material and the generation of a plasma plume. The consistency of this process crucially depends on the amount of energy absorbed by the broadening plasma plume (so called shielding effect). Assuming there is no absorption by the expanding plasma, the ablation front goes deeper beneath the target surface with a velocity proportional to the intensity of the beam. On the other hand, if entirely absorbed by the plasma plume (via inelastic free electron scattering), the beam cannot reach below the target surface to carry out further evaporation. When the plasma initially

propagates away from the target surface, the density of free electrons decreases, the plasma turns transparent and the beam can again interact with the target surface. These issues are generally encountered in PLA due to two major reasons. The first reason is that the quantity of ablated material depends on the optical absorption coefficient (penetration depth of the laser beam before it has dissipated) of the target material at the specified laser wavelength. The other reason is that the beam may not interact with the target surface effectively because the plasma plume acts as a shield in front of the target and absorbs a significant amount of energy from the beam. The plasma plume shielding effect can strongly affect the dynamics of ablation and the spectrum of energy distribution of the particles of the plasma plume (Harshavardhan and Strikovski, 2005).

In the case of PEBA, the ablation stage is not influenced by the target material optical properties due to the nature of the mechanism of electron beam-target interactions. In PEBA, the preliminary heating of the target surface to the ablation temperature is governed by the energy balance on the target by taking into account the rates of heat in and out, energy dissipation, and thermal conductance of the target material. In this regard, the absorption depth of the electron beam plays a vital role. The electron beam striking the target surface loses energy by inelastic collisions between the electrons of the beam and target atoms, leading to high surface temperature via heat conduction. After a short journey (a few micrometers) inside the target, Coulomb scattering is experienced by the energetic electrons, and the latter tend to diffuse into the material, instead of continuing in a linear path. The consequence of this effect helps in restricting the entire dissipated energy of beam to within about 1-2 μm layer of surface. Electron ablation exhibits a peculiar characteristic during the electron-target atoms interaction. Beam electrons interact with target atoms effectively, regardless whether they are in solid or vapor state. Therefore, the effective cross section for electron scattering by the target atom does not alter before or after ablation stage. In

this case, if the beam has adequate intensity, all the target material within surface layer of 1-2 μm can be ablated (Harshavardhan and Strikovski, 2005; Tricot et al., 2010). This phenomenon is slightly different from PLA, where shielding of the plasma plume controls the quantity of ablated material.

Most of the work on the modeling of plasma dynamics for pulsed energy ablation is related to PLA. A wide range of publications on the mathematical models for laser heating of a target, laser ablation of a target and plasma plume expansion in a background gas have been reported in the literature. Such works can be a good starting point in the development of realistic models to describe PEBA processes.

1.2.1.1 Laser Beam Ablation

Several researchers have modeled the laser ablation process for different pulse durations, laser intensities, laser wavelengths, target materials (metals, polymers, ceramics, etc.) and under different process conditions. As mentioned before, it is understood that the ablation process involves complex heat and mass transfer mechanisms.

In the vast number of the studies, researchers have modeled the ablation stage for a length of time equal to one single pulse. They have used the classical heat conduction equation as the principal equation of heat transfer to predict the variation of temperature in the target. They have evaluated melting and vaporization, and, subsequently, estimated the ablation rate. Using this approach Baeri et al. (1979) and Wood and Giles (1981) have modeled the melting of the target surface. Ablation was estimated by considering evaporation of the top target surface by Dabby and Paek (1972). Singh and Narayan (1990) and Singh (1990) proposed a model, which is based on a simple energy balance to predict the amount of material evaporated per pulse. In this model, the energy required

to vaporize the metal surface, losses due to conduction in the target and losses as a result of absorption by the plasma were equated to the energy deposited by the laser beam. This model was helpful to predict the average ablation rate as a result of a single incident pulse. Bhattacharya et al. (1991) modeled laser-target interaction to predict the ablation rate by considering an energy balance at the target interface.

All the previously mentioned models have not considered the downward movement (receding) of the top surface which occurs due to material ablation. Peterlongo et al. (1994) have included this in their model by selecting a reference frame moving with the ablated target surface. In their model, they have estimated the ablation rate of the top surface by assuming that the flow of vaporized material follows the Hertz–Knudsen equation and the vapor pressure above the vaporized surface can be evaluated with the classical Clausius–Clapeyron equation. Tokarev et al. (1995), Neamtu et al. (1999) and Bulgakova & Bulgakov (2001) have used similar approaches in their models to predict the amount of material ablated from the target surface. Bulgakova et al. (2004) have further modified their model (Bulgakova & Bulgakov, 2001) by considering the latent heat of fusion. Based on the concept of latent heat of fusion, few other models were developed by Stafe et al. (2007), Rozman et al. (2008), and Aghaei et al. (2008) to simulate ablation of the solids. Stafe et al. (2007), in addition to considering the material ablation by vaporization, have also included the ablation of the molten phase due to force exerted by the plasma pressure. It is important to mention here that all of the above models do not consider the shielding effect that influences the incoming laser beam after the expansion of plasma.

In PLA, shielding plays a key role as it strongly affects the energy balance during ablation. Fang et al. (2008) have proposed an improved two stage one-dimensional thermal model for UV-high – power nanosecond PLA. Two heat conduction equations are used to model solid and liquid phases

separately based on melting time interval. In the first stage, the heat equation accounts for heating of the solid target surface before it starts to melt. In the second stage, the heat equation with moving evaporation front accounts for the target surface (liquid phase) exceeding the melting temperature and surface vaporization effect after melting starts to take place. This model also includes plasma shielding effects, temperature dependent absorptivity, and absorption coefficient of target material. Based on all of the above, our proposed model will borrow from the more complete PLA models and add a proper expression for the heat source term.

1.2.1.2 Electron Beam Ablation

Electron beam ablation of a target material is quite a complex physical process and takes place in a sequence of phenomena. This sequence comprises several physical steps starting with rapid heating, melting/sublimation, and vaporization of the target surface. The electron beam ablation strongly affects the space distribution, composition, mass transfer processes, and ablation rate of the target material, which in turn have a critical bearing on the structure, stoichiometry and properties of thin films. A few models have been previously developed to predict the target temperature for electron beam interaction with solid materials (Akamatsu and Yatsuzuka, 2003; Kowalewicz and Redel, 1995; Markov and Rotshtein, 1997; Proskurovsky et al., 1998; Qin et al., 2004; Tricot et al., 2010).

Markov and Rotshtein (1997) have calculated thermal fields induced during high-current pulsed electron beam using a one-dimensional model, by considering phase transition during beam irradiation, temperature-independent thermo-physical properties, and constant heating source power density during the entire pulse width. The movement of the evaporation front is introduced in the boundary condition to estimate the thickness of the evaporated layer. Proskurovsky et al. (1998) have modeled the non-stationary temperature field of a solid as the result of electron beam

irradiation by solving an un-coupled set of one-dimensional equations of thermo-elasticity. When the evaporation phenomenon is neglected, the model tends to provide a precise description of the beam-affected conditions irradiated by a pulsed electron beam.

In their study, Akamatsu and Yatsuzuka (2003) have used a one-stage equation for thermal conduction to evaluate the temperature field by considering the target as a semi-infinite solid and constant beam density. Spatial and temporal dependence of the temperature for the titanium target was evaluated to calculate the cooling rate and the thickness of the treated surface. Qin et al. (2004) have simulated the temperature profiles of aluminum and steel by using a one-dimensional heat diffusion equation. Furthermore, they have also predicted initial melting positions, melting layer thickness and crater depth induced during high-current pulsed electron beam irradiation. All of the aforementioned models are based on high-current pulsed electron beams, which are mainly employed for surface modification. Electron beams used in all these studies are of monoenergetic nature. The source of electrons in the case of a pulsed electron beam engaged for thin films deposition is polyenergetic in nature (Kowalewicz and Redel, 1995; Witke et al., 1995; Witke et al., 1996). In an early attempt, Kowalewicz and Redel (1995) have proposed a model, which describes irradiation by a polyenergetic electron beam, energy dissipation via conduction and the effect of the vapor pressure of the ablated mass on the temperature of the target. Recently, Tricot et al. (2010) have suggested a simple model of heat conduction in a target irradiated by a polyenergetic pulsed electron beam, but does not include phase change during ablation. Therefore, both of these models do not account for the receding surface of the target during ablation.

1.2.2 Modeling of Plasma Plume Expansion

Erosion of particles from target surface by electron beam irradiation leads to the formation of a plasma plume expanding quickly away from the target material. The ablated particles are

subsequently deposited onto to a suitably positioned substrate as a thin film via condensation (film growth). The characteristics of the expanding plasma plume (density, composition, ionization degree, and temperature distribution) play an important role in defining the ultimate structure and morphology of the fabricated films. A plasma is overall electrically neutral and consists of electrons, ions and neutral atoms. It can be supposed to be in local thermodynamic equilibrium when $T_e = T_i = T_n = T$. Neutral atoms and ions are assumed to be present in large numbers and lying close to each other (ambipolar diffusion). Therefore, a local thermodynamic equilibrium of excited state species is easily achieved through collisions with electrons. The plasma plume expansion can be characterized by two regimes: (i) The ionization and plasma-heating phase in the presence of the beam; and (ii) The recombination phase corresponding to plasma cooling and relaxation after beam termination (Marla et al., 2011).

In PLA, investigations on plasma plume dynamics, its expansion and interaction with the laser beam, have been mostly carried out using gas-dynamics such as Knight (1979), Pert (1989), Singh and Narayan (1990), Singh et al. (1990), Anisimov et al. (1993), Peterlongo et al. (1994), Ho et al. (1995), Itina et al. (1998), Garrelie et al. (1998), Garrelie and Catherinot (1999), Garrelie et al. (1999), Neamtu et al. (1999), Itina et al. (2002), Itina et al. (2003), Stapleton et al. (2005); and Gusarov & Smurov (2005). The model equations have been solved by Monte Carlo schemes and the finite element method (FEM). The modeling of plasma expansion has been carried out by assuming the plasma to be an ideal gas. Plasma plume expansion is then described by the equations of conservation of mass, momentum and energy. Plasma dynamics in the first regime (plasma expansion in the presence of the beam) is not much different from the expansion in vacuum, since the driving force (plasma pressure ~ 1 kbar) is usually much higher than that of the low pressure background gas (< 1 mbar).

Knight (1979) proposed one of the first theoretical models for PLA plasma expansion in an ambient gas. His investigation was based on one-dimensional gas-dynamics for a transient, self-similar problem of steady mass flux with instantaneous vaporization. This study has included Knudsen's interface at the target surface, vapor-plume interface, and wave shock in the plume. Singh et al. (1990) have considered an anisotropic three-dimensional expansion of the laser-generated plasma, initially at high temperature and pressure. The model is based upon the generation of high-pressure gaseous plasma confined in small dimensions, which is suddenly allowed to expand in vacuum. They have assumed plasma expansion to be isothermal in the presence of the laser beam and adiabatic in its absence, i.e., between two successive pulses. In their model, Anisimov at al. (1993) have assumed the initial plasma plume to be distributed in a semi-ellipsoid form just over the target surface with the base area being the same as the beam width and the height is calculated as the distance covered by the plasma plume in a time equal to the pulse duration. They have also assumed expansion to be adiabatic after pulse termination. Anisimov et al. (1996), in another study, have employed the gas-dynamics equations to model plume expansion in PLA in vacuum and under the presence of a background gas.

One of the comprehensive theoretical models to study laser produced plasma plume in a background gas environment was presented by Bulgakov and Bulgakova (1995). A gas dynamic model was developed to predict the spatial and temporal distribution of the plasma plume propagating into an ambient gas under a pressure limited to few pascals. This study is based on the formation of a spherical plasma plume whose propagation is explained by two-temperature approximations using Euler equations. Simulation results show that the plume does not cease upon reaching the maximum propagation distance, however, moves frequently back and forth up to 200 μs after ablation. Ho et al. (1995) have modeled the plasma expansion process into an ambient gas

using a compressible fluid dynamics approach. The model captures shock waves induced during the interaction of plume and ambient gas and shows the presence of shock wave discontinuities in the microsecond range for gas pressure less than 10^{-2} atm. The shock waves cannot survive, if gas pressure is greater than 0.1 atm. Neamtu et al. (1999) have used Monte Carlo simulations to evaluate the expansion of the plasma plume from a target surface to the substrate surface. The space and time distributions of the main plasma parameters (e.g., atom density, electron temperature and density of plasma) have been evaluated. Aside from this, their model also takes into account the interaction of plasma with the ambient gas. Stapleton et al. (2005) have included the kinetics of electrons, ions and neutral atoms in the modeling of the plasma dynamics, together with gas-dynamics. The numerical simulations have shown that the plasma recoil pressure has significant effects on plasma dynamics. Plasma dynamics was strongly influenced by the laser wavelength. Simulation results have shown that the expansion is isothermal and isentropic for a laser spot size on the target above 50 μm.

Expansion of plasma plume as well as its interaction with a background gas in the second regime (plasma expansion after beam termination) is by far a more complicated gas-dynamic process due to the occurrence of many physical processes, such as attenuation, deceleration, thermalization of ablated species, diffusion, recombination, and shock waves formation (Aggoune et al., 2010). The most complete model for a plume expansion in an ambient gas is the one due to Arnold et al. (1999), who have treated a specific case with a system of equations for the motion of the plume, an internal shock wave moving towards the center of plume, and an external shock wave moving in front of the contact surface and the background gas. This model is based on the analytical solution of a simplified form of the gas dynamics equations. The study of Le et al. (2000) on laser induced plasma plume expansion is based on multispecies three-dimensional axisymmetric model.

The model includes the effects of mass diffusion, viscous dissipation, thermal conduction, and non-equilibrium condition for the particles ionization and recombination. They have also considered the influence of ambipolar diffusion on plasma expansion. The plasma plume propagation into an ambient gas environment and various important characteristics such as ion dynamics, shock front, temperature evolution of electrons and atoms, and ionization degree deviations are described in detail. Chen and Bogaerts (2005) have developed a one-dimensional gas-dynamic model for plume expansion in a background gas based on compressible Navier-Stokes equations. Local thermal equilibrium is considered by using Saha-Eggert equations during plasma formation. The Knudsen layer conditions are applied at the interface between the target and plume to couple them. This model has revealed that the assumption of ionization and plasma shielding effects significantly affect plume dynamics.

A few researchers have used Monte Carlo simulations to study the expansion of the plasma plume in PLA (Itina et al., 1998; Garrelie and Catherinot, 1999; Garrelie et al., 1999). In this approach, motion and collisions of particles are simulated by a procedure based on Bird's algorithm (Bird, 1994). A dimensional methodology is used to accurately define the plume expansion for large spot areas and high evaporation rate, by simulating the same plume in a reduced scale. According to this approach, collisions are measured with a frequency similar to that of the actual time scale. The flow is axially symmetric and the area just above the target surface is distributed into a network of cells defined by two coordinates: (i) z coordinate, normal to the target surface, passing through the center of the laser beam spot; (ii) r coordinate, plane parallel to the surface, determining the distance from this axis. Ion formation and recombination, which are primarily important at the initial stage of the plume expansion, cannot be described by this method, though.

1.3 Critical Comparison between PLA and PEBA

In PLA, the ablation process is influenced by the amount of photon energy absorbed by the target. The attenuation of the absorbed energy in the target is taken into account by Lambert-Beer's law by introducing the absorption coefficient of the material. The heat source distribution along the target depth is therefore expressed as an exponential decay function. In the case of PEBA, the ablation stage is not be influenced by the target material optical properties due to the nature of the mechanism of electron beam-target interactions. When electrons strike the target surface, they interact with atoms (electrons) by elastic and inelastic collisions. During an elastic collision, the energies of the electrons and atoms (electrons) remain almost the same even after the interaction. In this scenario, energy lost by electrons is in a small quantity and as deviation angles are wider, this type of collision leads to a deep diffusion of electrons into the target. In the case of inelastic collision, electrons lose a large fraction of their energy. The collision between the atoms of the target and electrons of the beam can lead to either one of these phenomena: (i) the excitation of target atoms (electrons) that promote the electron to a higher potential energy level; or (ii) ionization of the atoms if the incoming electrons have quite high energy. Other remaining inelastic activities are converted into heat, which leads to a better efficiency of the ablation stage. The heat source distribution inside the target does not follow a simple Lambert-Beer's law and must be defined beforehand.

During the initial stage of PEBA plasma plume expansion, the electron temperature is about 1 eV (Tricot et al., 2008). This temperature is lower than measured for plasma induced in PLA, which is around 5 eV for a similar fluence (Namba et al., 2006). This mechanism can be explained by the interaction of the electron beam with the expanding plume, which is slightly different from the interaction between the laser beam and the plume. In PLA, two essential mechanisms occur when

laser interacts with the expanding plume: inverse bremsstrahlung (IB) and photoionization (PI). Absorption of photons by free electrons in the plume is defined by IB phenomenon, while absorption by excited ions and neutral atoms is defined by PI phenomenon. These processes play a substantial role in heating the species and in enhancing the global excitation of the plume species. Therefore, it is very important to include the effect of photon absorption mechanisms during the modeling of PLA. These two mechanisms do not take place at the same magnitude during PEBA ablation, although the interaction between the electron beam and expanding plume is only restricted to electron impact ionization. The cross-section for electron impact ionization maximum value is achieved for electron energy in the range of 10-100 eV. The energy of electrons induced by pulsed electron beam is polyenergtic and has this energy distribution at the end of pulse. It has been reported in the literature (Tricot et al., 2008) for ZnO target, that the electron density for plasma induced by PEBA is around 10^{16}-10^{17} cm^{-3}, which is extremely low as compared to electron densities measured for PLA plasma. Therefore, the electron impact ionization is small. In the case of PEBA, the energetic electrons can deposit their energy over the total pulse duration and the electron beam is not shielded by the expanding plume. This likely leads to better ablation of the target surface and optimal deposition rate as compared to PLA. Deposition rate of 1.1 Å/pulse was reported for pulsed electron beam source functioning at 16 kV (~2.8 J/cm^2) when compared to deposition rate of 0.05 Å/pulse by PLA under the same process conditions. Based on the aforementioned reasons, shielding effect is not a dominating phenomenon during the modeling of PEBA and will not be considered here.

1.4 Thesis Motivation

One of the promising and versatile electron beam materials processing methods is pulsed electron beam ablation for thin film fabrication. Thin film deposition via PEBA is a complex phenomenon,

which goes through many fundamental processes all the way from the generation of intense electron pulses to the irradiation of a target material to the ablation and transfer of the material in the form of a plasma plume to a substrate through expansion in an ambient gas. A thorough examination of the literature suggests the lack of appropriate models to delve into the critical parameters involved in the deposition of the thin films via PEBA. The main purpose of the present research is to develop mathematical models for the fundamental processes underpinning the growth of thin films during PEBA. It is anticipated that the proposed research will help in gaining a fundamental understanding of the numerous phenomena and in optimizing the respective process parameters. Simulation results are be compared with appropriate experimental data in order to validate the results of the mathematical models.

1.5 Research Objectives

Based on the review of the state of the art, the main objectives of the present research are:

a. Development of a mathematical model for the electron beam ablation of the target material.

b. Development of a mathematical model for the expansion of the plasma above the target surface into a background gas.

c. Assessment of different process conditions such as beam efficiency (efficiency factor), accelerating voltage (kV), and beam power density (W/cm^2).

d. Validation of the models by comparing the calculated data with the results obtained from experimental studies. Specifically, pertinent data from the deposition of carbon will be used.

Chapter 2

2 Pulsed Electron Beam Ablation

2.1 Introduction

The key factor in pulsed energy deposition is the ability to produce a high power intensity at the target surface. Although nanosecond pulse-width excimer lasers can successfully fulfill this requirement, a relatively cost-effective and flexible method using pulsed electron beams can also attain this goal. Owing to high current (> 1000 A) and voltage (> 10 kV), pulsed electron beams are able to achieve a power density of ~10^8 W/cm^2 at the surface of a target; a critical characteristic for rapid non-equilibrium heating of the target surface, and a prerequisite for congruent material ablation. In PEBA, a high power pulsed electron beam interacts with the target surface, penetrates 1–2 μm deeper beneath the target surface, causing a quick evaporation of the target material. The process of ablation continues for about 100 ns leading to non-equilibrium heating, which subsequently facilitates stoichiometric preservation of the target composition in the deposited film. Under optimum PEBA process conditions, most of solid state materials can be congruently deposited as thin films. A low pressure gas discharge known as channel-spark (CS) (Figure 2.1) is used to generate a highly energetic beam of electrons (Jiang et al., 1994; Dediu et al., 1995).

The deposition of thin films in PEBA is a complex process and can be described by four stages: (i) generation of highly energetic electrons by the channel-spark device, (ii) irradiation by a beam and target surface ablation, (iii) expansion of the plasma plume in a background gas, and finally, (iv) thin film growth on the substrate. A typical PEBA experimental set-up is depicted in Figure 2.2. The target and substrate are kept inside a chamber, which is usually filled with an inert gas such as Ar, O_2, N_2, etc., at a pressure ranging from 30 mTorr to as low as 1 mTorr. The dimensions

of the target and substrate are of the order of a few centimeters. The distance between the target and the substrate ranges from 40 to 100 mm.

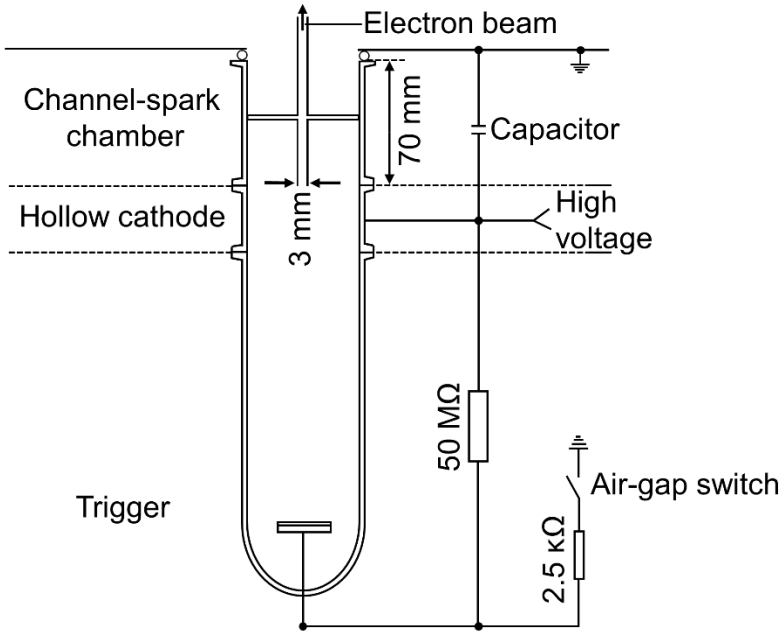

Figure 2.1: Schematic illustration of channel-spark discharge in PEBA. (Reprinted with permission from: Dediu et al., 1995. © 1995, IOP Publishing.)

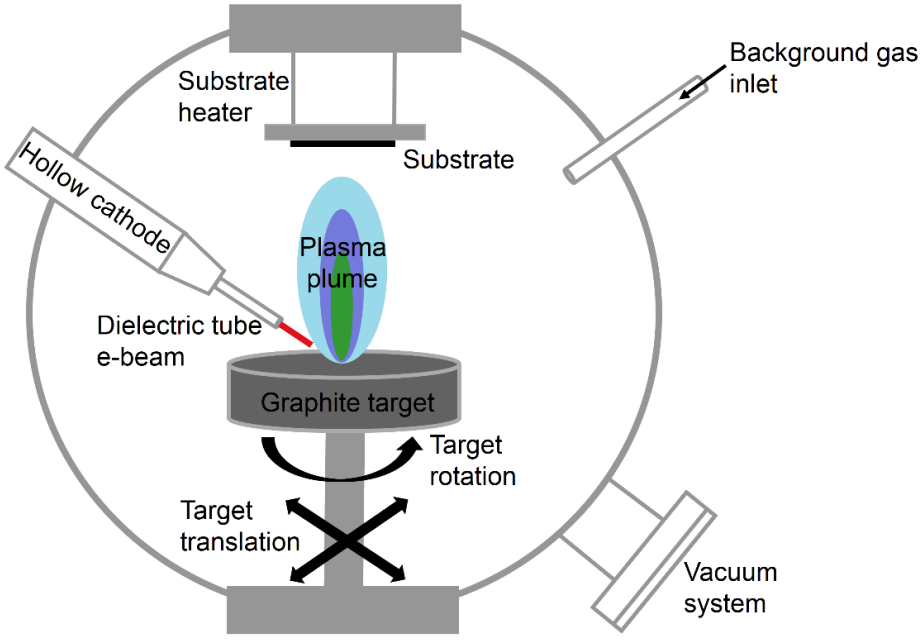

Figure 2.2: Schematic illustration of pulsed electron beam ablation (PEBA) (Ali and Henda, 2015).

2.2 Pulsed Electron Beam Source (PEBS)

The electron source used to generate the energetic beam of electrons is a unique kind of a transient hollow cathode (THC) based on a low pressure gas discharge, or channel-spark (CS), as mentioned earlier. The channel-spark device (Figure 2.1) consists of three components: (i) an alumina tube assembly comprised of a dielectric tube, which functions as an accelerator, (ii) a transient hollow cathode, and (iii) a glass tube assembly engaged for the production of a pre-discharge to trigger the channel-spark. The transient hollow cathode consists of a metallic tube placed in a vertical direction to a planar anode. A pre-discharge at the air spark-gap triggers a confined discharge in the trigger duct, which generates a high voltage. The high voltage, which is delivered to the hollow cathode initiates ignition at the cathode. The hollow cathode is filled with gas at low pressure and coupled with a dielectric acceleration tube. Electrons are extracted from the plasma generated on the inner walls of the hollow cathode. Plasma is primarily induced due to photoelectric effect or ion impact. A reduced potential difference between the hollow cathode and anode leads to extraction of electrons from the plasma. Due to this reduced potential difference across cathode and anode, electrons accelerate slowly, and, accordingly, the possibility for electron impact ionization increases. Electron flow is accelerated towards the anode through a narrow passage connected to the dielectric tube. The electron flow is picked by the dielectric tube for final acceleration towards the target (Müller et al., 1995).

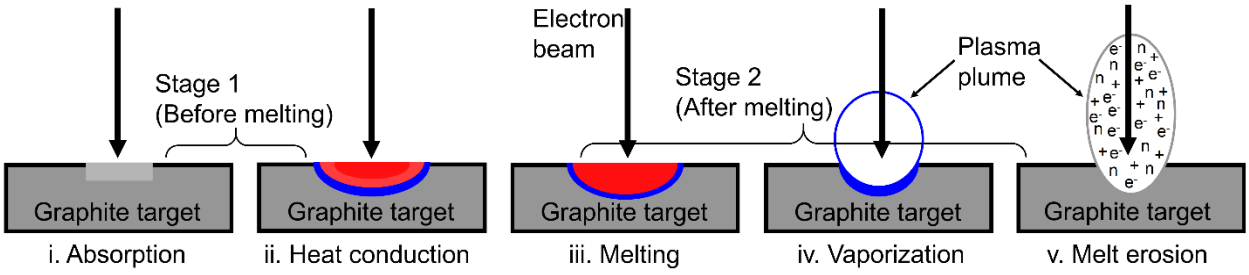

Figure 2.3: Phases of electron beam-target interaction.

2.3 Electron Beam-Target Interaction

When electron beam radiation is incident on a target surface, radiation is absorbed as it penetrates into the target surface. The absorbed radiation heats up the surface, leading to melting and evaporation of the target surface. Removal of material from a target surface by electron beam irradiation comprises complex phenomena, including thermal evaporation, electronic excitation, melting/evaporation, and droplet or solid particle ejections. The various processes involved in electron beam ablation are shown in Figure 2.3 (i-iv). The electron beam ablation process can be considered to occur in two stages. In the first stage, Figure 2.3 (i-ii), the beam energy is absorbed by the target surface leading to an increase in its temperature. During this stage, the electron beam energy directly heats the target surface. The heating rate and the surface temperature of the target are described by the absorption coefficient, thermal conductivity, and the specific heat of the material. In this stage, conduction is the only form of heat transport within the target material. In the next stage, Figure 2.3 (iii-v), ablation is initiated and material is ejected, which subsequently forms a plasma plume above the target surface. During this stage, when the temperature of the target surface reaches its melting point, the melt front penetrates the solid phase underneath. The thermal properties of the target material change during melting, resulting in significantly lower thermal conductivity. Afterwards, vaporization starts to occur when the temperature of the target surface is higher than the melting temperature. In the end, ejection of melted material from the target surface may be caused by the recoil pressure of the vaporizing material. Hence, this exerts a force on the molten bottom of the ablation spot and throwing the material in the vertical direction.

2.4 Plasma Plume Expansion in a Background Gas

Ablated material from the target surface due to electron beam irradiation leads to the development of a plume moving quickly away from the target. Ablated material in the form of a plume is mainly

composed of electrons, ions, and ground or excited-state neutrals. During pulse duration, the majority of the beam energy is converted to the internal energy of the particles in the plume. This energy is composed of energy of electrons in the plasma, thermal energy of the atoms, and energies of evaporation and ionization. The plume expands itself in a vertical direction to the target surface as a result of high internal pressure. The high internal plume pressure (~ 1 kbar) is far greater than any ambient gas pressure (< 1 mbar) inside the deposition chamber. Accordingly, the initial plume propagation is not influenced by the presence of an ambient gas. As a result of pressure gradient and backed by recombination of atoms and electrons, the plume is subjected to constant acceleration. The initial energy spectrum of the plasma plume is produced in the course of this stage. Furthermore, the size of the expanding plasma during this stage is approximately a few times the beam spot size on the target surface.

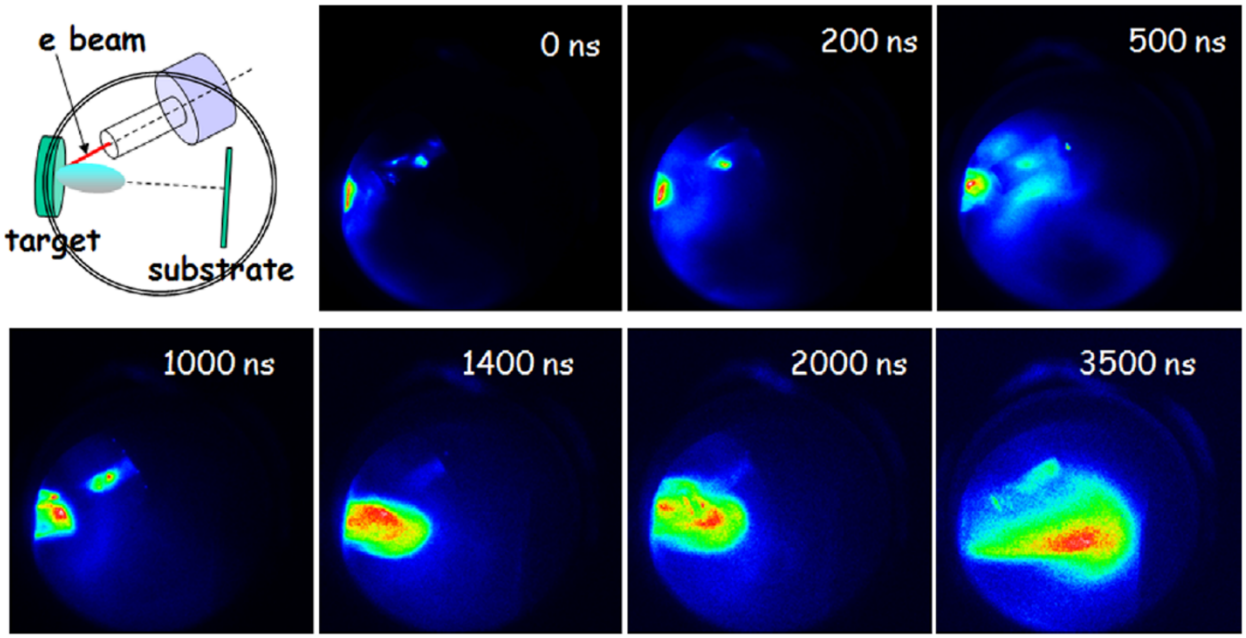

Figure 2.4: Plasma plume expansion time resolved fast images of hydroxyapatite (HA) in an argon gas at an ambient pressure of ≈ 7-15 mTorr induced during pulsed electron beam ablation (PEBA). (Reprinted with permission from: Nistor et al., 2008. © 2008, IOP Publishing.)

After some distance from the target surface, the expansion is quickly restrained by the interaction mechanism between ablated plume particles and the ambient gas molecules. The expansion process continues until the internal pressure is nearly equal to the ambient gas pressure. During this stage, highly energetic (fast) particles of the expanding plume passes through the ambient gas as in a vacuum, whereas slightly less energetic (slow) particles act on the surrounding ambient gas. The collisions among the slow particles and the ambient gas molecules causes collisional excitation of the plume particles at the boundary interface between the plume and the gas. These slow moving particles drive the compressed layer of the ambient gas away from the target surface. As result of this, an internal and external shock waves may be produced.

The physical properties of the ablated plume, i.e., particles velocity, mass and angular distribution of the ablated particles, play essential parts in the growth of thin films by PEBA. Specifically, the thickness distribution of the film grown on the substrate is primarily controlled by the plume shape that has emerged in the course of the expansion from the target surface to the substrate (Müller et al., 1995; Schou et al., 2007). Time-lapse images of the plasma plume expansion in the presence argon as an ambient gas is shown in Figure 2.4.

2.4.1 Plasma

Plasma is often termed as the fourth state of matter. It is a distinct state of matter, which is mainly composed of a mixture of electrically charged particles, i.e., electrons and ions, and neutral atoms. It is believed that over 99% of the visible matter in the universe exists in a plasma state. In 1929, the word plasma, for the first time, was introduced by Irving Langmuir to explain the behavior of ionized gases inside high-current vacuum tubes (Langmuir, 1929). In a short period of time, it was

understood that plasmas exhibit a unique behavior from simple non-ionized gases, and are evidently different from condensed solid and liquid states of matter.

In a simple non-ionized gas, every atom consists of equal number of positive and negative charges; the positive charges are confined within the nucleus and surrounded by same number of negative charges (i.e., all atoms are electrically neutral). A gas converts into plasma when increase in the temperature causes a substantial number of atoms to discharge few or all of their electrons. These atoms become positively charged, and are surrounded by "freely" moving electrons. These atoms and the resulting electrically charged gas is termed an ionized gas. Plasma is an ionized gas, which is also defined as a quasi-neutral gas that exhibits a collective behavior in the presence of external forces (i.e., electric or electromagnetic fields).

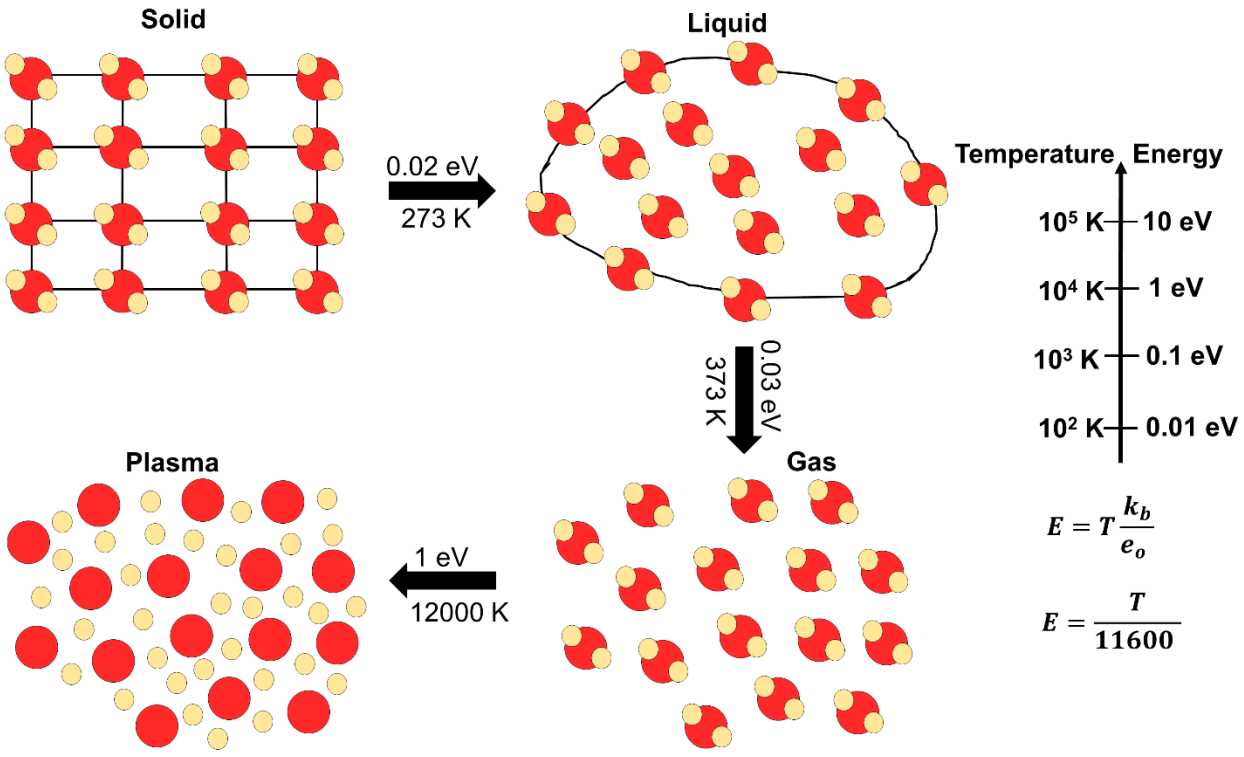

Figure 2.5: Schematic sequence for water converting into different states of matter.

All states of matter are characterized by different levels of molecular organization, depending on the strength of the binding energy. As temperature increases, the average kinetic energy of a molecule surpasses the binding energy and causes matter to change phase in the sequence solid → liquid → gas and finally plasma (Figure 2.5).

2.4.2 Properties of Plasmas

2.4.2.1 Degree of Ionization

The degree of ionization is one of the important properties used to characterize plasmas. The degree of ionization is a measure of the number of ionized atoms. It can be defined by,

$$\alpha = \frac{n_e}{n_e + n_a} \tag{1}$$

where n_e is the number density of electrons and n_a is the number density of neutral atoms. The degree of ionization is mainly dependent on temperature as can be seen in Figure 2.6.

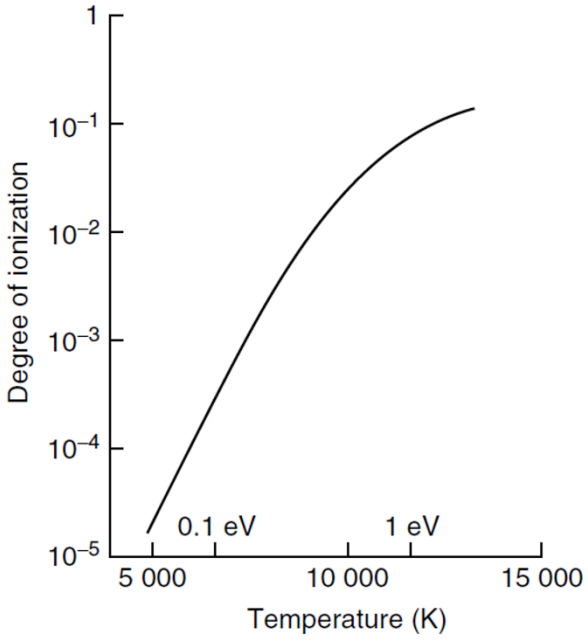

Figure 2.6: Variation of the degree of ionization of an atomic gas with temperature. (Reprinted with permission from: Harry, 2010, © 2010, Wiley and Sons Inc.)

In a plasma, not all particles are necessarily ionized, resulting in gases that are only partially ionized. The degree of ionization in conventional plasmas is in the range 10^{-7}–10^{-4}. When the degree of ionization is close to unity, such a plasma becomes fully ionized. When the degree of ionization is less than unity, the plasma is said to be weakly ionized.

2.4.2.2 Debye Length

In plasma physics, the Debye length is one of the most essential and fundamental length scales. It defines a screening distance, beyond which charges are unaware of other charges inside of the Debye length. A charged atom in a plasma will attract opposite charged atoms and repel similarly charged atoms to the point that its electric field is screened by the charged atoms it has attracted. Therefore, atoms outside the screening charges are unaware of the existence of the interior charged atoms. The Debye length can be expressed as,

$$\lambda_D = \sqrt{\frac{\varepsilon_o k_B T_e}{e_o^2 n_e}} \tag{2}$$

where ε_o, k_B, T_e, e_o, and n_e are the permittivity of free space, the Boltzmann constant, the electron temperature, the charge of an electron, and the number density of the electrons, respectively.

2.4.2.3 Debye Number

Debye number can be defined as the average number of electrons in a plasma contained within a sphere radius of the Debye length. The Debye number can be expressed as,

$$N_D = \frac{4}{3}\pi n_e \lambda_D^3 \tag{3}$$

where λ_D and n_e are the Debye length and the number density of the electrons, respectively. This parameter of plasma is critical in various ways to define its behavior. In order for a plasma to

demonstrate a collective behavior (charged particles behave in a collective way as a result of electric fields created within the plasma), the Debye number must be far greater than unity ($N_D \gg 1$).

2.4.2.4 Plasma Frequency

Plasm frequency is defined as when there is slight movement of opposite charged particles in a plasma, there will be a restoring electric force moving them back resulting in charged particles oscillating with a certain frequency. It is used to determine the characteristic properties of plasmas at high frequency, namely the cut-off frequency at which an electromagnetic wave will not be transmitted through a plasma. It can be expressed by,

$$\omega_p = \sqrt{\frac{e_o^2 n_e}{\varepsilon_o m_e}} \tag{4}$$

where e_o, n_e, ε_o, and m_e are the charge of the electron, number density of the electron, permittivity of free space, and effective mass of the electrons, respectively.

2.4.2.5 Local Thermodynamic Equilibrium

A plasma with a sufficiently high electron density is considered to be in a local thermodynamic equilibrium (LTE) state. As the density of plasma is increased, the number of collisions between atoms and ions increases. Excited state populations are determined by collision processes at adequately high densities. For a plasma to be in LTE state, the electron density should be adequately high for effective de-excitation processes to occur. The LTE condition can be tested by McWhirter criterion (McWhirter, 1965), which is expressed by the following relation,

$$n_e(cm^{-3}) \geq 1.6 \times 10^{12} \sqrt{T} (\Delta E_{nm})^3 \tag{5}$$

where T is the plasma temperature (K), and ΔE is the highest energy value for the considered electronic transitions (eV). This is a necessary criterion for LTE condition, but insufficient, and is normally satisfied during the first stages of a plasma lifetime.

The typical properties of a plasma induced in PEBA have been summarized and are given in Table 2.1.

Table 2.1: Properties of plasma induced during PEBA.

Electron temperature	Electron density	Degree of ionization	Debye length	Debye number	Plasma frequency
≤ 1.3 eV	$\cong 10^{17}$ cm^{-3}	$\cong 0.70$	$\cong 2.70 \times 10^{-8}$ m	$\cong 5.90 \times 10^{6}$	$\cong 1.80 \times 10^{13}$ rad/s

2.5 Thin Film Deposition at the Substrate

All thin film deposition techniques consists of three principal steps:

(i) Generation of the suitable ionic, molecular or atomic particles.

(ii) Distribution of these particles at the substrate surface via a medium.

(iii) Formation of solid film at the substrate surface via condensation, either directly or through an electrochemical and/or chemical reaction.

Deposition of a thin film occurs as a result of nucleation and growth processes. The fundamental processes occurring during growth of a thin film on a substrate surface are schematically represented in Figure 2.7. The processes taking place during the early stage of growth at the substrate surface can be described by six steps as follows (Reichelt, 1988):

1. Particles coming from the vapor source strike the substrate surface and see their vertical component of velocity deteriorates. Subsequently, arriving particles get adsorbed on the surface.

2. During the early stage of adsorption, particles are in thermodynamic non-equilibrium with the substrate and move over the substrate. As a result, particles tend to diffuse at a particular distance on the surface and desorb yet again.

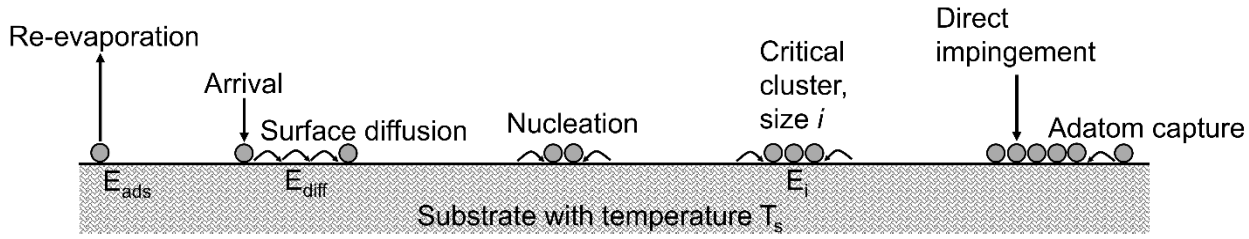

Figure 2.7: Schematic illustration of processes involved in nucleation and growth of thin film at the substrate.

3. Clusters/nuclei begin to grow in size as they collide with other adsorbed particles under the condition that particles on the substrate surface do not get desorbed. After sometime, cluster become thermodynamic stability and reaches a certain critical size. This is known as the nucleation stage, which consists of the formation of chemisorbed, stable, and critical-sized cluster/nuclei.
4. A saturation nucleation density is reached, when a significant amount (threshold level) of critical cluster/nuclei develops and grows in size. A nucleus starts to grow in both horizontal direction by surface diffusion of the adsorbed particles, and vertical direction by direct impingement of the incident particles. Accordingly, grown cluster/nuclei results in islands.
5. Next phase in the phenomena of thin film growth is coalescence stage, where small island begin coalescing with other islands in an effort to decrease the surface area of a substrate. This might result in generation of larger islands, which are known as agglomerates.

6. Islands begin to increase in size, leaving gaps and grooves on substrate surface. During this phase, film structure transition takes place from discontinuous island pattern to porous network pattern. Filling of the gaps and grooves produces an entirely continuous film.

Thin film deposition phenomena on substrate surface can be outlined as comprising of a geometric process of nucleation, three-dimensional cluster/nuclei growth through controlled surface diffusion, and generation of film structure network followed by agglomeration to provide a continuous film (Wasa et al., 2004).

Thin film growth and nucleation on the substrate surface is not within the scope of the present research. Accordingly, it will not be considered in the current study.

Chapter 3

3 Mathematical Models

3.1 Introduction

The models outlined hereafter describe the main processes involved in the growth of thin films during PEBA. These processes include electron beam-solid target interaction, the vaporization of target material, and the propagation of ejected particles in the presence of process background gas. The processes and potential couplings between them are developed in the following.

3.2 Model of Electron Beam Ablation

In order to model the phenomena taking place during pulsed electron beam interaction with a target surface, it is essential to have complete understanding of the concepts involved in the dynamics of thermal field and, eventually, phase transition (state change). The interaction of an electron beam with a target material is quite a complex physical process and takes place in a sequence of phenomena. Whether the target surface undergoes melting or sublimation during interaction with pulsed energy beams (PLA and PEBA) has been a subject of active debate (Kelly and Miotello, 1996; Pattini et al., 2013; Tricot et al., 2010; Venkatesan et al., 1984). In the case of PLA, it has been demonstrated that the target can experience four kinds of thermal processes for ablation, which include normal vaporization, normal boiling, explosive boiling, and subsurface superheating (Bulgakova, and Bulgakov, 2001). In the case of PEBA, it has been reported by Tricot et al. (2010) that normal vaporization could be the primary thermal mechanism (heating and sublimation of the target surface) leading to the ablation of a target surface. Due to high power density (10^8 W/cm^2) delivered to the target surface, fast heating and vaporization take place far from thermodynamic equilibrium. Solid-to-vapor transition is principally independent of the phase

diagram and composition of the target material, resulting in congruent sublimation and potentially, target stoichiometry preservation in the deposited thin film (Müller et al., 1995; Strikovski et al., 2010).

Clusters have been observed during thin films growth by PEBA in several studies (Chen et al., 2005; Mathis and Christen, 2007; Nistor et al., 2008). Cluster formation has been attributed to explosion/boiling of liquid phase and suggests that target surface go through melting transition during electron beam-target interaction (Zhijian et al., 2005). In the case of graphite, it has been relatively well established that at ambient pressure sublimation occurs when graphite is heated instead of being melted. However, the pressure of carbon in the gas phase is relatively low, and at adequate pressure and temperature, melting of graphite will take place instead of sublimation (Zazula, 1997). In their study of graphite melting by pulsed laser, Venkatesan et al. (1984) have reported that laser pulses are Gaussian in nature with a full width at half maximum (FWHM) of 30 ns, and, accordingly, the thermal energy is connected into the lattice of graphite in a duration sufficiently short to eradicate the effects of sublimation process that has been seen to take place with slower heating methods. Based on the aforementioned reasons, the nature of thermal mechanisms involved during electron beam ablation of a graphite target seems to be a highly controversial issue. Accordingly, both melting and sublimation as thermal mechanisms are considered here separately to model electron beam ablation stage.

3.2.1 Heating and Sublimation

When electron beam radiation is focused on a target surface, a fraction of the incident beam energy is backscattered whereas the remaining portion is absorbed by the electron subsystem of the target material. Subsequently and due to interactions between electrons and phonons, energy is

transferred to phonons in the material lattice (Ptitsin, 2012). The energy transferred to the phonons propagates in the target material through the mechanism of heat conduction. Over the past decade, advances in the field of nanotechnology have indicated that heat conduction in the regime of micro-scale, nano-scale, and ultrafast processes may diverge considerably from the predictions of the classical Fourier's law, due to finite mean-free time of energy carriers and scattering at the target boundary and interface. Recently, in order to compensate for the deficiency of the Fourier law that leads to the unreasonable result of an infinite speed of heat propagation, hyperbolic heat conduction (Kim et al., 1990), ballistic-diffusive heat-conduction (Chen, 2001), and constitutive heat conduction equations based on the Boltzmann transport equations (BTE) (Miranda et al., 2011) have been developed. Therefore, a preliminary investigation on the validity of the heat conduction equation used for nanosecond range electron beam ablation must be undertaken. As reported in the literature (Ready, 1971), the mean-free time among electron collisions in a metallic conductor is on the order of 10^{-13} s, whereas the duration of heat propagation to the lattice is of the order of 10^{-12} s. Accordingly, for nanosecond pulse width range, the temperature of lattice and electron-gas are approximately of the same in magnitude, and therefore, thermal equilibrium can be considered (Zhang et al., 2001). The question of which approach is more appropriate for a particular case is determined by the ratio ($L/l_e \gg 1$) between the characteristic length of the target material (L) and mean-free path of the electrons (l_e). In the case of graphite, the mean-free path of the electrons and characteristic length are approximately 15.4 nm (see calculation below) and 1068 nm (see section 3.2.5 One-dimensional assumption), respectively. This means that the ratio is much greater than unity. As a result, the classical heat transfer concepts can be enforced for nanosecond pulsed electron beam ablation.

Detail calculation of ratio ($L/l_e \gg 1$) between the characteristic length of the target material (L) and mean-free path of the electrons (l_e) is as follows,

- Relaxation time τ_e is given as (Alloul, 2011),

$$\tau_e = \frac{\sigma m_e}{ne^2} \tag{1}$$

$$\tau_e = \frac{(2.5 \times 10^5 \Omega^{-1} m^{-1})(9.10938291 \times 10^{-31} kg)}{(3 \times 10^{24} m^{-3})(1.60217657 \times 10^{-19} C)^2}$$

$$\tau_e = 2.9572426 \times 10^{-12} s$$

- Speed of electrons v_e can be estimated as (Alloul, 2011),

$$v_e = -\left(\frac{e\tau_e}{m_e}\right)\epsilon \tag{2}$$

$$v_e = -\left(\frac{(1.60217657 \times 10^{-19} C)(2.9572426 \times 10^{-12} s\,)}{9.10938291 \times 10^{-31} kg}\right)(10^4\, V/m)$$

$$v_e = 5.20 \times 10^3\, m/s$$

- Mean-free path l_e can be expressed as (Alloul, 2011),

$$l_e = v_e \tau_e \tag{3}$$

$$l_e = (5.20 \times 10^3\, m/s\,)(2.9572426 \times 10^{-12} s\,)$$

$$l_e = 1.54 \times 10^{-8}\, m$$

- The ratio

$$\frac{L}{l_e} \gg 1 \tag{4}$$

$$\frac{1.068 \times 10^{-6}}{1.54 \times 10^{-8}} \gg 1$$

$$69.35 \gg 1$$

where σ, m_e, n, e and ϵ are the electrical conductivity of graphite, mass of electron, electric carrier concentration, charge of electron and electric field, respectively.

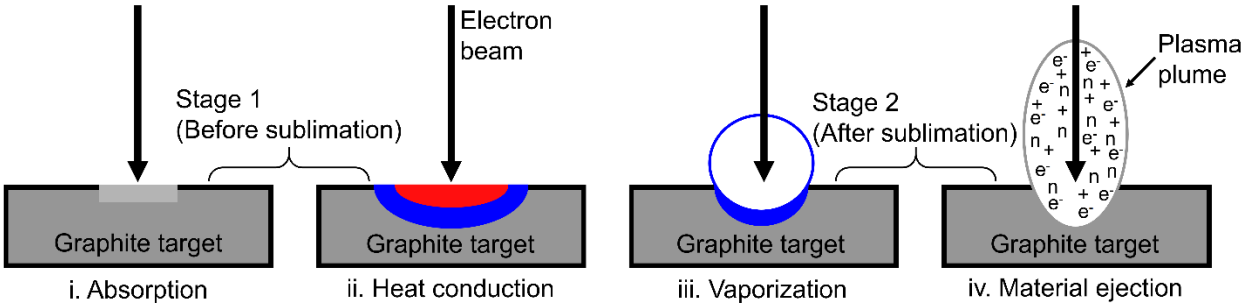

Figure 3.1: Phases of electron beam-target interaction during sublimation.

The thermal model for electron beam-target interaction in the regime of sublimation can be considered to take place in two stages as shown in Figure 3.1: the first stage, before sublimation, consists of (i) absorption of electron beam energy and (ii) heating of the target surface via conduction, and the second stage, after sublimation, comprises (iii) vaporization of the surface and (iv) material ejection from the target surface. Accordingly, the temperature distribution inside the target surface along the depth can be defined by a two stage one-dimensional heat conduction model. The spatial dimension of the model depends on the incident electron beam parameters and the thermophysical properties of the target material. The diameter of the electron beam is typically in the range of a couple millimeters, which is much larger than the diffusion depth (discussed in detail in next chapter). In this case, heat conduction can be considered to take place predominantly in one dimension along the target depth (Steinbeck et al., 1985). A rough estimate of surface thermal radiation reveals that the latter is very small (<<1%) compared to the incident beam energy fluence on the target surface, and, thus, it has been neglected in our model. Ablation during PEBA exhibits a peculiar characteristic during electron-target atoms interactions. Beam electrons interact with target atoms effectively, regardless of whether they are in solid or vapor state. Accordingly,

scattering cross-section for electrons by the target atom is not altered before or after the ablation stage. As a result, the electron beam can efficiently interact with the target surface and shielding effect during ablation is due to absorption of beam energy by the mass of target atoms within the electron beam penetration depth (Strikovski and Harshavardhan, 2003; Harshavardhan and Strikovski, 2005). In the current study, shielding has not been considered by assuming that ablated target mass is much smaller than the mass of target within the beam penetration depth. The heat conduction equation, which allows the calculation of time-dependent temperature distribution along the target depth, $T(x,t)$, before the target surface has started to vaporize is expressed as,

$$\rho_s C_{p_s} \frac{\partial T}{\partial t} = \frac{\partial}{\partial x}\left(k_s \frac{\partial T}{\partial x}\right) + Q(x,t) \qquad (0 < t \leq t_{sb}) \tag{5}$$

the initial condition,

$$T(x,0) = T_0 \tag{6}$$

boundary conditions,

$$-k_s \frac{\partial T}{\partial x}\Big|_{x\,=\,0} = Q_s(t) \qquad (0 < t \leq t_{sb}) \tag{7}$$

$$-k_s \frac{\partial T}{\partial x}\Big|_{x\,=\,l} = 0 \qquad (0 < t \leq t_{sb}) \tag{8}$$

where ρ_s, C_{p_s}, and k_s are the solid phase density, specific heat capacity, and thermal conductivity of the target material, respectively. The term Q is the heat source, x is the distance from the target surface along the incident direction, l is the thickness of the target material, Q_s is the surface power density delivered by the heat source, and t_{sb} is the time required by the target surface to attain the sublimation point. It has been shown that for highly absorbing materials (like graphite) and slow

vaporization (electron beam ablation) the power density (Q_s) at the target surface must be taken into account (Bäuerle, 2011).

When the target surface temperature rises and exceeds the sublimation temperature, vaporization will ensue. During the vaporization stage, the thermal field in the target can be calculated by introducing the moving vaporization front in the one-dimensional heat conduction equation (Peterlongo et al., 1994). The latter takes the form,

$$\rho_v C_{p_v}\left(\frac{\partial T}{\partial t} - u(t)\frac{\partial T}{\partial x}\right) = \frac{\partial}{\partial x}\left(k_v \frac{\partial T}{\partial x}\right) + Q(x,t) \qquad (t_{sb} < t \leq \tau) \tag{9}$$

here the initial and boundary conditions are

$$T(x, t_{sb}) = T(t_{sb}) \tag{10}$$

$$-k_v \frac{\partial T}{\partial x}\Big|_{x\,=\,0} = Q_s(t) - L_v \rho_v u(t) \qquad (t_{sb} < t \leq \tau) \tag{11}$$

$$-k_v \frac{\partial T}{\partial x}\Big|_{x\,=\,l} = 0 \qquad (t_{sb} < t \leq \tau) \tag{12}$$

where ρ_v, C_{p_v}, and k_v are the target material vapor phase density, specific heat capacity, and thermal conductivity, respectively. The terms $u(t)$, L_v, and τ are the surface recession velocity, latent heat of vaporization, and duration of the electron beam pulse, respectively. The time required by the target surface to attain the sublimation point can be estimated by (Bäuerle, 2011),

$$t_{sb} = \frac{\pi (T_{sb} - T_0)^2 \rho_s C_{p_s} k_s}{4 Q_s(t)^2} \tag{13}$$

where T_{sb} is the sublimation temperature.

3.2.2 Heating, Melting and Vaporization

The electron beam ablation model in the regime of melting can be considered to occur in two stages as presented in Figure 3.2. The first stage, before melting, comprises (i) the beam energy is absorbed by the target surface, and (ii) heat conduction leads to an increase in target temperature. The next stage, during and after melting, consists of (iii) the temperature of the target surface reaches its melting point, (iv) target surface vaporization starts to take place, and (v) ablation is initiated and material is ejected. Accordingly, thermal phenomena involved during the interaction of the target surface with the electron beam irradiation comprises of heating, melting, and eventually vaporization of a fine fraction of the target surface. In the solid phase, before melting starts to take place, thermal diffusion along the target depth can be described by one-dimensional heat conduction equation,

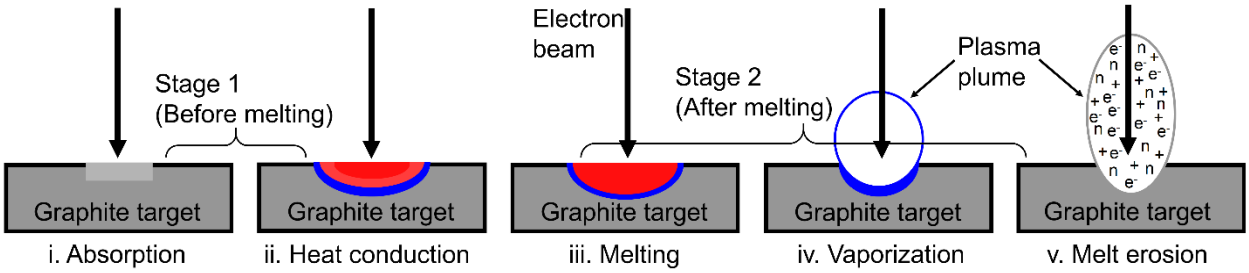

Figure 3.2: Phases of electron beam-target interaction during melting.

$$\rho_s C_{p_s} \frac{\partial T}{\partial t} = \frac{\partial}{\partial x}\left(k_s \frac{\partial T}{\partial x}\right) + Q(x,t) \qquad (0 < t \leq t_m) \tag{14}$$

the initial condition,

$$T(x,0) = T_0 \tag{15}$$

and boundary conditions,

$$-k_s \frac{\partial T}{\partial x}\Big|_{x\,=\,0} = Q_s(t) \qquad (0 < t \leq t_m) \tag{16}$$

$$-k_s \frac{\partial T}{\partial x}\Big|_{x=l} = 0 \qquad (0 < t \leq t_m) \tag{17}$$

where ρ_s, C_{p_s}, and k_s are the solid phase density, specific heat capacity, and thermal conductivity of the target material, respectively. The term Q is the heat source, x is the distance from the target surface along the incident direction, l is the thickness of the target material, Q_s is the surface power density delivered by the heat source, and t_m is the time required by the target surface to attain the melting point.

During the melting confinement stage, the temperature of the target surface reaches the melting point and the melt front penetrates through the solid. Afterwards, surface vaporization starts to takes place when the target temperature exceeds the melting temperature. To describe the thermal diffusion in the liquid state during which irradiated surface recedes with velocity due to ablation, the temporal and spatial dependence of the temperature in the target can be evaluated by including the recession velocity in the one-dimensional heat conduction equation (Peterlongo et al., 1994),

$$\rho_l C_{p_l}\left(\frac{\partial T}{\partial t} - u(t)\frac{\partial T}{\partial x}\right) = \frac{\partial}{\partial x}\left(k_l \frac{\partial T}{\partial x}\right) + Q(x,t) \qquad (t_m < t \leq \tau) \tag{18}$$

here the initial and boundary conditions are

$$T(x, t_m) = T(t_m) \tag{19}$$

$$-k_l \frac{\partial T}{\partial x}\Big|_{x=0} = Q_s(t) - \rho_l[L_m u_m + L_v u(t)] \qquad (t_m < t \leq \tau) \tag{20}$$

$$-k_l \frac{\partial T}{\partial x}\Big|_{x=l} = 0 \qquad (t_m < t \leq \tau) \tag{21}$$

where ρ_l, C_{p_l}, and k_l are the target material liquid phase density, specific heat capacity, and thermal conductivity, respectively. The terms u_m, $u(t)$, L_m, L_v, and τ are the melting front velocity,

surface recession velocity, latent heat of fusion, latent heat of vaporization, and duration of the electron beam pulse, respectively. It has been shown that for highly absorbing materials (like graphite) and slow vaporization (electron beam ablation), boiling can be assumed to take place inside a thin layer of target surface and the boundary condition can be written as equation (20) (Bäuerle, 2011). The time required by the target surface to attain the melting point can be estimated by (Xie and Kar, 1997),

$$t_m = \frac{\pi {k_s}^2 (T_m - T_0)^2}{4\alpha_s Q_s(t)^2} \tag{22}$$

where α_s is the thermal diffusivity of the target material in the solid phase and T_m is the melting temperature of the target material.

When rapid melting and solidification take place, the melting rate is assumed to be controlled by interface kinetics instead of thermal diffusion at the interface. In the case of graphite, interface kinetics can be defined by a melt interface growth model (Jackson, 2002). During melt interface growth, the melting front velocity is proportional to superheating at the interface (Xu et al., 1995),

$$u_m = \mu_m (T_{mi} - T_m) \tag{23}$$

where μ_m and T_{mi} are the kinetic melting coefficient and melt interface temperature, respectively. The kinetic melting coefficient during melting can be defined by crystal growth thermodynamics as in the Wilson-Frenkel model (Jackson, 2002). According to this model, the expression for the kinetic melting coefficient can be estimated by,

$$\mu_m = \frac{6 d_l f}{\Lambda^2} D \frac{L_m}{k_B T_{mi} T_m} \tag{24}$$

where d_l, f, Λ, and D are the distance between two adjacent crystalline layers, fraction of collisions among the crystal which adds to the crystal growth, average length of the diffusive jump of atoms in the liquid, and diffusion coefficient of the liquid, respectively. Accordingly, the diffusion coefficient of the liquid that provides the amount of atoms that attach to crystal can be given as,

$$D = \frac{1}{6}\Lambda^2 \nu_D exp\left(-\frac{Q_A}{k_B T_{mi}}\right) \tag{25}$$

where ν_D is the frequency of atoms on the order of the Debye frequency, and Q_A is the activation energy of the atoms for diffusive motion in the liquid.

3.2.3 Vaporization Phenomena

Vaporization dynamics of the target surface irradiation by the electron beam is primarily determined by the surface temperature of the target. During the process of sublimation/vaporization, the surface recession velocity can be evaluated assuming that the vaporization flux from the target surface follows the Hertz-Knudsen equation (Peterlongo et al., 1994), and it can be given by,

$$u(t) = (1-\beta)\frac{P_s(T_s)}{\rho}\left(\frac{m}{2\pi k_B T_s}\right)^{1/2} \tag{26}$$

where β is the back flux coefficient, $P_s(T_s)$ is the saturated vapor pressure at the surface temperature T_s, m is the average mass of target particle, and k_B is the Boltzmann constant. The back flux coefficient is defined as the fraction of particles returning back to the target as a result of collisions among particles just above the target surface. The back flux coefficient amounts to approximately 18% of the flow of the vaporized particles (Anisimov, 1968). In the case of normal vaporization, the solid is in equilibrium with the saturated vapors just above the target surface. The

solid/liquid to vapor phase transition has been assumed to follow the Clausius-Clapeyron equation (Peterlongo et al., 1994),

$$P_s(T_s) = P_0 exp\left[\frac{mL_v}{k_B}\left(\frac{1}{T_{pt}} - \frac{1}{T_s}\right)\right] \tag{27}$$

where P_0 is the normal atmospheric pressure, L_v is the latent heat of vaporization, and T_{pt} is the phase transition temperature either sublimation (T_{sb}) or boiling (T_b) temperature under P_0.

High vaporization rates occur when the beam energy density absorbed by the target surface is far greater than the amount of energy required to vaporize the target surface (Zweig, 1991). When high vaporization rates ensue from high electron beam power densities, condensation of the particles becomes substantial as a result of the back flux. During high vaporization rates, the velocities of the vapor particles escaping from the target surface transform from an anisotropic to an isotropic distribution through collisions between the vapor particles themselves. This isotropic distribution is achieved inside a very thin layer adjacent to the target surface, which is known as the Knudsen layer (KL). Typically, this transformation occurs within several mean-free paths, and the vapor properties such as temperature, pressure, and density beyond this layer may have a jump in their respective magnitude. Particles back flux and KL conditions according to Knight's vaporization model (Knight, 1979) can be given as follows,

$$\frac{T_k}{T_s} = \left[\sqrt{1 + \pi\left(\frac{\gamma_v - 1}{\gamma_v + 1}\frac{m_v}{2}\right)^2} - \sqrt{\pi}\frac{\gamma_v - 1}{\gamma_v + 1}\frac{m_v}{2}\right]^2 \tag{28}$$

$$\frac{\rho_k}{\rho_s} = \sqrt{\frac{T_s}{T_k}}\left[\left({m_v}^2 + \frac{1}{2}\right)e^{{m_v}^2} erfc(m_v) - \frac{m_v}{\sqrt{\pi}}\right] + \frac{1}{2}\frac{T_s}{T_k}\left[1 - \sqrt{\pi} m_v e^{{m_v}^2} erfc(m_v)\right] \tag{29}$$

where T_k and ρ_k are the temperature and density of the particles leaving the Knudsen layer, respectively, T_s and ρ_s are the target surface temperature and density of the target, respectively, and γ_v is the specific heat ratio. The term $m_v = \sqrt{\gamma_v/2}\,M$, where M is the Mach number. According to equations. (28) and (29), the surface recession velocity can be given as,

$$u(t) = \frac{P_s(T_s)}{\rho_s}\left(\frac{m}{2\pi k_B T_s}\right)^{1/2} - \alpha\frac{\rho_k}{\rho_s}\sqrt{\frac{R_g T_k}{2\pi}}\left(e^{-{m_v}^2} - \sqrt{\pi} m_v erfc(m_v)\right) \qquad (30)$$

where R_g is the gas constant of the vapor, and α is defined as:

$$\alpha = \left[(2{m_v}^2 + 1) - m_v\sqrt{\pi\frac{T_s}{T_k}}\right] e^{{m_v}^2}\frac{\rho_s}{\rho_k}\sqrt{\frac{T_s}{T_k}} \qquad (31)$$

3.2.4 Heat Source

The electron source used to generate the energetic beam of electrons is based on a low pressure gas discharge known as channel-spark (Müller et al., 1995; Harshavardhan and Strikovski, 2005). In the context of electron beam ablation, energy transfer takes place essentially by collisions of the beam electrons and the electrons in the target material (Alloul, 2011). The description of the energy losses by the electrons of the beam is based on the observation that as the primary electrons penetrates deeper into the target, they are slowed down. Monte Carlo (MC) simulations are well suited (very accurate) to estimate the profile of the energy transferred to the target material by the electron beam. This method is based on tracking a primary electron of initial energy E and direction v, and finding where the next collision will occur based on the calculation of the inelastic mean free path. At this point, a decision is made as to whether the collision is elastic or inelastic. In the case of an elastic collision, the electron energy remains unchanged and its direction v varies. In the case of an inelastic collision, the electron energy is recalculated according to the stopping

power formula (Equation 32) while keeping direction v constant. This iterative process of tracking continues until the energy of the electron has reached a threshold below which energy can be considered to be thermalized. To achieve a statistically meaningful sampling, this process is repeated for thousands of electrons. The stopping power formula is given by (Joy and Luo, 1989),

$$-\frac{dE}{ds} = 785 \times \frac{Z\rho}{AE} \ln\left(\frac{1.166 \times (E + kJ)}{J}\right) \tag{32}$$

where E is the instantaneous electron energy, s is the distance travelled along the electron trajectory, Z is the atomic number of the target material, A is the atomic weight of the target material, J is the mean ionization energy and k is a variable depending only on Z.

The source of electrons in PEBA is polyenergetic in nature (Kowalewicz & Redel, 1995; Tricot et al., 2010). In order to define the heat source appropriately, the apportionment of energy must be taken into consideration. In the present study, the electrons of the beam have been categorized into three different groups for an electron beam accelerating voltage of 15 kV.

(a) The first group (A) appears during the initial 33.3 ns of the electron beam pulse and is composed of fast energetic electrons with energy ranging from 6 to 15 keV and a current of 140 A.

(b) The second group (B) consists of electrons that appear in the next 33.3 ns of the pulse and with energies between 2 and 6 keV. The magnitude of the current is 220 A.

(c) The last group (C) is composed of low energy electrons (<2 keV) that appear during the final 33.3 ns of the pulse. The current has a magnitude of 400 A.

Similarly, for electron beam operating at an accelerating voltage other than 15 kV, the first group of electrons appearing during the initial 33.3 ns of the beam can be adjusted by increasing or decreasing its electron energy (e.g. 15 to 16 or 14 keV).

The analytical expression of maximum energy deposited by each group of electrons can be fitted into a polynomial function as,

$$\frac{E}{E_{max}}(x) = f_{A,B,C}(x) = \sum_{i=0}^{7} a_i \times x^i \tag{33}$$

where x is the penetration depth along the target material.

Finally, in order to estimate the power density delivered to the target, the most probable penetration depth by each group of electrons, $h_{A,B,C}$, is calculated. This calculation gives the amount of thermalized electrons inside the target as a function of the depth for each group of electrons. The surface power density delivered by the heat source to the target surface is given by,

$$Q_s(t) = \begin{Bmatrix} \frac{I_A E_A}{S_a} for\ 0\ ns\ \leq t\ < 33.3\ ns \\ \frac{I_B E_B}{S_a} for\ 33.3\ ns\ \leq t\ < 66.6\ ns \\ \frac{I_C E_C}{S_a} for\ 66.6\ ns\ \leq t\ < 99.9\ ns \end{Bmatrix} \tag{34}$$

where I is the beam current, E is the electron energy, $S_a = \pi r^2$ is the beam spot cross-sectional area on the target surface, and r is radius of the beam spot on the target surface ($r = 2\ mm$). Hence, the heat source is defined by the following expressions:

$$q(x,t) = \begin{Bmatrix} f_A(x)\frac{I_A E_A}{\pi r^2 h_A}\ for\ 0\ ns\ \leq t\ < 33.3\ ns \\ f_B(x)\frac{I_B E_B}{\pi r^2 h_B}\ for\ 33.3\ ns\ \leq t\ < 66.6\ ns \\ f_C(x)\frac{I_C E_C}{\pi r^2 h_C}\ for\ 66.6\ ns\ \leq t\ < 99.9\ ns \end{Bmatrix} \tag{35}$$

where electron energy (E) and current (I) values are in eV and A, respectively. The terms I_A (I_B, I_C) and E_A (E_B, E_C) are the current and average energy of group A (B, C) electrons, respectively. The magnitudes of E_A, E_B and E_C are the average values of the energy intervals of each group of electrons, (i.e., $E_A = 10.5$ keV, $E_B = 4$ keV, $E_C = 1$ keV). Not all electrons diffusing inside the target surface contribute to the increase in the internal energy of the target. During the bombardment stage, many electrons are discharged by the target surface. Those discharged consist of either secondary electrons (SE), which are produced due to the ionization of a target material atom and escape from the outer surface of the target, or backscattered electrons (BSE) from the beam itself. SEs usually have a low energy (<50 eV) and the amount of SE per incident electron of the beam is governed by the beam energy. These SE do not take part in the heating of the target. For the case of graphite, the average secondary electron emission yield has been experimentally determined to be 0.273, which amounts to ~1% of the irradiated beam energy (Kanter, 1961; Nishiwaki and Kato, 2005; Voreades, 1976). BSE are reflected elastically by the surface of the target and contribute a very small amount of energy transferred to the target. The average BSE coefficient for an electron beam incident on a graphite target at an angle of 45º is nearly ~40% (Bishop, 1967; Darlington and Cosslett, 1972; El-Gomati and Assa'd, 1998). Finally, it can also be noted that no electrons of the beam are transmitted through the target as it is thick enough (order of few millimeters). In order to account for energy losses, the fraction of beam electrons that is effectively used during ablation is taken into account by applying an efficiency factor η (< 1) to Equation (35). In the literature, a wide range of values are reported for η between 0.2 and 0.8 (Koleva, 2005; Qin et al., 2003). Accordingly, the calculations are carried out by using four values of η, viz., 0.2, 0.4, 0.6, and 0.8, whereby

$$Q(x,t) = \eta q(x,t) \tag{36}$$

3.2.5 One-Dimensional Assumption

The thermal diffusion length is used to explain the one-dimensional assumption considered for this case. The model is based on calculating the amount of heat that would flow along the target depth of the beam-irradiated region by using the thermal diffusivity at room temperature and the full duration of the pulse, t. The length of heat diffusion of the beam irradiated region can be calculated by (Carslaw and Jaeger, 1983; Ready, 1971):

$$L_d = \sqrt{2\left(\frac{k}{\rho C_p}\right)t} \tag{37}$$

Using the room temperature density, specific heat capacity, thermal conductivity and time scale of pulse duration of 100 ns, Equation (37) gives

$$L_d = 1.068\,\mu m \tag{38}$$

Bearing in mind that the diameter of the electron beam *(d_b)* is ~ 3.17 mm, it is clear that the ratio $d_b/L_d \gg 1$. Accordingly, the assumption of a one-dimensional heat conduction molded is a valid one under the prevailing conditions of this study.

3.3 Model of Plasma Plume Expansion

Expansion of plasma plume into a background gas is a critical process in PEBA. It can be divided into two different regimes: (i) plasma plume formation and initial expansion during the beam lifetime, and (ii) plasma plume expansion after the termination of the beam pulse. Since plasma plays an important part in defining the properties of the thin films, the magnitude of the kinetic energy of the particles in the expanding plasma plume and how it is affected by the pressure of a background gas will influence the nature and energy of the particles impinging on the substrate

surface, and, as a result, will control the quality and properties of deposited thin films (Mahmood et al., 2009). In PEBA, the pressure of the background gas (4–30 mTorr) is an essential requirement for the optimum operation of the pulsed electron beam source (PEBS).

The initial expansion of plasma plume in a background gas is nearly similar to an expansion in vacuum due to the very high driving pressure (~1 kbar). As the plasma plume moves in a perpendicular direction away from the target, the expansion regime near the substrate is mainly governed by the interaction processes among the plasma plume and the background gas. At low background gas pressures, the plasma plume expansion is mostly controlled by diffusion and collisions with the background gas. Collisions cause the ablated particles to thermalize. The collective effects (i.e., compression shock and mixed plasma) caused by the interaction of plasma plume and background gas can be disregarded at lower background gas pressure. Moreover, the background gas at low pressures usually does not have a significant effect on the expansion, as the plume may continue to expand after an initial acceleration stage of a few millimeters. After this stage, the velocity of expanding plume head remains almost constant in any direction.

3.3.1 Plasma Plume Expansion in the Presence of a Background Gas

The plasma plume induced by electron beam can be assumed as a viscous compressible and non-dissipative gas composed of electrons, ions and neutral atoms. For this case, the plasma plume expansion in a gas atmosphere can be mathematically described by the one-dimensional axisymmetric compressible Navier-Stokes equations for a mixture. This set of gas-dynamics equations also includes the effects of mass transfer, thermal conduction and viscosity. The equations of gas-dynamics consisting of mass conservation, momentum and energy transfer are as follows (Zel'dovich and Raizer, 1966; Bird et al., 2002)

$$\frac{\partial \rho_p}{\partial t} = -\frac{\partial}{\partial x}(\rho_p u) \tag{39}$$

$$\frac{\partial \rho_p u}{\partial t} = -\frac{\partial}{\partial x}(\rho_p uu) - \frac{\partial P}{\partial x} - \frac{\partial \bar{\bar{\tau}}}{\partial x} \tag{40}$$

$$\frac{\partial \rho_p E_p}{\partial t} = -\frac{\partial}{\partial x}(\rho_p E_p u) - \frac{\partial q}{\partial x} - \frac{\partial}{\partial x}(Pu) - \frac{\partial}{\partial x}(\bar{\bar{\tau}}\, u) \tag{41}$$

where ρ_p is the overall density of the ablated plume, u is the velocity of the ablated plume, P is the total pressure of the ablated plume, $\bar{\bar{\tau}}$ is the viscous shear stress tensor, E_p is the total specific energy of the ablated plume, and q is the heat flux due to conduction. Assuming that the plasma plume follows the ideal gas law, the total pressure can be given by

$$P = (1 + x_e) n_p k_B T_p \tag{42}$$

where $n_p = \rho_p / m$ is the number density of the ablated plume, x_e is the partial fraction of electrons in ablated plume, and T_p is the temperature of ablated plume.

The viscous shear stress tensor $\bar{\bar{\tau}}$ can be expressed as

$$\bar{\bar{\tau}} = -\frac{4}{3}\mu_p \frac{\partial u}{\partial x} \tag{43}$$

where μ_p is the viscosity of the ions and atoms in the ablated plume. The viscosity μ_p for the ablated plume is given as

$$\mu_p = \frac{1}{\pi {d_p}^2}\sqrt{\frac{m k_B T_p}{\pi}} \tag{44}$$

where d_p and m are the diameter and mass of target particle in the ablated plume.

The total specific energy of the ablated plume E_p can be expressed by

$$E_p = \mathcal{E} + \frac{1}{2} u^2 \tag{45}$$

where $\mathcal{E}$ is the specific internal energy, which can be defined as follows,

$$\rho_p \mathcal{E} = n_p \left[\frac{3}{2} (1 + x_e) k_B T_p + IP_1 x_1 + (IP_1 + IP_2) x_2 \right] \tag{46}$$

where IP_1 and IP_2 are the first and second ionization energy of carbon, respectively. x_1 is the partial fraction of singly charged ions (C^+), and x_2 is the partial fraction of doubly charged ions (C^{2+}).

The heat flux due to conduction q is given by

$$q = -\left(\kappa_p + \kappa_e\right) \frac{\partial T_p}{\partial x} \tag{47}$$

where κ_p is the thermal conductivity of the ablated plume particles, and κ_e is the thermal conductivity of the electrons. The thermal conductivity κ_p for the ablated plume particles is expressed as

$$\kappa_p = \frac{1}{{d_p}^2} \sqrt{\frac{{k_B}^3 T_p}{\pi^3 m}} \tag{48}$$

and the thermal conductivity κ_e for the electrons can be calculated by (Mitchner and Kruger, 1972),

$$\kappa_e = 3.2 \frac{{k_B}^2 T_p n_e}{m_e \bar{\nu}} \tag{49}$$

where n_e is the overall electron number density $\left(n_e = n_p x_e\right)$, m_e is the mass of electron and $\bar{\nu}$ is the effective electron collision frequency.

The effective electron collision frequency $\bar{\nu}$ is estimated by (Mitchner and Kruger, 1972),

$$\bar{\nu} = \sum_i n_i Q_{ei} \tag{50}$$

where n_i $\left(n_i = n_p x_i\right)$ and Q_{ei} are the number density of species i and effective electron-ion momentum transfer collision cross-section, respectively. The effective electron-ion momentum transfer collision cross-section, Q_{ei}, is expressed as

$$Q_{ei} = \frac{4(2\pi)^{1/2}}{3}\left(\frac{m_e}{k_B T_p}\right)^{3/2}\left(\frac{Z_i e^2}{4\pi\epsilon_o m_e}\right)^2 ln\Lambda_i \tag{51}$$

where Z_i is the charge state of species i, e is the elementary electric charge, ϵ_o is the permittivity of free space, and Λ_i is the Coulomb logarithm of species i. The Coulomb logarithm can be described as follows

$$\Lambda_i = \frac{3}{2Z_i(n_e\pi)^{1/2}}\left(\frac{4\pi\epsilon_o k_B T_p}{e^2}\right)^{3/2} \tag{52}$$

3.3.2 Plasma Generation

During pulse duration, electron beam irradiation increases the target surface temperature and the plasma plume expands steadily with increasing temperature and density. As plasma plume temperature and density continue to increase, the atoms will collide with each other and local thermal equilibrium (LTE) assumption can be adopted for each volume element. This indicates that thermal equilibrium is attained among ions, electrons, and neutral atoms in an adequately

small region of the plasma plume. That is, atoms can be distinguished by a single common temperature. For plasma in LTE, the distribution and population of ionized atoms conforms to the Saha-Eggert equation (Mitchner and Kruger, 1972). In this case, two Saha-Eggert equations are employed to calculate the number density of ionized atoms (C^+ and C^{2+}) and electrons, which are defined as,

$$\frac{x_1 x_e}{x_0} = 2\frac{g_1}{g_0}\frac{1}{n_p}\left(\frac{2\pi m_e k_B T_p}{h^2}\right)^{3/2} exp\left(-\frac{IP_1}{k_B T_p}\right) \tag{53}$$

$$\frac{x_2 x_e}{x_1} = 2\frac{g_2}{g_1}\frac{1}{n_p}\left(\frac{2\pi m_e k_B T_p}{h^2}\right)^{3/2} exp\left(-\frac{IP_2}{k_B T_p}\right) \tag{54}$$

where g_0, g_1, and g_2 are the degeneracy factors of a neutral, singly ionized (C^+), and doubly ionized atoms (C^{2+}), respectively. In order to solve the system of Saha-Eggert equations (53) and (54), two additional equations of conservation are required: (a) conservation of ions, which involves a consistent number of heavy particles,

$$x_0 + x_1 + x_2 = 1 \tag{55}$$

and (b) conservation of charge (electro-neutrality)

$$x_1 + 2x_2 = x_e \tag{56}$$

3.3.3 Initial and Boundary Conditions

The gas dynamics for plasma plume expansion and the heat conduction at the target surface are connected together through the Knudsen layer adjacent to target surface. The temperature, pressure, and density of the particles exiting the KL can be coupled with the density, temperature, and pressure at the target surface by the following relations (Knight, 1979),

$$\frac{T_k}{T_s} = 0.67 \tag{57}$$

$$\frac{P_k}{P_s} = 0.21 \tag{58}$$

$$\frac{\rho_k}{\rho_s} = 0.31 \tag{59}$$

where T_k, P_k, and ρ_k are the temperature, pressure, and density of the particles leaving the Knudsen layer, respectively, T_s, P_s, and ρ_s are the target surface temperature, pressure, and density of the target, respectively. The velocity leaving the Knudsen layer is assumed to be equal to the velocity of sound (due to supersonic flow), which is determined by the temperature of the ablated particles (T_k) (Knight, 1979),

$$u_k = \sqrt{\frac{\gamma_v k_B T_k}{m}} M \tag{60}$$

The boundary conditions at $x = L_s$ are given as,

$$\{T_p = 0\ K, \rho_p = 0\ kg/m^3, u = 0\ m/s\ \} \tag{61}$$

The initial conditions for the plasma plume expansion, are assumed according to ambient conditions as of background gas and given as,

$$\{T_p = 300\ K, \rho_p = 0\ kg/m^3, u = 0\ m/s\ \} \qquad at\ t = 0 \tag{62}$$

$$\{P_g = 0.6\ Pa, \rho_g = 1.512 \times 10^{-6}\ kg/m^3\} \qquad at\ t = 0 \tag{63}$$

where P_g and ρ_g are the pressure and density of the background gas (argon), respectively.

When plasma plume starts to expand towards the substrate, the boundary condition at this stage is specified by the energy balance at the target surface, which connects the heat conduction and gas-dynamics equations,

$$u_k \left[\rho_k L_v + \rho_p \mathcal{E} + \frac{1}{2}\rho_p {u_k}^2 + P_k\right] - k_{v/l} \frac{\partial T}{\partial x}\Big|_{x=0} = Q_s(t) \qquad \left(t_{sb/m} < t \leq \tau\right) \qquad (64)$$

In this case, the surface recession velocity $u(t)$ can be obtained by the mass balance,

$$\rho_{v/l} u(t) = \rho_k u_k \qquad (65)$$

The heat conduction equations for electron beam-target interaction and gas-dynamics equations for plasma plume expansion in a gas atmosphere have been set up and solved using the finite element method in COMSOL Multiphysics®. Space mesh and time step have been refined until the calculation results have become independent of discretization steps. The heat source term used in the electron beam-target interaction model is solved by a Monte Carlo scheme simulating electron trajectories in solids (CASINO).

3.4 Thermo-Physical Properties of Graphite

In the case of graphite, the thermal conductivity, specific heat capacity and density depend strongly on temperature. Numerous studies have estimated these thermodynamics properties and used appropriate mathematical expressions to fit their experimental data (Abrahamson, 1974; Kelly, 1981; Leider et al., 1973; Lutcov et al., 1970; Null et al., 1973; Reynolds, 1968). The estimated mathematical expressions for the thermodynamics properties of graphite can be given as,

(a) thermal conductivity ($W/m\,K$) (Lutcov et al., 1970; Reynolds, 1968),

$$k_a = \left(\frac{26760}{T}\right) \qquad (66)$$

$$k_c = -0.101 + 181.022T^{-0.53} \tag{67}$$

$$k = \left(k_a{}^2 k_c\right)^{1/3} \tag{68}$$

(b) specific heat capacity $(J/kg\ K)$ (Kelly, 1981; Leider et al., 1973),

$$C_p = 1357.1190 + 0.4381T - \frac{7.1624 \times 10^5}{T^2} (T < 1000\ K) \tag{69}$$

$$C_p = 2076.8526 + 0.04073T - \frac{5.9247 \times 10^3}{T} - \frac{3.0383 \times 10^8}{T^2} (T > 1000\ K) \tag{70}$$

(c) density (kg/m^3) (Kelly, 1981; Reynolds, 1968),

$$\rho = \rho_{T_0} \left(\frac{c}{c_{T_0}}\right)^{-1} \tag{71}$$

where c is the thermal expansion along the c-axis. It has been observed from experimental studies that expansion occurs only along the c-axis in graphite. According to Baskin and Meyer (1955) study, thermal expansion in graphite along the c-axis can be expressed as,

$$c/_2 = 3.357 + 91.9 \times 10^{-6}(T - 273) + 5.3 \times 10^{-9}(T - 273)^2 \tag{72}$$

The data on the physical properties of the graphite target used in this study are summarized in Table 3.1.

Table 3.1: Physical properties of graphite target (Chung, 2002; Mantell, 1968; Pappis and Blum, 1961; Pierson, 1994).

Parameter	**Value**
Sublimation temperature, $T_{sb}(K)$	4200
Melting temperature, $T_m(K)$	4200
Boiling temperature, $T_b(K)$	4500
Latent heat of vaporization, $L_v\ (kJ/kg)$	59.742×10^3
Latent heat of fusion, $L_v\ (kJ/kg)$	7.5×10^3
Average mass of atom, $m\ (kg)$	1.9944×10^{-26}
Two adjacent crystalline layer, $d_l\ (\text{Å})$	3.354
Average length of the diffusive jump of atoms in the liquid, $\Lambda\ (\text{Å})$	1.42
Activation energy of the atoms for diffusive motion in the liquid, $Q_A\ (kJ/kg)$	104.433
Gas constant of vapor, $R_g\ (J/kg\ K)$	692.88
Atomic number, Z	6
Atomic weight, A	12
Diameter of the particle, $d_p\ (\text{Å})$	2.1
First ionization energy, $IP_1\ (eV)$	11.260
Second ionization energy, $IP_2\ (eV)$	24.384
Degeneracy factors of a neutral, g_0	9
Degeneracy factors of a singly ionized atom, g_1	6
Degeneracy factors of a doubly ionized atom, g_2	1

Chapter 4

4 Target Ablation Results and Discussion

4.1 Introduction

Thin film deposition during PEBA is significantly influenced by many factors such as power density, beam energy, pulse frequency, background gas, pressure of background gas, and target to substrate distance. Target ablation is mainly affected by two critical factors, which are beam energy and power density delivered to the target surface. In order to thoroughly assess PEBA for the deposition of thin films with superior properties, it is essential to investigate how the critical parameters affect the ablation process. In this chapter, the effect of beam efficiency (efficiency factor), accelerating voltage (beam energy), and beam power density (beam tube output-target surface distance) on graphite target ablation is presented. The Knudsen boundary layer effect on ablation is also discussed.

4.2 One-Dimensional Assumption

The ratio between different beam diameters and the heat diffusion length inside the target surface after irradiation is represented in Figure 4.1. For this case, heat diffusion length inside the target surface after irradiation is calculated by equation (37). For the sake of assessing the effect of different beam diameters on heat diffusion length, seven various values of beam diameters ranging from 1 nm to 1 mm have been considered. It can be seen for the small beam diameters, i.e., 1 nm to 100 nm, that the ratio d_b/L_d is very small and that heat diffusion under these conditions is strongly two-dimensional. This might be due to the fact that the electrons lose a major portion of their energy by experiencing elastic collisions, which results in significant changes in the initial direction of the electrons. As a result, lateral heat flow diffusion area might expand steadily. For

large beam diameters, i.e., 1 µm to 1 mm, the ratio d_b/L_d is always equal to or greater than one. It can be observed for beam diameters larger than 1 µm, the ratio d_b/L_d is far greater than one. Beyond this diameter value, the heat diffusion inside the target surface is a function of depth, x. Accordingly, at higher values of beam diameter, the lateral diffusion of electrons becomes negligible and the heat flow is only depth dependent.

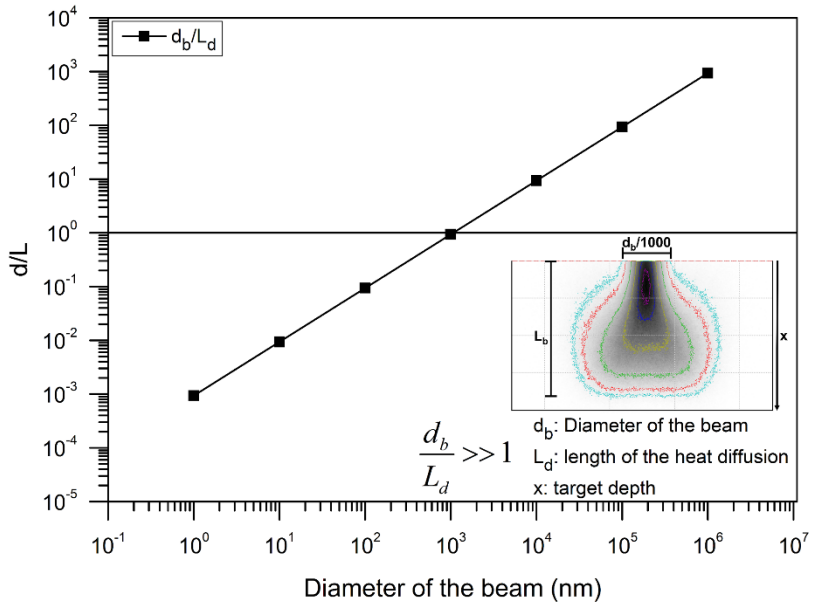

Figure 4.1: Ratio between different beam diameters and heat flow diffusion lengths.

4.3 Heat Source

In contrast to pulsed laser ablation, the penetration depth of electrons is much larger in PEBA, hinting at drastic differences in the thermodynamics of both ablation types (Gilgenbach et al. 1999). The energy deposited by each group of electrons for various accelerating voltages along the diffusion depth is calculated by equations (32) and (33), and reported in Figure 4.2. It can be seen that the maximum deposited energy for the beam operating at different accelerating voltages ranges approximately between one-fifth (highly energetic electrons) and one-seventh (weakly energetic electrons) of the total penetration depth, i.e., the penetration depth of the less energetic

electrons is shallower (closer to the target surface). Figure 4.3 shows the number of thermalized electrons inside the target along the diffusion depth and is estimated by equation (32). The most probable diffusion depth reached by each group of electrons is indicated on the same figure (Figure 4.3) and corresponds to the maximum of each curve.

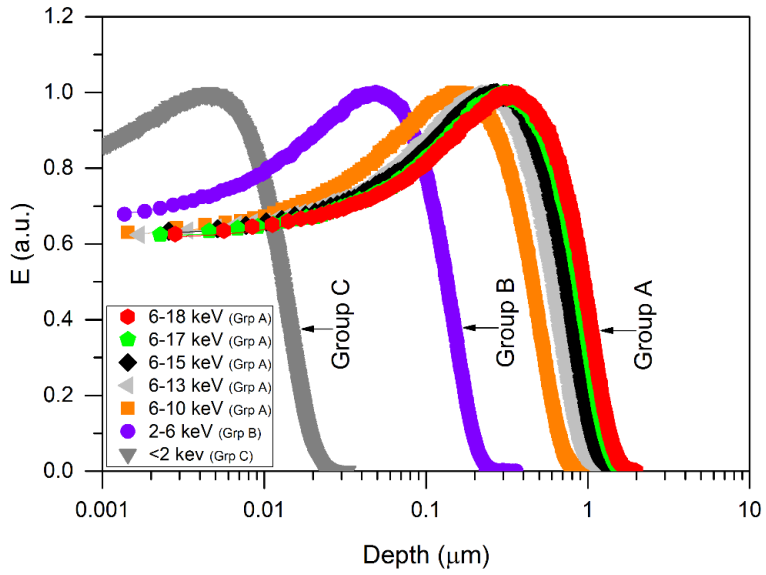

Figure 4.2: Energy deposited by each group of electrons for various accelerating voltages along the penetration depth in the target. The data are fitted into polynomial functions of degree indicated by solid lines.

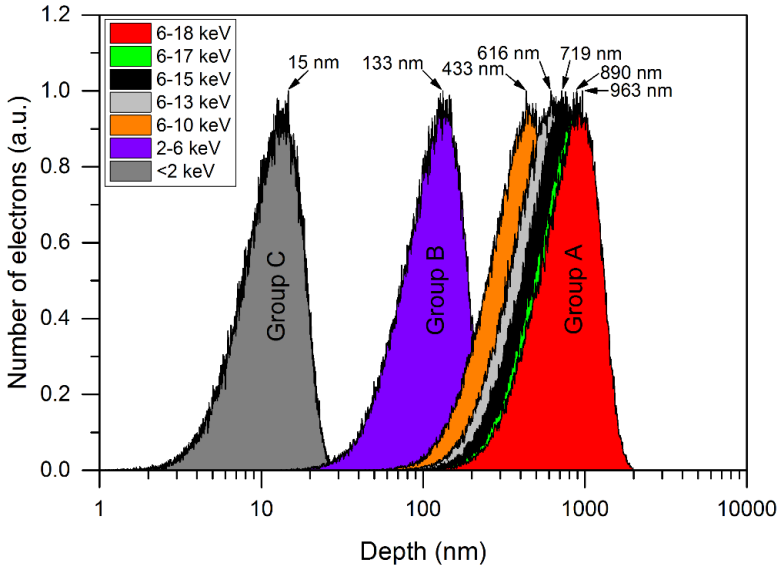

Figure 4.3: Distribution of the number of electrons along the penetration depth in the target.

4.4 Heating and Sublimation

In this section, modeling results of heating and sublimation of a graphite target upon interaction with a nanosecond polyenergetic electron beam are presented. The results account for the effect of the Knudsen boundary layer, beam efficiency (η), accelerating voltage, and beam power density (beam tube output-target surface distance).

4.4.1 Beam Efficiency

Due to the rapid deposition of electron beam radiation onto the target surface, the target temperature, which is initially at ambient temperature (298 K), rises very quickly. The temperature profiles of the target surface for different values of the efficiency factor are calculated through equations (5) – (13) and illustrated for the entire pulse width for an accelerating voltage of 15 kV in Figure 4.4. For the sake of assessing the effect of the efficiency factor on ablation, four values of η, viz., 0.2, 0.4, 0.6, and 0.8

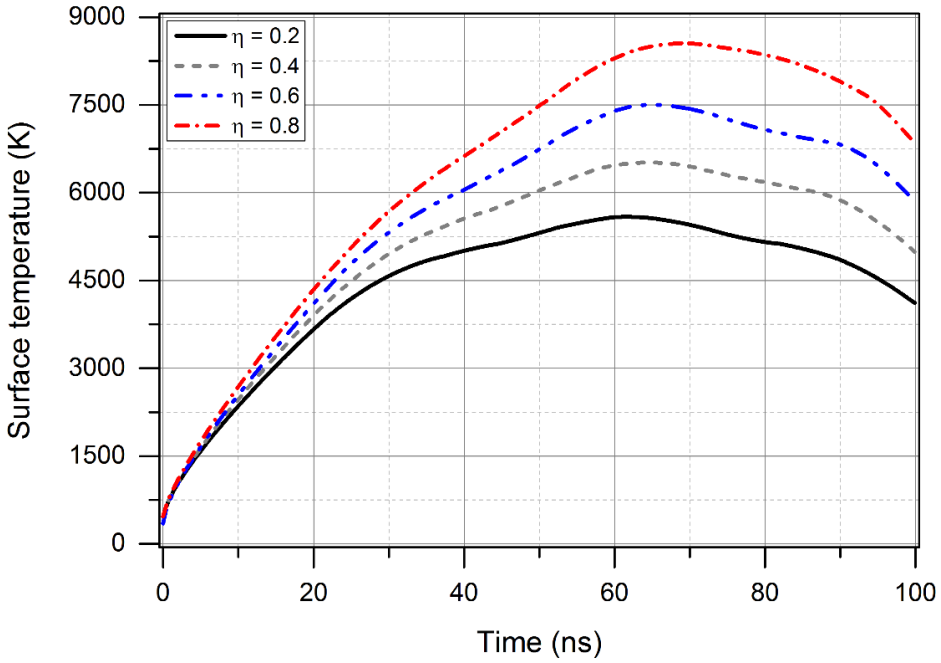

Figure 4.4: Target surface temperature for various beam efficiencies as a function of time during pulse duration as is the case for sublimation.

have been considered in the present calculations (Figure 4.4). As it can be seen, the effect of the efficiency factor is clearly noticeable. It can be observed that the surface temperature increases slowly for lower values *of* η, viz, for 0.2 and 0.4. For instance, for an efficiency of 0.4, the temperature rises gradually during the pulse duration and reaches up to 6500 K. At lower values of beam efficiency ($\eta = 0.2$), the maximum surface temperature is not sufficiently high to cause a substantial amount of vaporization of the target surface (discussed later in Figure 4.9) due to corresponding lower saturation vapor pressure, relatively to high values of the efficiency. This can be explained by the fact that a large portion of the impinging electrons is potentially backscattered off the target, leading to poor ablation performance. For high efficiencies, i.e., 0.6 and 0.8, the heating rate increases very quickly resulting in higher surface temperature, i.e., 7500 K and 8500 K, respectively. Subsequently, the temperature starts to drop, although this decrease is considerably slower than the initial increase. As it can be seen in Figure 4.4, the surface temperature is still greater than the sublimation temperature of 4200 K at the end of the pulse. This is likely due to the polyenergetic character of the electron beam. Low energy electrons appearing at the end of the pulse induce a power density of ~10^6 W/cm^2 as a result of high beam current and short penetration depths in the target, which, in turn, sustains the ablation process.

The target temperature along the electrons penetration depth is calculated through equations (5) – (13) and presented in Figure 4.5 for various time intervals after target bombardment for an efficiency factor 0.6. It can be observed that the maximum temperature is reached at the target surface and decreases along the depth. As shown in Figure 4.3, due to the polyenergetic character of the beam, the majority of the electrons generated by the beam for an accelerating voltage of 15 kV have low energies. As a result, the beam energy is mostly absorbed in a narrow surface layer

of the target, resulting in rapid increase in surface temperature, whereas the temperature of the subsurface region further into the target remains relatively unaffected.

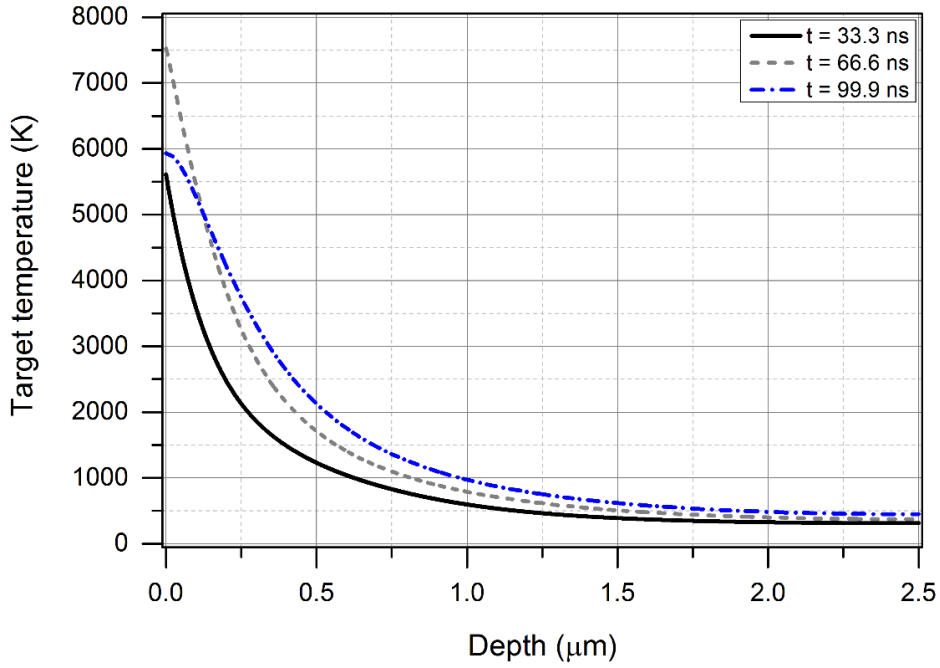

Figure 4.5: Target surface temperature as a function of penetration depth for different time intervals for an efficiency of 0.6 as is the case for sublimation.

The target surface recession velocity, defined by equation (26), has been calculated assuming a back flux coefficient of 0.18 as noted previously. As illustrated in Figure 4.6, for an efficiency of 0.8, the recession velocity reaches a maximum value of 290 m/s at about 65 ns, i.e., when the surface temperature of the target is at maximum value (8500 K). Beyond the latter, the surface recession velocity drops as the target surface cools down. For all values of the efficiency, the surface begins to vaporize within 30 ns from the pulse start. The surface vaporization is delayed in the case of a pulsed electron beam (relatively to PLA) mainly due to the fact that the pulse width of the present electron beam is five times larger than that of a pulsed excimer laser, resulting in an increase in the thermal diffusion depth of the electrons. Longer pulse widths and greater thermal diffusion depths lead to an increase in the effective depth of energy deposition and prolongation

of the onset time for ablation and plasma formation during PEBA (Gilgenbach et al, 1999). As anticipated, similar trends can be observed for the other values of the efficiency.

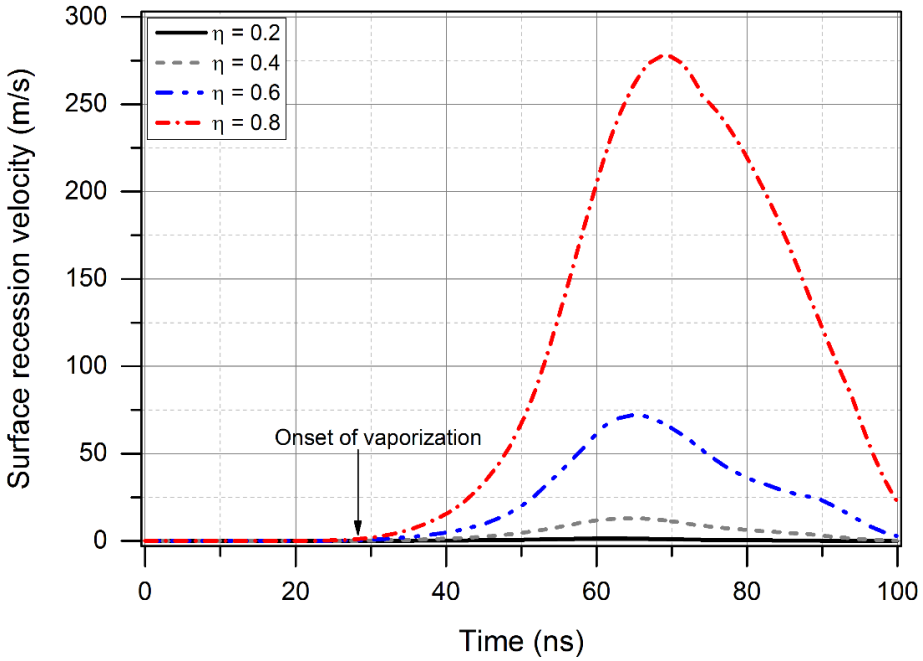

Figure 4.6: Surface recession velocity for back flux coefficient of 0.18 and for various beam efficiencies as a function of time during pulse duration as is the case for sublimation.

The Knudsen layer exists at high vaporization rates, where the vapors at the target surface near the solid-gas phase boundary are in isotropic distribution. For an efficiency factor of 0.8, the effects of KL, defined by equations (28) – (31), and back flux on the surface recession velocity for the entire pulse width are illustrated in Figure 4.7. When back flux is considered only, the recession velocity varies smoothly during the pulse duration, and is continuously positive. In contrast, when KL is considered, the vapors velocity within this thin layer changes in a peculiar way with time. During the bulk of the pulse duration, the recession velocity is mostly positive. At end of the pulse width (after 90 ns), the recession velocity adjacent to the surface exhibits an inversion, i.e., shifts from a positive to a negative value. This inversion is likely the result of more energy losses (owing to heat conduction and vaporization) than energy gain (absorbed beam energy) at the target surface,

which results in a negative velocity. The latter can be explained based on the observation that when vaporization decreases, the vapor pressure is reduced at the target surface, resulting in the development of a pressure gradient and a backward flow of the vapors towards the surface. A similar trend, i.e., negative recession velocity, has been observed during nanosecond laser ablation (Alexiades and Autrique, 2010). According to calculation results shown in Figure 4.7, the fraction of ablated particles returning back to the target surface seems to be overestimated when KL is considered. As expected, the effect of KL on the recession velocity is only appreciable for higher values of the beam efficiency, viz., 0.8, in this case. Surface recession velocity estimation for a back flux coefficient of 0.18 appears to be more accurate than its counterpart when the KL is accounted for as confirmed from experimental data (Morozov, 2004).

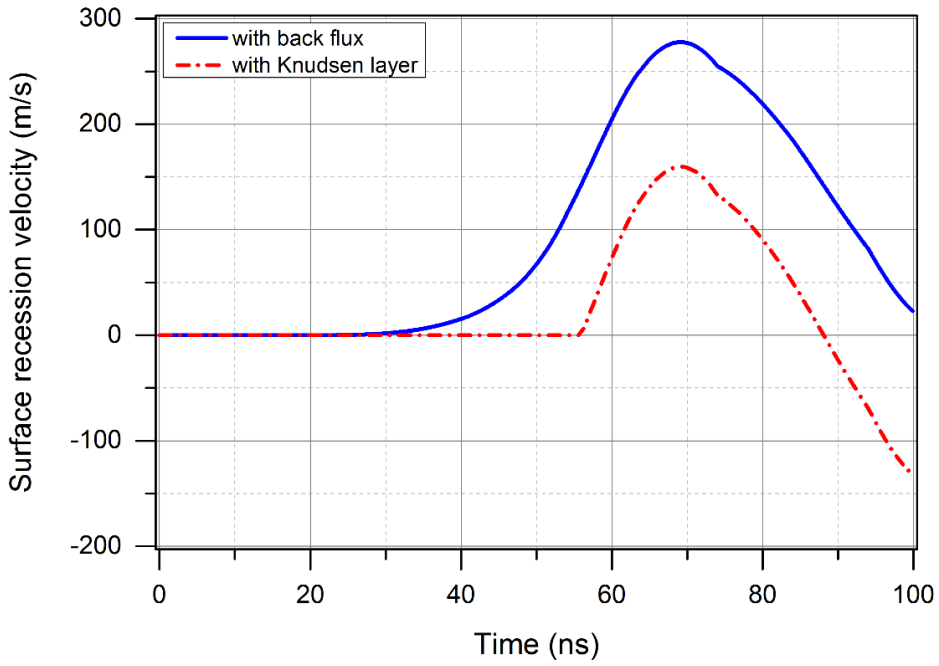

Figure 4.7: Effect of the Knudsen layer and back flux coefficient on surface recession velocity as a function of pulse duration for an efficiency of 0.8 as is the case for sublimation.

The ablation depth and ablated can be obtained by integrating the surface recession velocity, given by equation (26), over the pulse duration. Similarly, the ablated mass per unit area has been calculated by integrating the target material density, given by equation (71), times the recession velocity over the pulse duration. These are plotted as a function of pulse duration in Figures 4.8 and 4.9, respectively. As expected for the case of 0.8, the calculated ablation depth and rate are larger than for lower values of the beam efficiency. The calculated ablation depth is around 10 μm and the ablated mass per unit area is about 17 μg/mm^2 for an efficiency of 0.8. Similar profiles of both ablation depth and rate for the lower values of the efficiency can be observed. It can be seen that the recession velocity estimated at an efficiency of 0.8 carries a large uncertainty as a result of assuming that a large fraction of beam electrons is used during ablation. Therefore, ablation appears to be either overestimated for an efficiency of 0.8 or underestimated for low values of beam efficiency, i.e., η = 0.2-0.4. For an efficiency of 0.6, the estimated ablated mass seems to be in accordance with reported experimental data as discussed later.

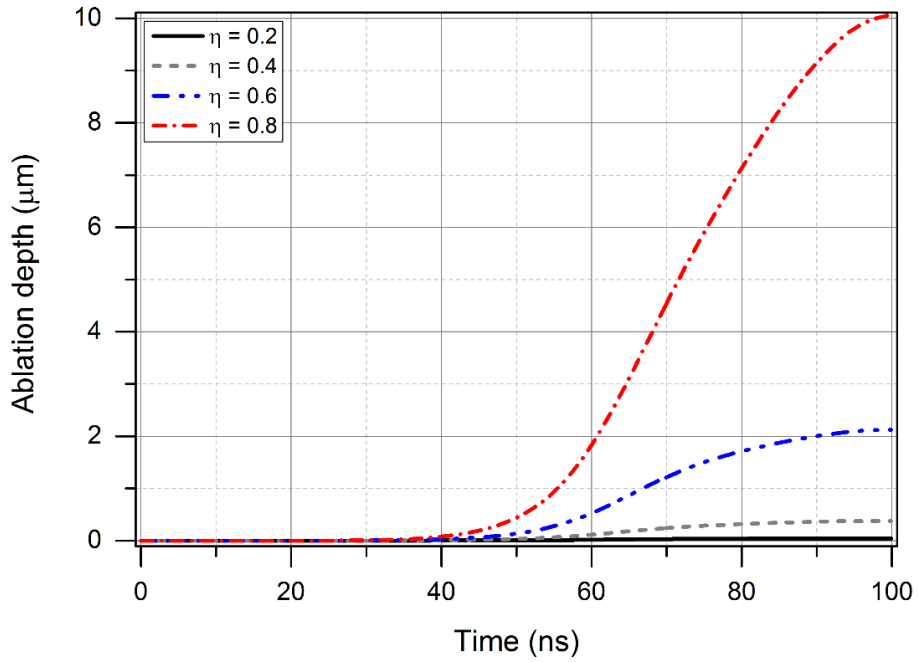

Figure 4.8: Ablation depth for various efficiencies as a function of time during pulse duration as is the case for sublimation.

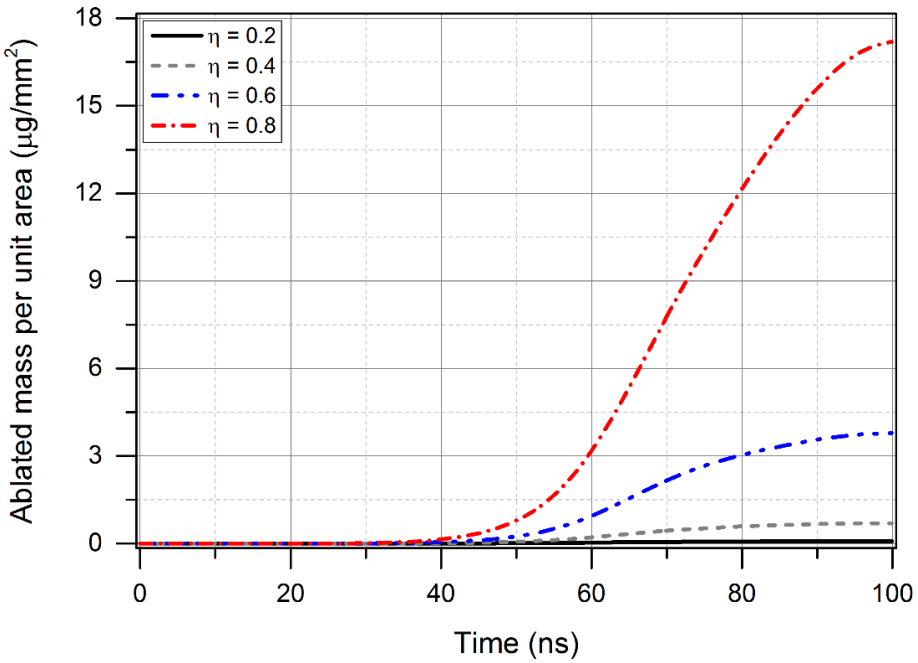

Figure 4.9: Ablated mass per unit area for various efficiencies as a function of time during pulse duration as is the case for sublimation.

4.4.2 Beam Power Density

An effective approach to enhance the heating rate in PEBA is by the provision of a large beam power density onto the target surface through the reduction of the beam spot cross-sectional area. In order to enhance the beam power density, the target surface must be as close as practically possible to the electron beam tube output. The effect of the distance between the beam tube output and target surface on ablation can be assessed by modifying the beam spot radius (r) in Eqs. 34 and 35, Chapter 3. Different values of the radius of the beam spot used in this study are 2.0, 2.6, 2.9 and 3.5 mm. Based on geometrical considerations, the values r, viz., 2.0 mm, 2.6 mm, 2.9 mm, and 3.5 mm correspond to values of the distance between the beam tube output and target surface (d) of 4.0 mm, 6.0 mm, 8.0 mm, and 10.0 mm, respectively. Figures 4.10, 4.11, 4.12 and 4.13 show the calculated surface temperature, surface recession velocity, ablation depth and ablated mass per unit area, respectively, for various values of the distance between the tube output and

target surface for the entire pulse width at an efficiency of 0.6. For long distances, namely, $r \geq 6$ mm, it can be seen from Figure 4.10 that the heating rate and surface temperature rise very slowly. For instance, the temperature reaches 5400 K at a distance of 6 mm. As illustrated in Figure 4.11, surface recession velocity is quasi-insignificant at this temperature. Similarly, as shown in Figures 4.12 and 4.13, the ablation depth and ablated mass per unit area for $r \geq 6$ mm are not large enough to ablate a substantial portion of surface from the target. This is due to the fact that beam electrons deviate from their path and their energy is scattered over a widespread surface area. As a result, the beam power density decreases with increasing tube output-target surface distance, which, in turn, reduces the heating rate and ablation efficiency. It can be seen that the heating rate and surface temperature increase very quickly for a distance of 4 mm, as compared to other distances, and reaches a maximum temperature of 7500 K. As the tube output-target distance decreases, the beam electrons are less prone to deviation and the beam cross-sectional area decreases while, at the same, the beam power density on the target surface increases.

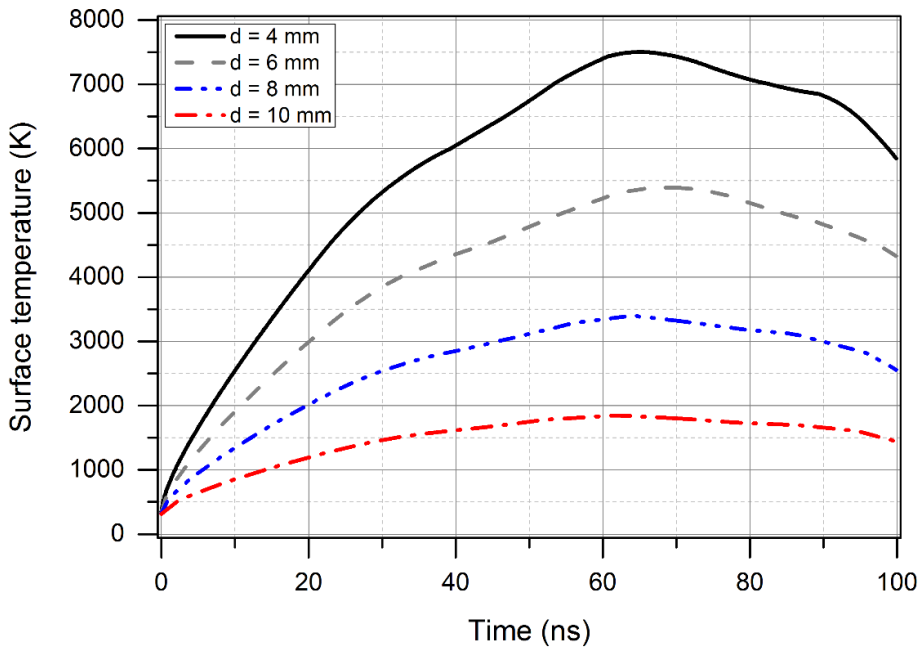

Figure 4.10: Target surface temperature for various distances between beam tube output and target surface as a function of pulse duration for an efficiency of 0.6 as is the case for sublimation.

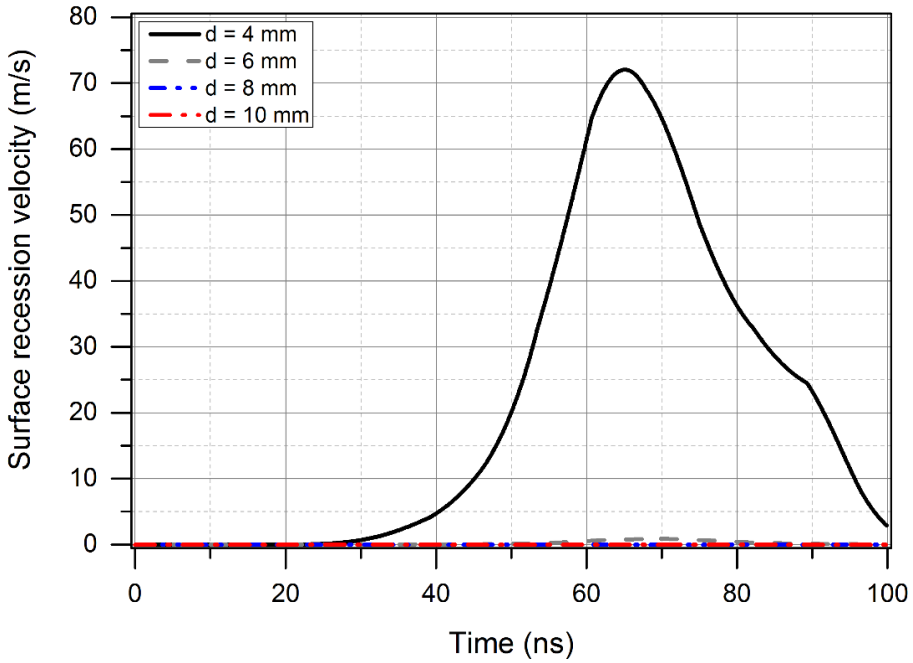

Figure 4.11: Surface recession velocity for various distances between beam tube output and target surface as a function of pulse duration for an efficiency of 0.6 as is the case for sublimation.

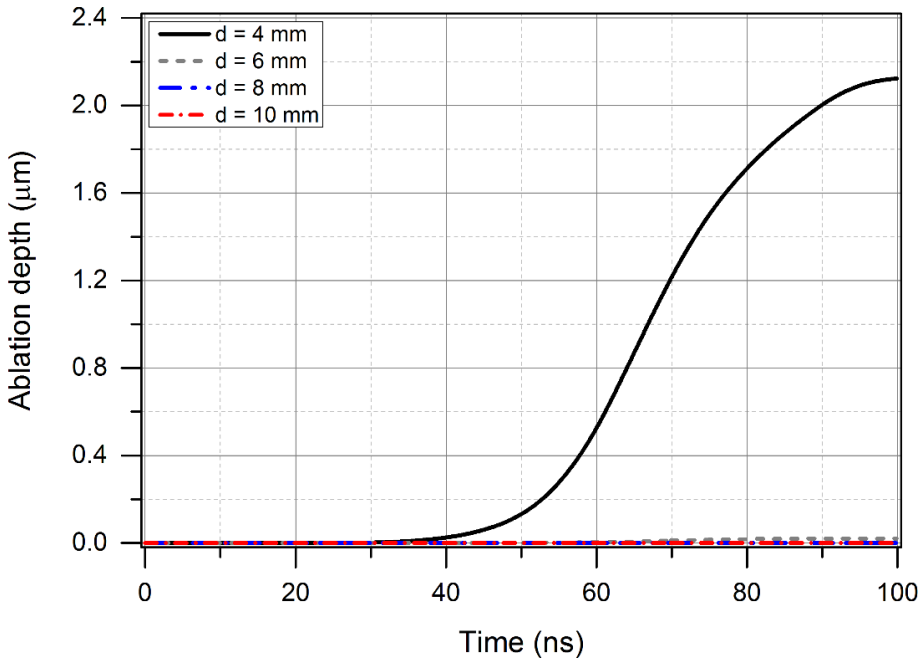

Figure 4.12: Ablation depth for various distances between beam tube output and target surface as a function of pulse duration for an efficiency of 0.6 as is the case for sublimation.

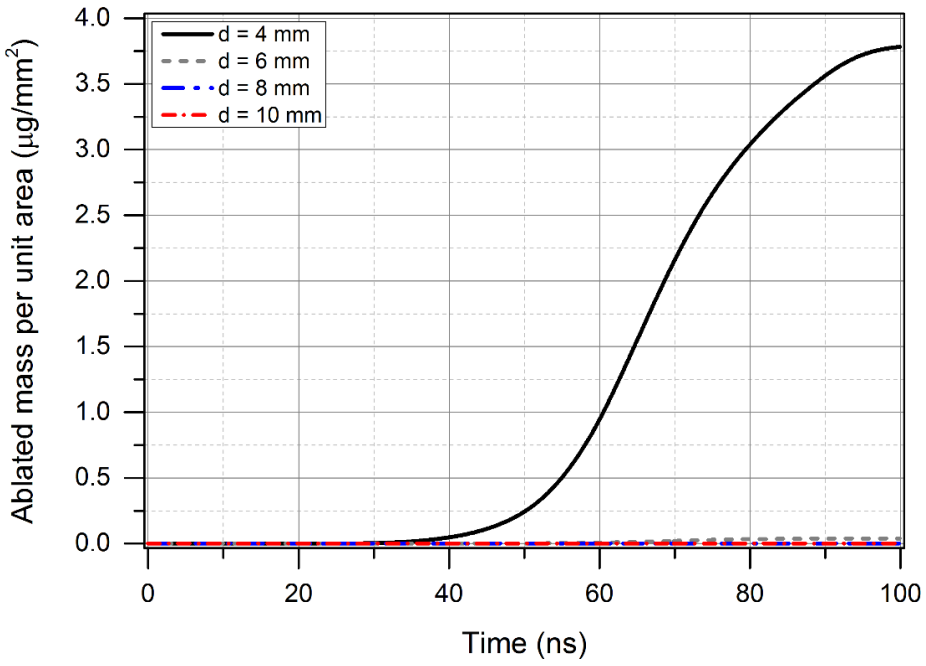

Figure 4.13: Ablated mass per unit area for various distances between beam tube output and target surface as a function of pulse duration for an efficiency of 0.6 as is the case for sublimation.

4.4.3 Accelerating Voltage

In our calculations, the target is initially at ambient room temperature (298 K). Due to the non-equilibrium electron beam energy deposition in the target material, the surface is heated very rapidly. The calculated target surface temperature for various values of the accelerating voltage is depicted for the entire pulse width (~100 ns) in Figure 4.14. It can be seen that the surface temperature and heating rate increase rapidly for the accelerating voltage in the range of 10 to 15 kV. This finding is likely due to the polyenergetic nature of the electron beam (Kowalewicz and Redel, 1995). The majority of electrons produced by the beam for the voltage in the range of 10 to 15 kV have lower energies. As a result, the maximum energy of the electrons is deposited near the target surface. The highest temperature is observed for an accelerating voltage of 15 kV at about 7500 K between 60 and 70 ns. At higher voltages, the heating rate falls off due to an increase in the penetration depth of the electrons, which offsets the intensity increase of the beam. As the

acceleration voltage increases the energy of the electrons in the beam increases while, at the same time, the highly energetic electrons will penetrate deeper in the target. This results in greater losses of the beam energy, which becomes predominant at higher voltages (above 15 kV), and eventually cancels out the effect of the acceleration voltage on the beam energy. For 17 kV, it can be seen that initially the heating rate is about the same as 15 kV, but it slightly decreases after 40 ns yielding a maximum temperature of 7300 K. The evolution of the target surface temperature with time and dependence on voltage seem to have a similar trend for all voltages except for 18 kV. At 18 kV, the temperature profile goes through a short plateau at ~20 ns corresponding to a target surface temperature of 4000 K. This is the result of phase change due to sublimation, which starts to occur around 4000 K. Afterwards, there is a sudden climb in the temperature whereby the surface temperature reaches 6700 K. For voltages lower than 18 kV, sublimation seems to occur much faster so that not plateauing of the temperature can be observed.

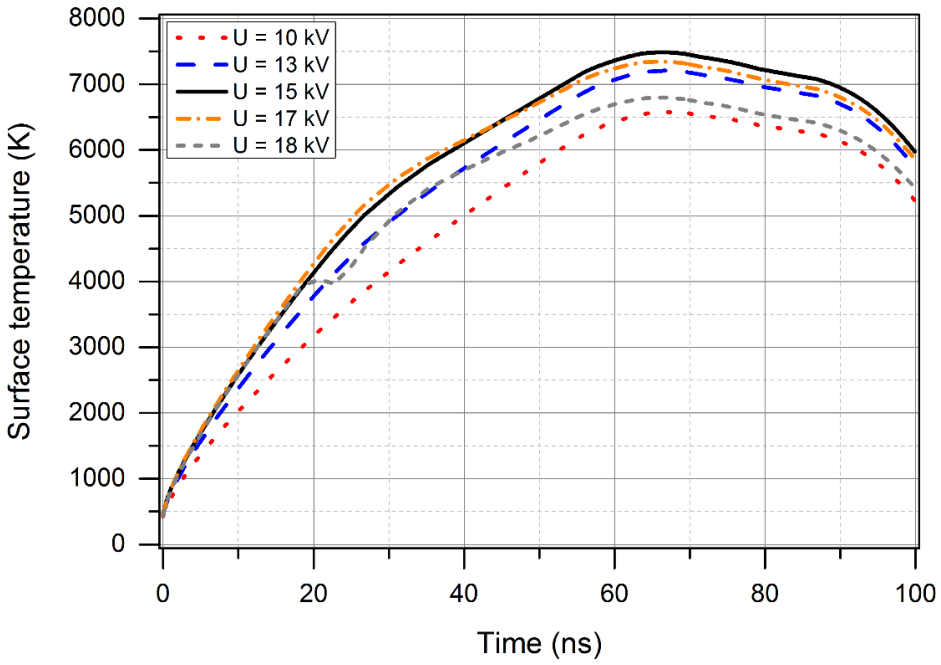

Figure 4.14: Target surface temperature for various accelerating voltages as a function of pulse duration for an efficiency of 0.6 as is the case for sublimation.

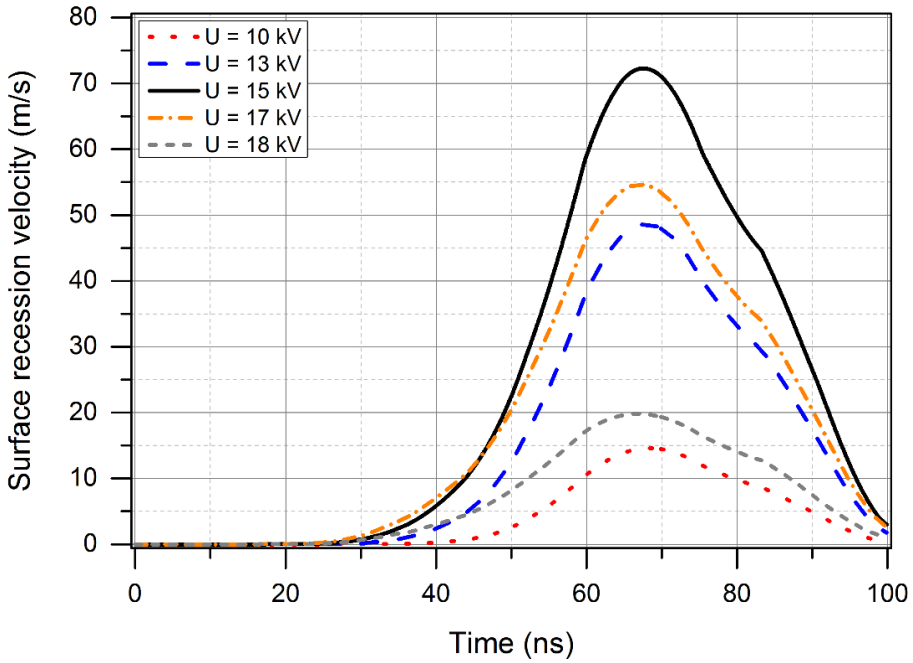

Figure 4.15: Surface recession velocity for various accelerating voltages as a function of pulse duration for an efficiency of 0.6 as is the case for sublimation.

The recession velocity from the target surface is illustrated in Figure 4.15. As can be observed, at 15 kV the recession velocity reaches a maximum value of 71 m/s at about 65 ns, i.e., when the surface temperature of the target is at maximum (7500 K). Beyond the latter, the surface front receding velocity decreases as the target surface temperature drops. A similar trend can be observed for the other values of the accelerating voltage.

As mentioned before, the ablation depth and ablated mass per unit area can be calculated from the surface receding velocity and density. These are plotted as a function of pulse duration in Figures 4.16 and 4.17, respectively. As expected, for the case of 15 kV, the calculated values of ablation depth and ablated mass per unit area are higher than at other accelerating voltage values. The calculated ablation depth is around 2.1 μm and the ablated mass is about 3.8 μg/mm^2. Similar profiles of both ablation depth and ablated mass per unit area for the remaining accelerating voltage values can be observed.

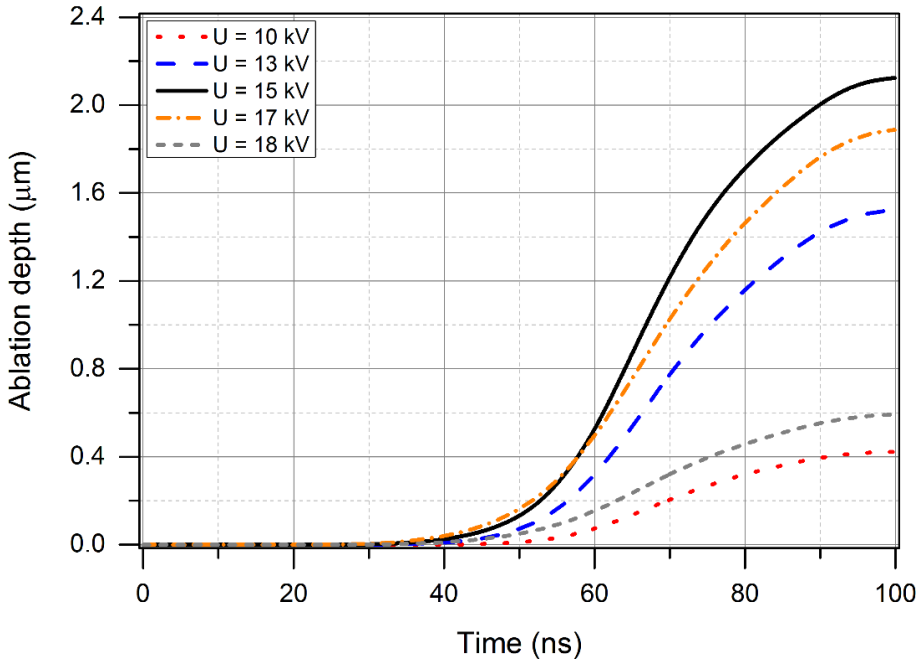

Figure 4.16: Ablation depth for various accelerating voltages as a function of pulse duration for an efficiency of 0.6 as is the case for sublimation.

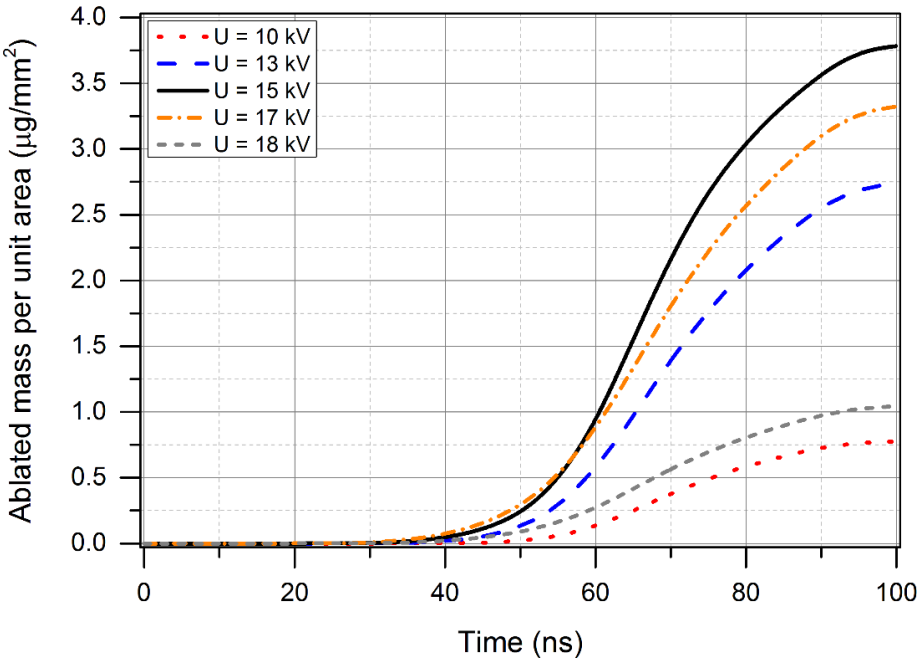

Figure 4.17: Ablated mass per unit area for various accelerating voltages as a function of pulse duration for an efficiency of 0.6 as is the case for sublimation.

4.4.4 Model Assessment

Experimental data on solid-state target ablation induced by pulsed electron beams are quite scant and much so for graphite. It has been reported that dissipated electron beam energy amounts to 30-40 % of the irradiated beam power (Gilgenbach et al., 1999; Schiller et al., 1982). Our observations, based on calculation results, that the appropriate value of beam efficiency would be around 0.6 is in quantitative agreement with the theoretical data. To validate the model, the ablation depth and ablated mass calculated for an efficiency factor value of 0.6 and accelerating voltage of 15 kV are compared with relevant experimental and theoretical data in the literature (Bulgakova and Bulgakov, 2001; Harshavardhan and Strikovski, 2005; Höbel et al., 1990; Kowalewicz and Redel, 1995; Strikovski and Harshavardhan, 2003; Strikovski et al., 2010). For this efficiency ($\eta = 0.6$), the ablated mass per unit area (mm^2) amounts to ~48 µg/pulse or ~24×10^{17} atoms/pulse, which is in good accordance with experimental data of a few tens of µg/pulse (Harshavardhan and Strikovski, 2005) or some 10^{17} atoms/pulse (Kowalewicz and Redel, 1995). Experimental results have further revealed that the ablated mass per unit area in PEBA is at least 10 times larger than its counterpart in PLA. This is the case of our model calculations where the ablated mass in PEBA is 10-20 times the rate in PLA for a graphite target (Bulgakova and Bulgakov, 2001; Harshavardhan and Strikovski, 2005). In terms of the heating rate for different values of the accelerating voltage, our results are in qualitative (no absolute values have been provided by the authors) agreement with experimental data (Strikovski and Harshavardhan, 2003; Strikovski et al., 2010). The latter suggest that the heating rate is at maximum at a voltage of about 15 kV. In terms of the ablation depth, it has been reported that the beam electrons can reach a penetration depth of 1-2 µm in the target (Harshavardhan and Strikovski, 2005; Höbel et al., 1990). This is in good agreement with our estimated ablated depth of ~2 µm as illustrated in Figure 4.8.

4.5 Heating, Melting and Vaporization

In this section, results obtained by two stage one-dimensional heat conduction model comprised of heating, melting and vaporization of a graphite target upon interaction with a nanosecond polyenergetic electron beam are presented. The effects of beam efficiency (efficiency factor), accelerating voltage, and beam power density (beam tube output-target surface distance) are accounted for and analyzed.

4.5.1 Beam Efficiency

The effect of the efficiency factor of the incident electron pulse delivered to the target surface is assessed via the target surface temperature, surface recession velocity, melt depth, ablation depth and ablated mass per unit area. To this effect, target surface temperature profiles have been calculated using equations (14) – (22) for four different values of η, viz., 0.2, 0.4, 0.6, and 0.8, at an accelerating voltage of 15 kV and a pulse width duration of ~100 ns as illustrated in Figure 4.18. It can be observed that the calculated target surface temperature varies significantly, suggesting strong dependence of ablation on beam efficiency. The beam efficiency governs the energy content of the electron pulse as explained earlier. Accordingly, with increasing the beam efficiency, the energy delivered to and deposited onto the target surface also increases. Upon increasing the efficiency factor, the maximum surface temperature rises significantly, as can be seen in Figure 4.18. This is likely due to the fact that the majority of the impinging electrons effectively interact with the target surface. A small portion of the electrons is potentially backscattered off the surface, resulting in enhanced ablation performance for high η. For low values of η, viz., 0.2 and 0.4, the rate of rise of surface temperature is quite low as small amount of energy is used for ablation. For instance, for an efficiency of 0.2, the surface temperature increases steadily during the pulse duration and reaches up to 5500 K. As the beam efficiency

increases, viz., 0.6 and 0.8, the rate of temperature rise increases very quickly. As it can be seen, for $\eta = 0.8$, the rapid heating rate leads to maximum surface temperature of 8500 K at 68 ns after the beginning of the pulse. Thereafter, the temperature begins to decline, but this temperature drop is significantly slower as compared to the initial temperature rise. Furthermore, it can be observed that at the end of the pulse, the surface temperature is quite higher than the boiling temperature of 4500 K. This can be attributed to the polyenergetic nature of the electron as pointed out before. Low energetic electrons arriving at the end of the pulse generate a power density of ~10^6 W/cm^2 due to short penetration depths in the target and high beam current, which, accordingly, withstands the ablation process. Finally, the slope of the curves suggests that the heating rate also increases substantially with an increase in the efficiency factor.

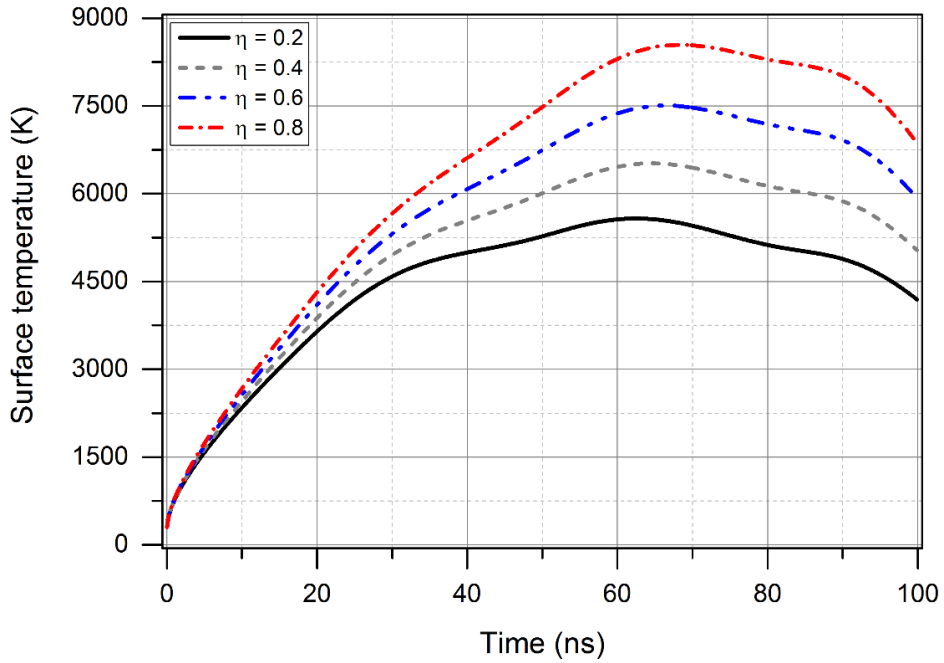

Figure 4.18: Target surface temperature for various beam efficiencies as a function of time during pulse duration as is the case for melting.

There are primarily two modes of ablation in nanosecond PLA, which are normal vaporization and phase explosion. Normal vaporization can take place at any level of energy fluence. When ablation

occurs due to normal vaporization, the maximum surface temperature that the graphite target can reach is primarily controlled by its boiling temperature. Phase explosion only appears at high values of the energy fluence that can bring the surface temperature of the target close to the thermodynamic critical point. Explosion of liquid phase is highly time dependent, which also requires very high heating rates. Phase explosion can be initiated as the target temperature approaches $0.9T_c$, where T_c is the thermodynamic critical temperature. As the surface (liquid) temperature approaches $0.9T_c$, large fluctuations in density start to take place resulting in the formation of vapor nuclei in the low density regions. Rate of vapor nuclei formation increases significantly at $0.9T_c$, leading to homogeneous bubble nucleation inside the liquid, which results in explosion of the liquid phase (Bulgakova and Bulgakov, 2001; Kelly and Miotello, 1996; Martynyuk, 1977). The critical temperature for graphite is estimated from an empirical relationship based on the latent heat of vaporization suggested by Martynyuk (1977) and is approximately 11670 K. It can be observed from Figure 4.18 that the calculated maximum surface temperature remains well below $0.9T_c$. In the case of PEBA, the ablation of graphite takes place predominantly by means of normal vaporization with no evidence of phase explosion taking place even at an efficiency factor as high as 0.8. This is likely the result of the lack volumetric boiling, which is initiated by the heterogeneous nucleation. As a result, the vapor nuclei do not have adequate time to expand to a critical size. Furthermore, experimental studies reported on ablation of graphite irradiated by electron beam operating at an accelerating voltage ~14.5 kV and pulse duration of ~100 ns revealed that there was no evidence of large size clusters or fragments seen during nano-crystalline diamond thin film grown by PEBA (Alshekhli and Henda, 2014). Accordingly, target surface temperature results obtained by model and experimental studies suggests that phase

explosion could not take place during deposition of thin films via PEBA. Ablation can be considered to take place primarily in the regime of normal vaporization from the target surface.

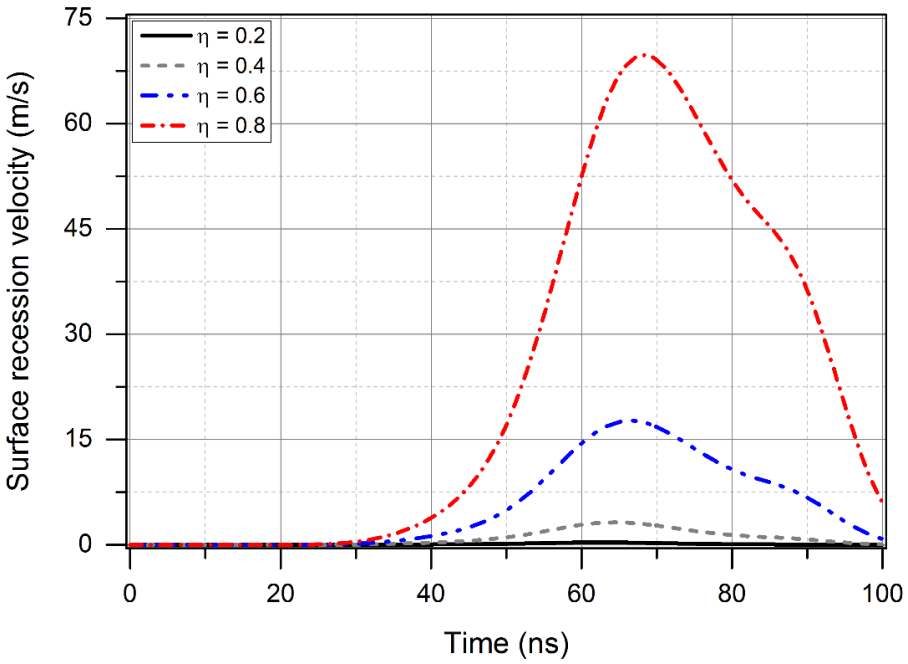

Figure 4.19: Surface recession velocity for various beam efficiencies as a function of time during pulse duration as is the case for melting.

Recession velocity from the target surface for different values of η by considering a back flux coefficient of 0.18 is presented in Figure 4.19. It can be observed that the surface recession velocity profile visibly reflects the Gaussian electron beam intensity distribution at the target. At higher values of η, i.e., 0.6 and 0.8, the surface recession velocity increases with time due to steady energy accumulation during the period of pulse duration. As depicted in Figure 4.19, the calculated surface recession velocity for $\eta = 0.8$ attains a maximum value of 70 m/s at about 68 ns, i.e., when the target surface is at maximum temperature (8500 K). Beyond the latter, it can be observed that the surface recession velocity decreases as the surface temperature of the target drops. This suggests that vaporization also comes to an end once the pulse is terminated (~100 ns). For low efficiencies, the surface recession velocity is not high enough to cause a significant amount of vaporization of

the target surface due to lower saturated vapor pressure available just above the surface. For all values of efficiency, it can be seen that upto 30 ns there is no substantial vaporization of the target. This delay in surface vaporization in the case of PEBA (comparatively to PLA) is primarily the result of the fact that the pulse width (~100 ns) of the current electron beam is nearly five time longer than that of a pulsed excimer laser, which leads to an increase in the thermal diffusion depth of the electrons. Accordingly, greater thermal diffusion depth and longer pulse width give rise to an increase in the effective depth of energy deposition and lengthening of the onset time for ablation and plasma expansion during PEBA (Gilgenbach et al, 1999). As can be observed in Figure 4.19, around 85 ns, the surface recession velocity exhibits a hump. The latter corresponds to an inflection point in the profile of the beam power density (not shown here).

The melting depth of the target during electron beam irradiation can be obtained by integrating the time evolution of the melt front velocity, given by equation (23). Melt depth calculated for various values of η for the entire pulse width is shown in Figure 4.20. As anticipated for the case of 0.8, the estimated melt depth, namely, 10 μm, is greater than other values of efficiency factor. For high efficiencies, i.e., 0.6 and 0.8, the graphite surface approaches the melting point in a shorter duration as a result of a stronger heat flux at the target surface. However, for all values of the efficiency, the target surface approaches the melting point within 25 ns from the beginning of the pulse. At this point in time, the melt layer develops at the surface and, afterwards, extends from the surface into the target. The melt depth reaches a maximum value at the end of the pulse width. While the surface temperature starts to decrease after pulse termination (Figure 4.18), the target surface can still stay in molten state for a considerably long period of time even after the pulse ends. As expected, similar trends can be observed for the other values of the beam efficiency.

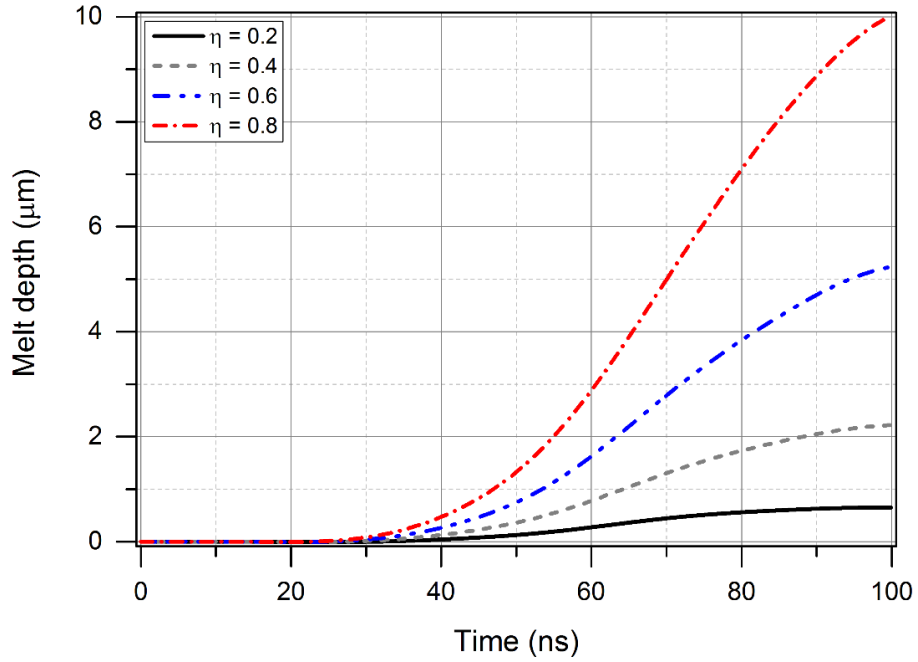

Figure 4.20: Melt depth for various beam efficiencies as a function of time during pulse duration as is the case for melting.

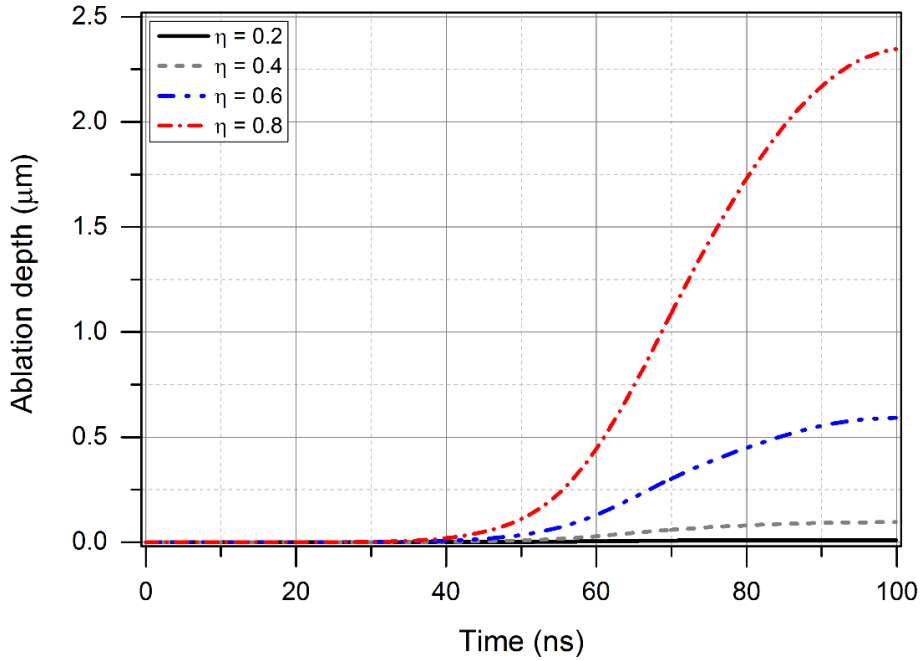

Figure 4.21: Ablation depth for various beam efficiencies as a function of time during pulse duration as is the case for melting.

From the surface recession velocity and pulse duration, the ablation depth and ablated mass per unit area are estimated and they are plotted as a function of pulsed duration in Figures 4.21 and 4.22, respectively. Ablation depth and ablated mass increase continuously as a function of pulse duration and reach maximum values of about 2.3 μm and 4 μg/mm^2, respectively, before the termination of the pulse. Ablation is initiated after 30 ns, which can be considered as the ablation threshold time. It can be seen that the time of ablation threshold varies for different values of beam efficiency. An increase in η leads to a decrease in ablation threshold time and an increase in ablation depth and ablated mass per unit area. At low efficiencies, i.e., 0.2 and 0.4, it can be observed that the vapor motion from the irradiated spot on the target is very weak, melted material remains in its original position, and the melted layer is still very thick. This poor ablation performance is mainly due to the fact that a large fraction of the beam energy is backscattered from the surface and the remaining beam energy is consumed to cause surface heating and melting. Ablation appears to be more efficient in the case of high η (0.6 and 0.8) mainly due to the fact that a large fraction of beam electrons is used. It can be also observed that a very less amount of melt layer is ablated, which is very likely the result of high energy losses beneath the surface than energy gain at the surface. Scanning electron microscopy analyses of target surface after electron beam irradiation did not reveal any presence of craters and liquid droplets on the target surface (Tricot et al., 2010). Furthermore, fast imaging analyses of the expanding plasma plume from the target shows no traces of any bright trails affiliated with the explosion of liquid droplets from the surface (Tricot et al., 2008). Both analyses indicate that splashing of molten material from bottom of the ablation spot due to the recoil pressure of the vaporizing material is very unlikely to take place in the case of nanosecond electron beam ablation. Accordingly, ablation during PEBA occurs only as a result of normal vaporization. Beam efficiency can be considered as one of the key factors

that governs the ablation process during pulsed electron beam deposition. Calculated ablation depth and ablated mass seem to be marginally overestimated for an efficiency of 0.8 or highly underestimated for lower values of η, i.e., 0.2 and 0.4. For an efficiency of 0.6, ablation appears to agree with a lower limit of reported experimental data as discussed later.

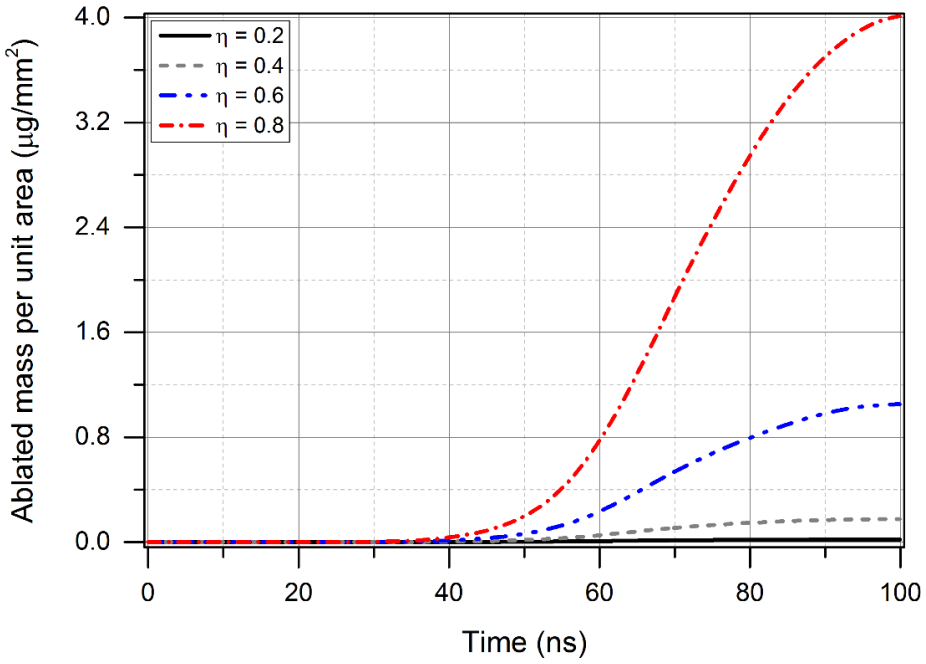

Figure 4.22: Ablated mass per unit area for various beam efficiencies as a function of time during pulse duration as is the case for melting.

4.5.2 Beam Power Density

An effective method to improve the heating rate in PEBA is by providing a large beam power density onto the target surface through the reduction of the beam spot cross-sectional area. In order to improve the beam power density, the target surface must be as close as practically possible to the electron beam tube output. Accordingly, the effect of beam power density on ablation can be assessed by modifying the beam spot radius (r) in equations 34 and 35. Various values of the beam

spot radius used in this study are 2.0, 2.6, 2.9 and 3.5 mm. Based on geometrical considerations, the values of beam spot radius (r), viz., 2.0 mm, 2.6 mm, 2.9 mm, and 3.5 mm correspond to values of the distance between the beam tube output and target surface (d) of 4.0 mm, 6.0 mm, 8.0 mm, and 10.0 mm, respectively. Figures 4.23, 4.24, 4.25 and 4.26 show the calculated surface temperature, surface recession velocity, ablation depth and ablated mass per unit area for various values of the distance between the tube output and target surface for the entire pulse width at an efficiency of 0.6. For a distance of 4 mm, it can be seen from Figure 4.23 that the heating rate and surface temperature increase very quickly and the surface reaches a maximum temperature of 7500 K. It can be observed from Figure 4.24 that target surface recession is substantial at this temperature. Similarly, as shown in Figures 4.25 and 4.26, ablation depth and mass per unit area are significant at this temperature relatively to other long distances. This is due to the fact that beam electrons are less prone to deviation and their energy is restricted to a smaller surface area. As a result, the beam power density increases with decreasing tube output-target surface distance, which, in turn, enhances the heating rate and ablation efficiency. At long distances, it can be seen that the heating rate and surface temperature rise very slowly. For instance at distance of 6 mm, the target surface just reaches a temperature of 5400 K. Similar profiles of surface recession velocity, ablation depth and ablated mass per unit area for a distance of 6 mm can be observed. As the tube output-target distance increases, the beam electrons deviate from their path and the beam cross-sectional area increases while, at the same, the beam power density on the target surface decreases.

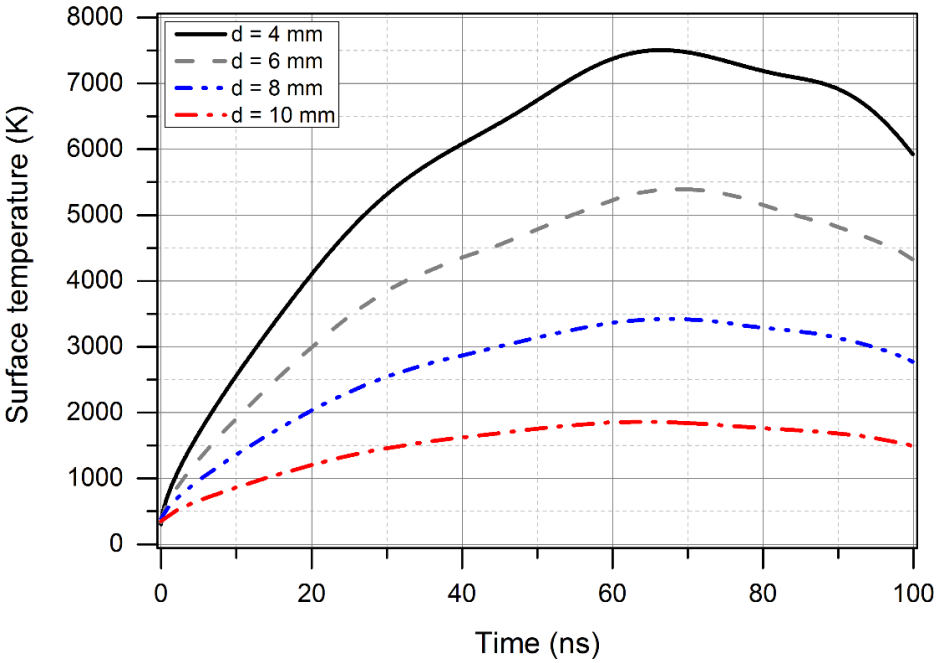

Figure 4.23: Target surface temperature for various distances between beam tube output and target surface as a function of pulse duration for an efficiency of 0.6 as is the case for melting**.**

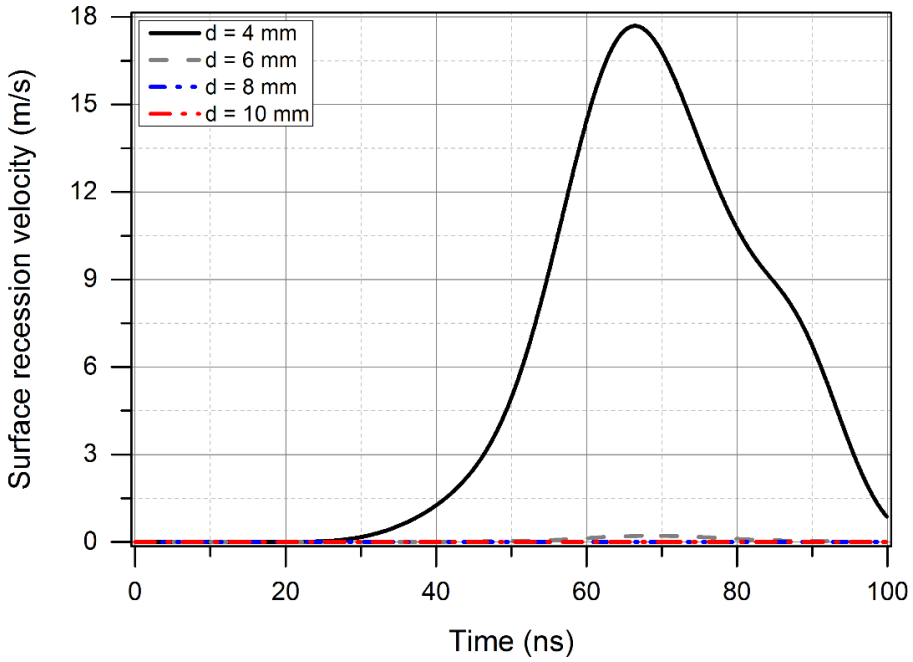

Figure 4.24: Surface recession velocity for various distances between beam tube output and target surface as a function of pulse duration for an efficiency of 0.6 as is the case for melting.

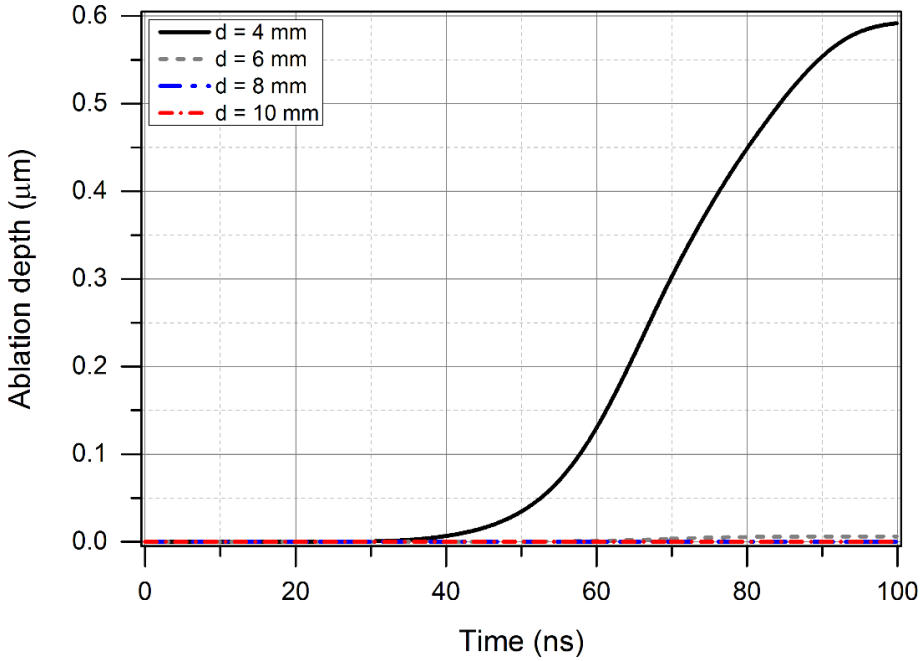

Figure 4.25: Ablation depth for various distances between beam tube output and target surface as a function of pulse duration for an efficiency of 0.6 as is the case for melting.

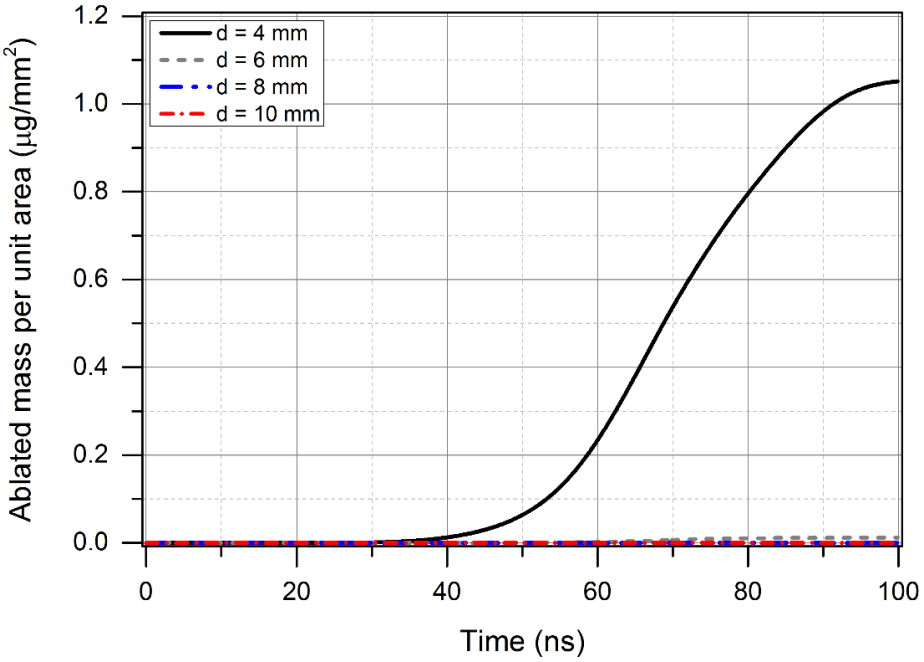

Figure 4.26: Ablated mass per unit area for various distances between beam tube output and target surface as a function of pulse duration for an efficiency of 0.6 as is the case for melting.

4.5.3 Accelerating Voltage

In this section, the target surface temperature is calculated and discussed in terms of the effect of beam accelerating voltage. The temperature distribution at the target surface for various values of accelerating voltage is presented in Figure 4.27 for an entire pulse width of 100 ns at a beam efficiency of 0.6. The maximum temperature is to be found at the target surface, as anticipated. For the accelerating voltage in the range of 10 to 15 kV, it can be observed that the heating rate and surface temperature increases very quickly. These results are most likely due to the polyenergetic character of the electron beam as explained earlier (Kowalewicz and Redel, 1995). A large fraction of electrons generated by the beam for the voltage in the range of 10 to 15 kV have lower energies. Accordingly, the bulk of beam energy is deposited near the target surface. The maximum temperature is about 7500 K for an accelerating voltage of 15 kV at around 67 ns.

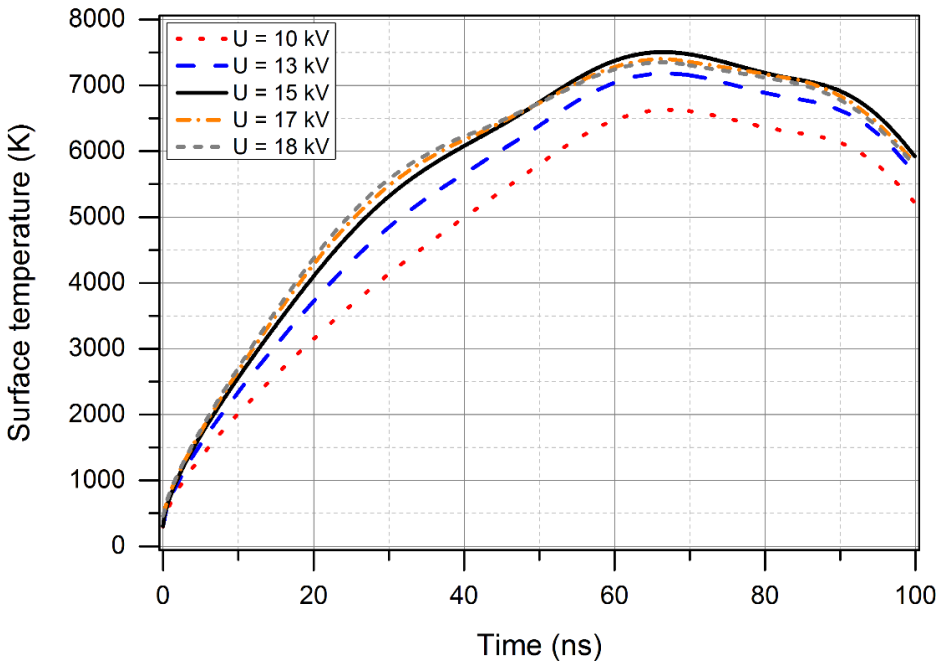

Figure 4.27: Target surface temperature for various accelerating voltages as a function of pulse duration for an efficiency of 0.6 as is the case for melting.

After the surface has reached the maximum temperature, it stays at this temperature for few nanoseconds due to thermal inertia, which leads to an increase in vaporization. An increase in accelerating voltage beyond 15 kV does not lead to a substantial rise in the heating rate as a result of the increase in the penetration depth of the electrons, which tends to offset beam intensity. An increase in the accelerating voltage leads to an increase in the electrons energy in the beam while, at the same time, electrons consisting of high energy will penetrate deeper in the target. This leads to high losses of the beam energy, which turns out to be more significant at higher voltages (above 15 kV), and, in the end, cancels out the effect of the acceleration voltage on the beam energy. For 17 and 18 kV, it can be seen that initially the heating rate is marginally greater than for 15 kV, but it tends to decrease slightly after 50 ns yielding a maximum temperature of 7400 and 7350 K, respectively. The evolution of the target surface temperature with time and dependence on voltage seem to have a similar trend for all high voltages.

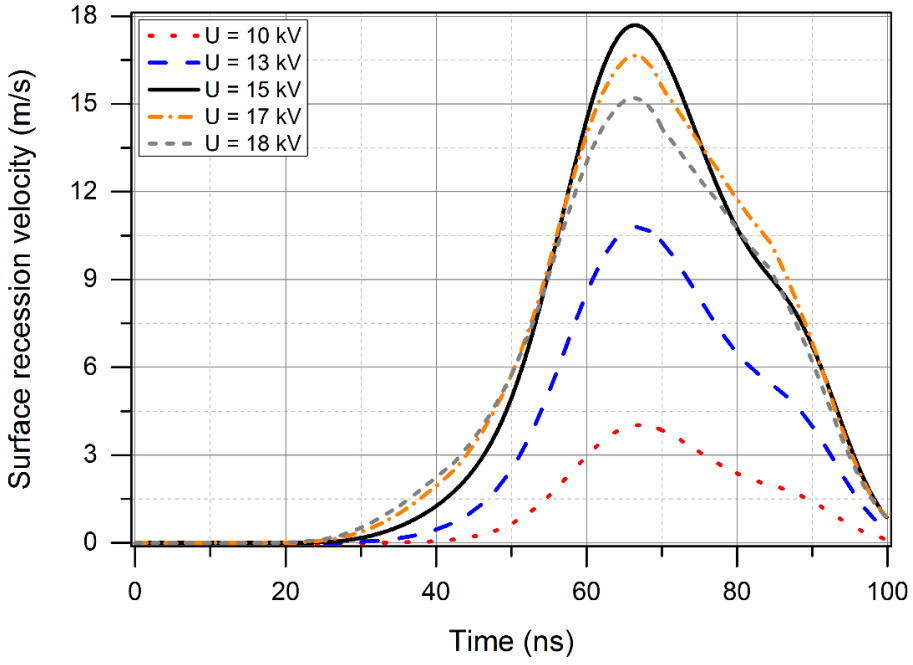

Figure 4.28: Surface recession velocity for various accelerating voltages as a function of pulse duration for an efficiency of 0.6 as is the case for melting.

The amount of material vaporized from the target surface for various values of accelerating voltage is depicted in Figure 4.28. As it can be observed, at 15 kV the velocity approaches a maximum value of about 18 m/s at 67 ns, i.e., when the temperature of the target surface reaches its maximum (7500 K). Away from the latter, the surface recession velocity falls as the temperature at target surface decreases. Similar profiles can be seen for the other values of the accelerating voltage.

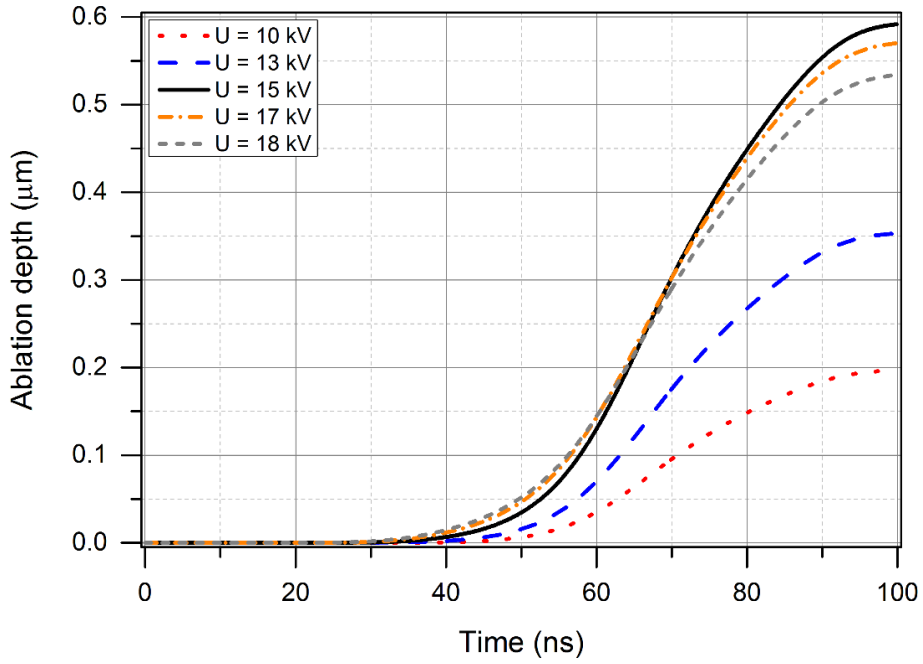

Figure 4.29: Ablation depth for various accelerating voltages as a function of pulse duration for an efficiency of 0.6 as is the case for melting.

The calculated ablation depth and ablated mass profiles from target surface for different values of the accelerating voltage are shown for the entire pulse width in Figures 4.29 and 4.30. For the case of $\eta = 0.6$, the calculated ablation depth and ablated mass per unit area are higher than for other values of the accelerating voltages, as anticipated. The calculated values of ablation depth and ablated mass per unit are around 0.6 μm and 1.05 μg/mm^2, respectively. Similar trends of both ablation depth and ablated mass per unit area for the remaining accelerating voltages can be observed.

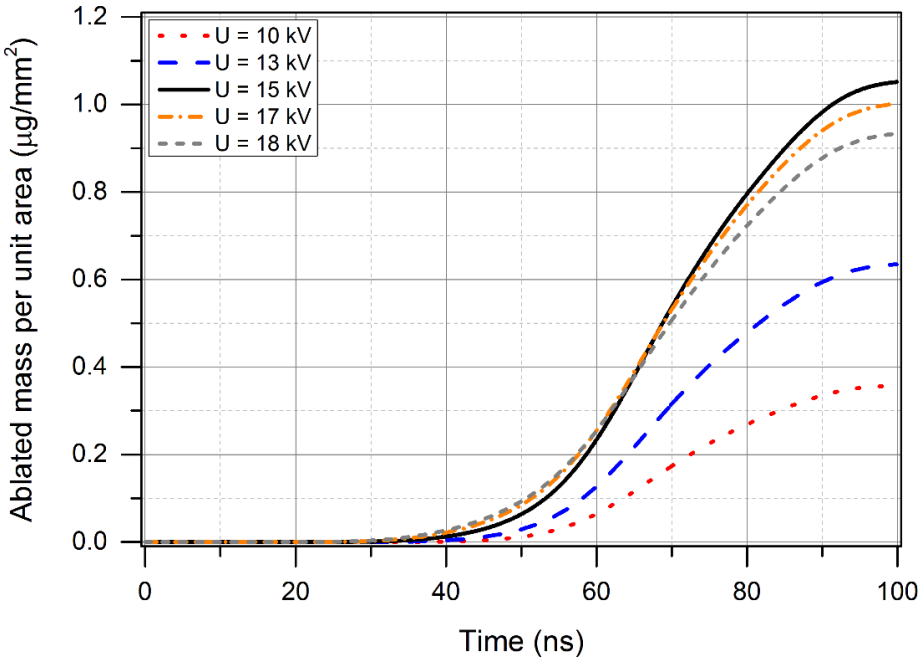

Figure 4.30: Ablated mass per unit area for various accelerating voltages as a function of pulse duration for an efficiency of 0.6 as is the case for melting.

4.5.4 Model Assessment

To assess the model (melting in this case), the calculated parameters for a beam efficiency value of 0.6 and accelerating voltage of 15 kV are compared to appropriate experimental data available in the literature and results obtained from model based on sublimation (Ali and Henda, 2015; Bulgakova and Bulgakov, 2001; Harshavardhan and Strikovski, 2005; Höbel et al., 1990; Kowalewicz and Redel, 1995; Strikovski and Harshavardhan, 2003; Strikovski et al., 2010). For a beam efficiency of 0.6, the ablated mass per unit area (mm^2) in case of melting is about ~14 µg/pulse or ~7×10^{17} atoms/pulse, which is in good agreement with appropriate experimental data of a few tens of µg/pulse (Harshavardhan and Strikovski, 2005) or some 10^{17} atoms/pulse (Kowalewicz and Redel, 1995). The ablated mass per unit area reported by the experimental results in PEBA is almost 10 times higher than its counterpart in PLA. This is precisely in our case where the ablation mass in PEBA is 5-10 times the rate in PLA for a graphite target (Bulgakova and

Bulgakov, 2001; Harshavardhan and Strikovski, 2005). The ablated mass per unit area obtained by model based on sublimation phenomena is relatively 3.5 times greater than melting model. As far as heating rate is concerned, our calculated results are in qualitative (no absolute values have been provided by the authors) accordance with available experimental data (Strikovski and Harshavardhan, 2003; Strikovski et al., 2010). The latter point out that the heating rate is at maximum at a voltage of about 15 kV. The heating rate in both case of melting and sublimation is maximum at a voltage of about 15 kV. Finally, it have been reported that if the beam intensity is sufficient then a certain layer (~1 μm) within all kind of target material can be ablated (Harshavardhan and Strikovski, 2005; Höbel et al., 1990). This is in reasonable agreement with our calculated ablated depth of ~ 0.6 μm as depicted in Figure 4.21. For the sake of comparison between melting and sublimation, ablated depths calculated from the model accounting for sublimation is about 3.5 times higher than the model accounting for melting. Comparing the results obtained from the current model and the results obtained from the sublimation based model, it can be concluded that the melting model seems to be more realistic. Based on the aforementioned observations and in accordance with some earlier experimental data (Höbel et al., 1990; Müller and Schultheiss, 1994), melting seems to be the phenomenon likely responsible for the removal of material from the target surface during PEBA. Accordingly, the ablation of graphite in the case of PEBA can be considered to take place predominantly in the regime of heating, melting and vaporization from the target surface.

Chapter 5

5 Plume Dynamics Results and Discussion

5.1 Introduction

Material ablation, plasma expansion, and the interaction of plume particles with an ambient gas are critical in defining the morphology and structure of thin films. The properties of the expanding plume play a crucial role in defining the ultimate properties of the deposited films (Misra et al., 1999). The distribution and range of the kinetic energy of the ablated plume particles significantly affect the quality of the deposited film. The presence of an ambient gas influences both the energy and nature of ablated particles impinging on the substrate surface, which, in turn, govern the properties of the deposited films (Thareja et al., 1997). Despite PEBA increasing technological significance, details of the complex processes responsible for its characteristic features are not well explored. The processes controlling PEBA are strongly coupled and nonlinear. For a better understanding of phenomena affecting the quality of thin film growth, it is expedient to develop a comprehensive model of the process. Accordingly, modeling of the plasma plume expansion into an ambient gas is important not only to acquire a better understanding of the phenomena involved, but also to optimize and eventually control PEBA process. In this chapter, results of plasma expansion induced upon irradiation with a nanosecond (~100 ns) polyenergetic pulsed electron beam (for a beam efficiency of 0.6 and accelerating voltage of 15 kV) from a graphite target placed in an argon atmosphere at reduced pressure are presented. Simulation results obtained by the set of one-dimensional gas-dynamics equations are validated by comparing with experimental data available in the literature.

5.2 Plasma plume expansion in the presence of a background gas

The spatio-temporal evolutions of the temperature, velocity, pressure, and electron density of expanding plasma induced during PEBA of graphite are calculated by solving the gas dynamics equations, viz., equations (39) – (65), and discussed in the following sections. Results from our recent investigations have indicated that the optimum values of beam efficiency and accelerating voltage are about 0.6 and 15 kV, respectively, for the target to reach optimal ablation performance, see Chapter 4 (sections 4.4 and 4.5) and (Ali and Henda, 2015; Ali and Henda, 2017). The results correspond to a beam efficiency of 0.6 and accelerating voltage of 15 kV.

5.2.1 Temperature Distribution

The plasma plume temperature is illustrated in Figure 5.1. A rich variety of shock waves can be clearly observed from the form of the temperature profiles at different times during the beam pulse. As can be observed in Figure 5.1, the plasma temperature increases rapidly in the vicinity of the target surface. At 20 ns, corresponding to the onset of ablation, the plasma temperature can reach a maximum value of 11,800 K at ~0.5 cm above the target surface. Between one-third and two-thirds of the beam pulse, i.e., ~30 ns to ~60 ns, inner and outer shock waves can be clearly observed, see Figure 5.1, t = 40 ns, 60 ns. 'Doubling' of the shock wave is likely the result of the expanding plasma being pushed backward by the ambient gas. The plasma temperature seems to decrease, albeit only slightly, e.g., ~11,400 K at 40 ns and ~11,300 K at 60 ns (see Figure 5.1), relatively to the plasma temperature during the early stage of the beam pulse. This is the result of energy losses owing to internal interactions within the expanding plasma and plasma interaction with the ambient gas. Towards the end of the pulse, the shock waves seem to blend together resulting in a broader shock wave, as depicted in Figure 5.1 at t = 80 ns and 100 ns. The plasma

temperature slightly increases due to the polyenergetic nature of the electron beam, viz, highly and weakly energetic electrons appear at the start and end of the beam pulse, respectively. (Ali and Henda, 2017; Witke et al., 1996).

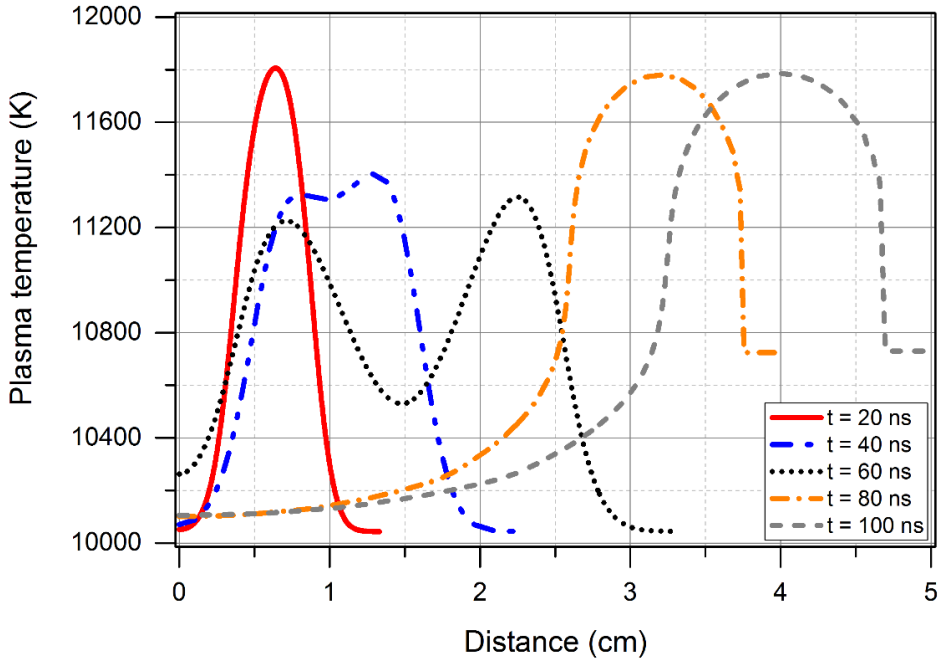

Figure 5.1: Spatial distribution of plasma temperature at various time intervals.

5.2.2 Plasma Velocity

Plasma velocity profile calculated for various time intervals is shown in Figure 5.2. As the plume expands, the plasma velocity increases significantly over the pulse duration. For example, at 20 ns corresponding to the onset of ablation, the plasma velocity is just below 5000 m/s. For larger values of time, the plume velocity further increases as the plume expands in the upward direction and reaches a maximum value of ~9900 m/s at the shock wave peak at the end of the beam pulse, see Figure 5.2, t = 100 ns. As anticipated, the presence of the low pressure ambient gas slightly affects the plume velocity and, in turn, allows the plume to expand over a large distance.

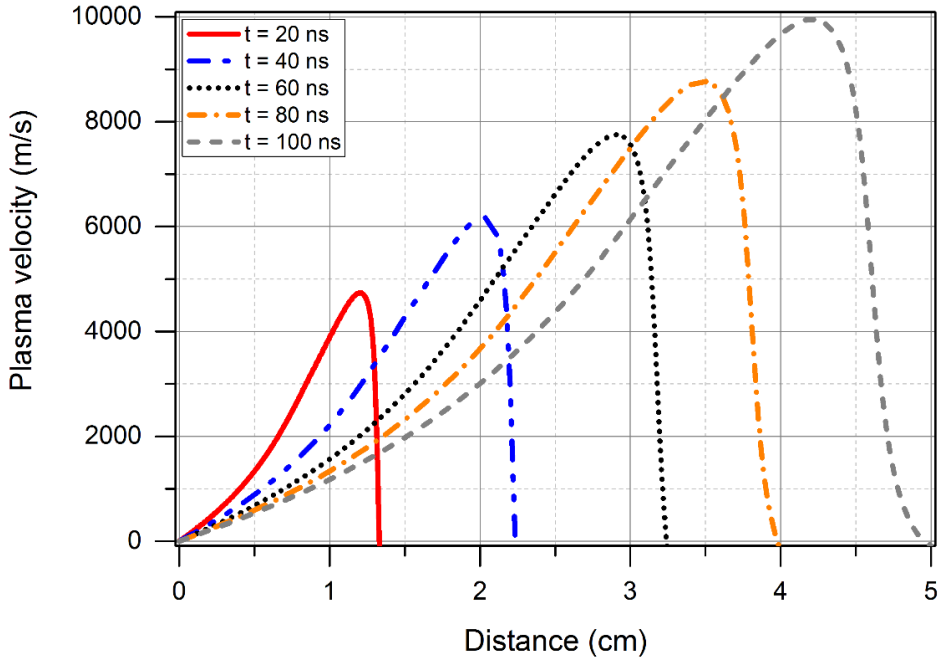

Figure 5.2: Spatial distribution of plasma velocity at various time intervals.

5.2.3 Plasma Pressure

The spatial distribution of the plume pressure as a function of time is presented in Figure 5.3. It can be observed that, at first, the expanding plasma encounters an isentropic rarefaction wave, where the pressure decreases as the plasma plume moves forward. As anticipated, the maximum pressure is located near the target surface. For instance, at 20 ns, the maximum value of the plasma pressure is ~2.7×10^6 Pa, which decreases as the plasma plume moves away from the surface. As time progresses, the pressure of expanding plasma declines. At the end of beam pulse (100 ns), the plume pressure reaches a maximum of 4×10^5 Pa only in the vicinity of the target surface (about eightfold less than at 20 ns).

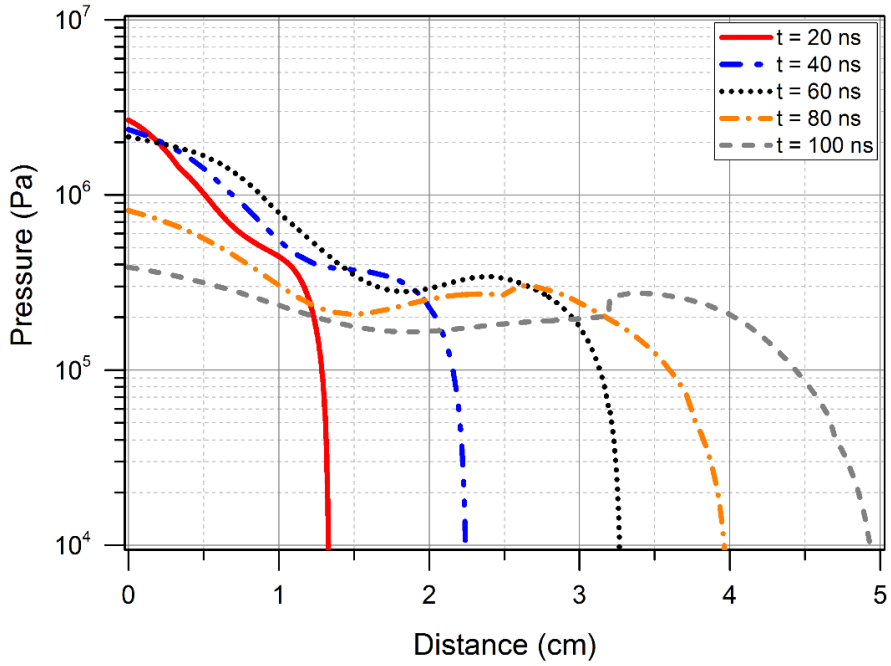

Figure 5.3: Spatial distribution of plasma pressure at various time intervals.

5.2.4 Electron Density

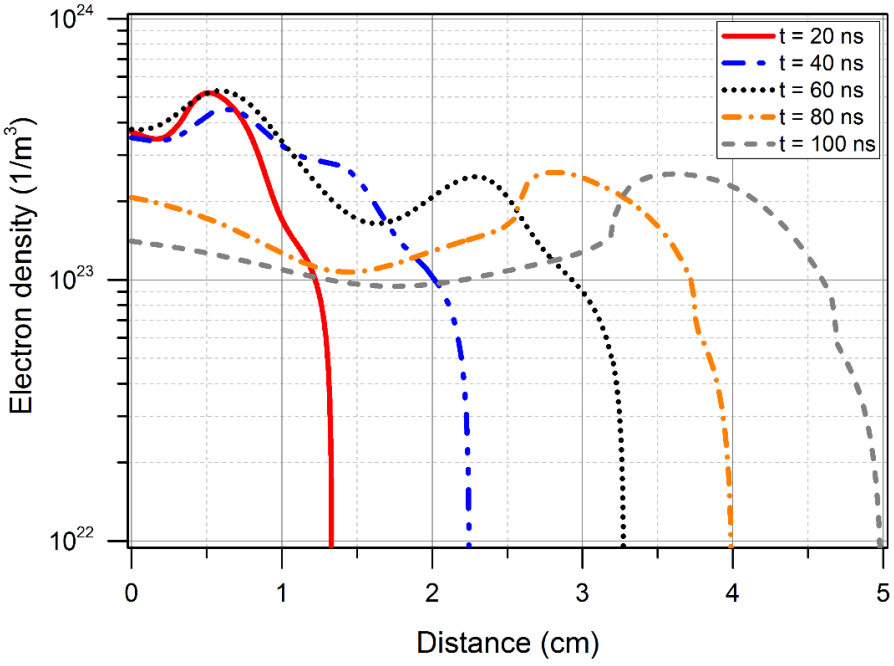

Figure 5.4: Spatial distribution of plasma electron density at various time intervals.

Figure 5.4 shows the spatial distribution of the electron density of the plasma at various time intervals throughout the beam pulse. It can be observed that the electron density exhibits a maximum value, which is shifted away from the target surface as time increases. At 20 ns, the maximum value of electron density is ~5.2×10^{23} m^{-3}, which is located at ~ 0.5 cm from the target surface. For longer times, such as at 80 ns, the maximum electron density is 2.5×10^{23} m^{-3} and located ~2.8 cm from the target surface. Overall, the electron density and plasma pressure profiles seem to show similar structures.

5.3 Model Assessment

In order to assess the model, some of the calculated variables from the current model have been compared with experimental data available in the literature for plasma induced during PEBA (Witke et al., 1996; Tricot et al., 2008; Nistor et al., 2010). Experimental results have reported electron density values in the range of 10^{16}-10^{17} cm^{-3} (Witke et al., 1996; Tricot et al., 2008; Nistor et al., 2010). This is in accordance with our calculation results, whereby the average electron density is ~10^{17} cm^{-3}. It has been found that the average temperature of the plasma varies from 1 eV to 1.25 eV (Witke et al., 1996; Tricot et al., 2008). The results based on our calculations indicate that the plasma temperature is ~1 eV, which is in quantitative agreement with the reported experimental data. Finally, experimental investigations have revealed that the propagation of the plasma plume can reach ~10^4 m/s (Nistor et al., 2010). This is in good agreement with our calculated plasma velocity of 9900 m/s as depicted in Figure 5.2.

Chapter 6

6 Conclusion and Prospective Work

6.1 Conclusion

To our knowledge, this is the first attempt to comprehensively model the fundamental processes responsible for the growth of thin films during pulsed electron beam ablation. The major findings and conclusions of this thesis work are summarized in the following sections.

1. Electron Beam Ablation

A comprehensive model to study electron beam ablation has been presented by solving a one-dimensional two-stage heat conduction equation to account for the interaction of an electron pulse of 100 ns with a graphite target. The electron beam-target interaction was modeled using a classical thermal approach. The thermal model proposed in this study comprises of two different approaches during beam-target interaction, which were as follows: (a) Heating and sublimation, and (b) Heat, melting and vaporization.

A. Heat and Sublimation

The temporal and spatial dependence of the temperature of the target has been numerically estimated. Surface recession velocity, ablation depth and rate have also been calculated. A comparative study has been carried out to assess the effects of the Knudsen layer and back flux coefficient on the surface recession velocity at the target surface. The findings have shown that an optimum value of the beam energy efficiency and accelerating voltage is around 0.6 and 15 kV, respectively, when considering a back flux coefficient of 0.18, corresponding to realistic values of the surface recession velocity, ablation depth and ablated mass per unit area. It has been found that the target surface can reach a temperature of 7500 K and an ablated mass of about 3.8 $\mu g/mm^2$ at

an efficiency of 0.6. The calculated results have been compared with available experimental and theoretical data and found to be in overall good agreement. The beam tube output distance from the target surface greatly influences the ablation performance during beam-target interaction. An effective method to optimize the heating rate in PEBA is by the provision of a large beam power density onto the target surface through the reduction of the beam spot cross-sectional area.

B. Heat, Melting and Vaporization

The thermal model proposed in this study captures a number of complex phenomena consisting of heating, melting and vaporization during beam-target interaction. Melting depth, surface recession velocity, ablation depth, and ablated mass per unit area have been calculated from the model. The calculation results show that various process parameters such as electron beam efficiency, power density and accelerating voltage significantly influence the ablation process during beam-target interaction. The results indicate that the efficiency factor and accelerating voltage have optimum values around 0.6 and 15 kV, respectively. The findings have shown that the target surface can reach a temperature of 7500 K and an ablated mass of about 1.05 $\mu g/mm^2$ at the optimum values of efficiency and accelerating voltage**.** The maximum temperature calculated for the target surface is well below the empirically estimated thermodynamic critical temperature of graphite. Accordingly, the absence of a sudden rise in the ablated mass with increasing beam efficiency, power density and accelerating voltage is indicative that material removal occurs primarily through normal vaporization instead of phase explosion. The calculated results compare favorably well with experimental data available in the literature for an accelerating voltage 15 kV and an efficiency of 0.6.

2. Plasma Plume Expansion

We have proposed a one-dimensional gas-dynamics model based on Navier-Stokes equations to investigate the properties of plasma expansion induced during PEBA. Model calculations allow the estimation of the spatio-temporal dependence of the temperature, velocity, pressure, and electron density of the expanding plasma. The calculated preliminary results for an efficiency factor and accelerating voltage of 0.6 and 15 kV, respectively, are in good agreement with experimental data reported in the literature.

6.2 Prospective Work

As in any modeling efforts, the model developed as part of this thesis project is based on a few assumptions, which have been carefully assessed and rationalized. A few recommendations for future work and/or enhancements of current model are in order.

- For comparison purposes, the electron beam-target interaction could be modeled using the Boltzmann transport equation (BTE) and contrast the results with continuum approach based on Fourier's law.
- It would be interesting to analyze the effect of different heat sources on the maximum temperature of the target surface. The different heat sources could be possibly based on empirical measurements to define the decaying energy of the electrons beneath the target surface.
- A two-dimensional gas-dynamics model based on compressible Euler equations could be employed to investigate the properties of plasma expansion induced during pulsed electron beam.

It would be interesting to have direct access to some analytical and plasma diagnostic tools to have a more comprehensive comparison between experimental and modeling results.

- More comprehensive experimental studies of electron beam ablation with the assistance of scanning electron microscopy (SEM) analyses could be carried out to have a better understanding of the interaction of the pulsed electron beam with a graphite target.
- In-situ experimental studies based on Langmuir probe and optical emission spectroscopy (OES) could be employed to characterize the electron temperature, electron density and identify plasma species. The measurement data of electron density, temperature and plasma species could be compared with the results obtained from the gas-dynamics model.

References

Abrahamson, J., 1974, “Graphite sublimation temperatures, carbon arcs and crystallite erosion”, *Carbon*, vol. 12, no. 2, pp. 111-118.

Aggoune, S., Vidal, F., and Amara, E.H., 2010, “Numerical study of the expansion of metallic vapor plasma by a nanosecond”, *Applied Physics A: Materials Science and Processing*, vol. 101, no. 1, pp. 167-171.

Aghaei, M., Mehrabian, S., and Tavassoli, S.H., 2008, “Simulation of nanosecond pulsed laser ablation of copper samples: A focus on laser induced plasma radiation”, *Journal of Applied Physics,* vol. 104, no. 5, pp. 53303-53311.

Akamatsu, H., and Yatsuzuka, M., 2003, “Simulation of surface temperature of metals irradiated by intense pulsed electron, ion and laser beams”, *Surface and Coatings Technology,* vol. 166-170, pp. 219-222.

Ali, M., and Henda R., 2015, “Mathematical modeling of pulsed electron beam induced heating and sublimation in graphite”, *ECS Journal of Solid State Science and Technology,* vol. 4, no. 9, pp. P369-P375.

Ali, M., and Henda R., 2017, “Modeling of beam-target interaction during pulsed electron beam ablation of graphite: Case of melting”, *Applied Surface Science,* vol. 396, pp. 67-77.

Alexiades, V., and Autrique D., 2010, “Enthalpy model for heating, melting, and vaporization in laser ablation”, *Electronic Journal of Differential Equations: Conference,* vol. 19, pp. 1-14.

Alloul, H., 2011, "Electron Transport in Solids" in *Introduction to the Physics of Electrons in Solids*, trans. S. Lyle, Springer-Verlag, Berlin, pp. 99-143.

Alshekhli, O., and Henda R., 2014, “Hydrogen-free deposition of nanocrystalline diamond by channel-spark electron beam ablation”, *ECS Journal of Solid State Science and Technology,* vol. 3, no. 6, pp. M21-M25.

Anisimov, S.I., 1968, “Vaporization of metal absorbing laser radiation”, *Soviet Physics Journal of Experimental and Theoretical Physics*, vol. 27, no. 1, pp. 182-183.

Anisimov, S.I., Bäuerle, D., and Luk’yanchuk, B.S., 1993, “Gas dynamics and film profiles in pulsed-laser deposition of materials”, *Physical Review B*, vol. 48, no. 16, pp. 12076-12081.

Anisimov, S.I., Luk'yanchuk, B.S., and Luches, A., 1996, "An analytical model for three-dimensional laser plume expansion into vacuum in hydrodynamics regime", *Applied Surface Science*, vol. 96-98, pp. 24-32.

Arnold, N., Gruber, J., and Heitz, J., 1999, "Spherical expansion of the vapor plume into ambient gas: an analytical model", *Applied Physics A: Materials Science and Processing*, vol. 69, no. 7, pp. 87-93.

Baeri, P., Campisano, S.U., Foti, G., and Rimini, E., 1979, "A melting model for pulsing–laser annealing of implanted semiconductors", *Journal of Applied Physics*, vol. 50, no. 2, pp. 788-797.

Baskin, Y., and Meyer, L., 1955, "Lattice constants of graphite at low temperatures", *Physical Reviews*, vol. 100, no. 2, pp. 544.

Bäuerle, D., 2011, *Laser Processing and Chemistry,* Springer-Verlag, Berlin, pp. 177-235.

Bhattacharya, D., Singh, R.K., and Holloway, P.H., 1991, "Laser-target interactions during pulsed laser deposition of superconducting thin films", *Journal of Applied Physics,* vol. 70, no. 10, pp. 5433-5439.

Bird, G.A., 1994, *Molecular Gas Dynamics and the Direct Simulation of Gas Flow,* Clarendon Press, Oxford, pp. 218.

Bird, R.B., Stewart, W.E., and Lightfoot, E.N., 2002, *Transport Phenomena,* John Wiley and Sons Inc., New York, 2nd ed.

Bishop, H.E., 1967, "Electron scattering in thick targets", *British Journal of Applied Physics,* vol. 18, no. 6, pp. 703-715.

Bulgakova, N.M., and Bulgakov, A.V., 2001, "Pulsed laser ablation of solids: transition from normal vaporization to phase explosion", *Applied Physics A: Materials Science and Processing*, vol. 73, no. 3, pp. 199-208.

Bulgakova, N.M., Bulgakov, A.V., and Babich, L.P., 2004, "Energy balance of pulsed laser ablation: thermal model revised", *Applied Physics A: Materials Science and Processing*, vol. 79, no. 4-6, pp. 1323-1326.

Bulgakov, A.V., and Bulgakova, M.N., 1995, "Dynamics of laser-induced plume expansion into an ambient gas during film deposition", *Journal of Physics D: Applied Physics*, vol. 28, no. 8, pp. 1710-1718.

Carslaw, H., and Jaeger J., 1986, *Conduction of Heat in Solids*, Oxford University Press Inc., New York, 2nd ed.

Chen, G., 2001, "Ballistic-diffusive heat-conduction equations", *Physical Review Letters*, vol. 86, no. 11, pp. 2297-2300.

Chen, L.M., Xu, B., Chen, P., Chen, Z.P., and Zhang, R., 2005, "Controllable formation of particulates and the effects on superconductivity of $La_{1.85}Sr_{0.15}CuO_4$ film gown by the pulsed electron deposition method", *Journal of Superconductivity and Novel Magnetism*, vol. 25, no. 4, pp. 951-956.

Chen, Z., and Bogaerts, A., 2005, "Laser ablation of Cu and plume expansion into 1 atm ambient gas", *Journal of Applied Physics*, vol. 97, no. 6, pp. 063305.

Chung, D.D.L., 2002, "Review graphite", *Journal of Materials Science,* vol. 37, no. 8, pp. 1475-1489.

Colligon, J.S., 1995, "Energetic condensation: processes, properties, and products", *Journal of Vacuum Science and Technology A,* vol. 13, no. 3, pp. 1649-1657.

Dabby, F., and Paek, U.-C., 1972, "High-intensity laser-induced vaporization and explosion of solid material", *IEEE Journal of Quantum Electronics,* vol. 8, no. 2, pp. 106-111.

Darlington, E.H., and Cosslett, V.E., 1972, "Backscattering of 0.5-10 keV electrons from solid targets", *Journal of Physics D: Applied Physics*, vol. 5, no. 11, pp. 1969-1981.

Dediu, V.I., Jiang, Q.D., Matacotta. F.C., Scardi, P., Lazzarino, M., Nieva, G., and Civale, L., 1995, "Deposition of $MBa_2Cu_3O_{7-x}$ thin films by channel-spark method", *Superconductor Science and Technology*, vol. 8, no. 3, pp. 160-164.

El-Gomati, M.M., and Assa'd, A.M.D., 1998, "On the Measurement of the Backscattering Coefficient for Low Energy Electrons" in *Modern Developments and Applications in Microbeam Analysis,* eds. G. Love, W.A.P. Nicholson, and A. Armigliato, Springer-Verlag, Wien, pp. 325-331.

Fang, R., Zhang, D., Li, Z., Yang, F., Li, L., Tan, X., and Sun, M., 2008, "Improved thermal model and its application in UV high-power pulsed laser ablation of metal target", *Solid State Communications*, vol. 145, no. 11-12, pp. 556-560.

Garrelie, F., Aubreton, J., and Catherinot, A., 1998, "Monte Carlo simulation of the laser-induced plasma plume expansion under vacuum: Comparison with experiments", *Journal of Applied Physics*, vol. 83, no. 10, pp. 5075-5082.

Garrelie, F., and Catherinot, A., 1999, “Monte Carlo simulation of the laser-induced plasma-plume expansion under vacuum and with a background gas”, *Applied Surface Science*, vol. 138-139, pp. 97-101.

Garrelie, F., Champeaux, C., and Catherinot, A., 1999, “Study by a Monte Carlo simulation of the influence of a background gas on the expansion dynamics of a laser-induced plasma plume”, *Applied Physics A: Materials Science and Processing*, vol. 69, no. 1, pp. 45-50.

Gilgenbach, R.M., Kovaleski, S.D., Lash, J.S., Ang, L.-K., and Lau, Y.Y., 1999, “Science and applications of energy beam ablation”, *IEEE Transactions on Plasma Science*, vol. 27, no. 1, pp. 150-158.

Gusarov, A.V., and Smurov, I., 2005, “Thermal model of nanosecond pulsed laser ablation: Analysis of energy and mass transfer”, *Journal of Applied Physics*, vol. 97, no. 1, pp. 014307.

Harry, J.E., 2010, *Introduction to Plasma Technology: Science, Engineering and Applications*, Wiley–VCH, Weinheim, pp. 1–13.

Harshavardhan, K.S., and Strikovski, M., 2005, "Pulsed Electron–Beam Deposition of High Temperature Superconducting Films for Coated Conductor Applications" in *Second Generation HTS Conductors*, ed. A. Goyal, Kluwer Academic Publishers, Boston, pp. 109-133.

Ho, J.R., Grigoropoulos, C.P., and Humphrey, J.A.C., 1995, “Computational study of heat transfer and gas dynamics in the pulsed laser evaporation of metals”, *Journal of Applied Physics*, vol. 78, no. 7, pp. 4696-4709.

Höbel, M., Geerk, J., Linker, G., and Schultheiss, C., 1990, “Deposition of superconducting YBaCuO thin films by pseudospark ablation”, *Applied Physics Letters*, vol. 56, no. 10, pp. 973-975.

Itina, T.E., Marine, W., and Autric, M., 1998, “Monte Carlo simulation of pulsed laser ablation into an ambient gas”, *Computational Materials Science*, vol. 10, no. 1-4, pp. 144-147.

Itina, T.E., Hermann, J., Delaporte, P., and Sentis, M., 2002, “Laser-generated plasma plume expansion: Combined continuous-microscopic modeling”, *Physical Review E,* vol. 66, no. 6, pp. 066406.

Itina, T.E., Hermann, J., Delaporte, P., and Sentis, M., 2003, “Combined continuous-microscopic modeling of laser plume expansion”, *Applied Surface Science*, vol. 208–209, pp. 27-32.

Jackson, K.A., 2002, "The interface kinetics of crystal growth processes", *Interface Science,* vol. 10, no. 2-3, pp. 159-169.

Jiang, Q.D., Matacotta, F.C., Konijnenberg, M.C., Müller, G., and Schultheiss, C., 1994, "Deposition of $YBa_2Cu_3O_{7-x}$ thin films by channel-spark pulsed electron beam ablation", *Thin Solid Films,* vol. 241, no. 1-2, pp. 100-102.

Joy, D.C., and Luo, S., 1989, "An empirical stopping power relationship for low-energy electrons", *Scanning*, vol. 11, no. 4, pp. 176-180.

Kanter, H., 1961, "Energy dissipation and secondary electron emission in solids", *Physical Review*, vol. 121, no. 3, pp. 677-681.

Kelly, B.T., 1981, *Physics of Graphite,* Applied Science Publishers, London.

Kelly, R., and Miotello, A., 1996, "Comments on explosive mechanisms of laser sputtering", *Applied Surface Science*, vol. 969-98, pp. 205-215.

Kim, W.S., Hector Jr., L.G., and Özisik, M.N., 1990, "Hyperbolic heat conduction due to axisymmmetirc continuous or pulsed heat sources", *Journal of Applied Physics*, vol. 68, no. 1, pp. 5478-5485.

Knight, C.J., 1979, "Theoretical modeling of rapid surface vaporization with back pressure", *AIAA Journal*, vol. 17, pp. 519-523.

Koleva, E., 2005, "Electron beam weld parameters and thermal efficiency improvement", *Vacuum*, vol. 77, no.4, pp. 413-421.

Kovaleski, S.D., Gilgenbach, R.M., Ang, L.K., Lau, Y.Y., and Lash, J.S., 1998, "Electron beam ablation versus laser ablation: plasma plume diagnostic studies", *Applied Surface Science*, vol. 127-129, pp. 947-952.

Kowalewicz, R., and Redel, T., 1995, "Interaction of a high current polyenergetic electron beam with metal", *IEEE Transactions on Plasma Science*, vol. 25, no. 3, pp. 270-274.

Langmuir, I., 1929, "The interaction of electron and positive ion space charges in cathode sheaths", *Physical Review*, vol. 33, no. 6, pp. 954–989.

Le, H.C., Zeitoun, D.E, Parisse, J.D., Sentis, M., and Marine, W., 2000, "Modeling of gas dynamics for a laser-generated plasma: Propagation into low-pressure gases", *Physical Review E*, vol. 62, no. 3, pp. 4152–4161.

Leider, H.R., Krikorian, O.H., and Young, D.A., 1973, "Thermodynamic properties of carbon up to the critical point", *Carbon,* vol. 11, no. 5, pp. 555-563.

Lutcov, V.I., Volga, V.I., and Dymov, B.K., 1970, "Thermal conductivity, electric resistivity and specific heat of dense graphites", *Carbon,* vol. 8, no. 6, pp. 753-760.

Mahmood, S., Rawat, R.S., Zakaullah, M., Lin, J.J., Springham, S.V., Tan, T.L., and Lee, P., 2009, "Investigation of plume expansion dynamics and estimation of ablation parameters of laser ablated Fe plasma", *Journal of Physics D: Applied Physics*, vol. 42, no. 13, pp. 135504.

Mantell, C.L., 1968, *Carbon and Graphite Handbook*, Interscience Publishers, New York, pp. 6.

Markov, A.B., and Rotshtein, V.P., 1997, "Calculation and experimental determination of dimensions of hardening and tempering zones in quenched U7A steel irradiated with a pulsed electron beam", *Nuclear Instruments and Methods in Physics Research Section B: Beam Interactions with Materials and Atoms,* vol. 132, no. 1, pp. 79-86.

Marla, D., Bhandarkar, U.V., and Joshi, S.S., 2011, "Critical assessment of the issues in the modeling of ablation and plasma expansion processes in the pulsed laser deposition of metals", *Journal of Applied Physics*, vol. 109, no. 2, pp. 021101.

Martynyuk, M.M., 1977, "Phase explosion of a metastable fluid", *Combustion, Explosion and Shock Waves*, vol. 13, no. 2, pp. 178-191.

Mathis, J.E., and Christen, H.M., 2007, "Factors that influence particle formation during pulsed electron deposition of YBCO precursors", *Physica C: Superconductivity and its Applications*, vol. 459, no. 1-2, pp. 47-51.

Mattox, D.M., and McDonald, J.E., 1963, "Interface formation during thin film deposition", *Journal of Applied Physics*, vol. 34, no. 8, pp. 2493-2496.

Mattox, D.M., 2000, "Ion plating – past, present and future", *Surface and Coatings Technology*, vol. 133-134, pp. 517-521.

McWhirter, R.W.P., 2010, "Spectral Intensities" in *Plasma Diagnostic Techniques*, eds. R.H. Huddlestone and S.L. Leonard, Academic Press, New York, pp. 201-264.

Miranda, J.O-., Yang, R., and Gil, J.J.A-., 2011, "A constitutive equation for nano-to-macro-scale heat conduction based on Boltzmann transport equation", *Journal of Applied Physics*, vol. 109, no. 8, pp. 084319.

Misra, A., Mitra, A., and Thareja, R.K., 1999, "Diagnostics of laser ablated plasmas using fast photography", *Applied Physics Letters*, vol. 74, no. 7, pp. 929-931.

Mitchner, M., and Kruger, C.H., 1973, *Partially Ionized Gases*, John Wiley and Sons Inc., pp. 58.

Morozov, A.A., 2004, "Thermal model of pulsed laser ablation: back flux contribution", *Applied Physics A: Materials Science & Processing*, vol. 79, no. 4, pp. 997-999.

Müller, G., Konijnenberg, M., Krafft, G., and Schultheiss, C., 1995, "Thin film deposition by means of pulsed electron beam ablation" in *Science and Technology of Thin Films*, eds. F.C. Matacotta and G. Ottaviani, World Scientific, Singapore, pp. 89-119.

Müller, G., and Schultheiss, C., 1994, "Deposition by means of pulsed electron beam ablation" in *10th International Conference on High-Power Particle Beams*, San Diego, 2, pp. 833-836.

Nakanishi, Y., Miyake, A., Kominami, H., Aoki, T., Hatanaka, Y., and Shimaoka, G., 1999, Preparation of ZnO thin films for high-resolution field emission display by electron beam evaporation", *Applied Surface Science*, vol.142, no.1-4, pp. 233-236.

Namba, S., Nozu, R., and Takiyama, K., 2006, "Spectroscopic study of ablation and recombination processes in a laser-produced ZnO plasma", *Journal of Applied Physics,* vol. 99, no. 7, pp. 073302.

Neamtu, J., Mihailescu, I.N., Ristoscu, C., and Hermann, J., 1999, "Theoretical modelling of phenomena in the pulsed–laser deposition process: Application to Ti targets ablation in low-pressure N_2", *Journal of Applied Physics*, vol. 86, no. 11, pp. 6096-6106.

Nishiwaki, M., and Kato, S., 2005, "Study on secondary electron emission from carbon materials", *Journal of the Vacuum Society of Japan,* vol. 48, no. 3, pp. 118-120.

Nistor, M., Manadache, N.B., and Perrière, J., 2008, "Pulsed electron beam deposition of oxide thin films", *Journal of Physics D: Applied Physics,* vol. 41, no. 16, pp. 165205.

Nistor, M., Gherendi, F., and Manadache, N.B., 2011, "Fast imaging of ablation plasma produced by a pulsed electron beam", *IEEE Transactions on Plasma Science*, vol. 39, no. 11, pp. 2800-2801.

Null, M.R., Lozier, W.W., and Moore, A.W., 1973, "Thermal diffusivity and thermal conductivity of pyrolytic graphite from 300 to 2700 K", *Carbon,* vol. 11, no. 2, pp. 81-87.

Pappis, J., and Blum, S.L., 1961, "Properties of pyrolytic graphite", *Journal of the American Ceramic Society,* vol. 44, no. 12, pp. 592-597.

Pattini, F., Bronzoni, M., Mezzadri, F., Bissoli, F., Gilioli, E., and Rampino, S., 2013, "Dynamics of evaporation from $CuGaSe_2$ targets in pulsed electron deposition technique", *Journal of Physics D: Applied Physics,* vol. 46, no. 24, pp. 245101.

Pert, G.J., 1989, “Two-dimensional hydrodynamic models of laser–produced plasmas”, *Journal of Plasma Physics,* vol. 41, no. 2, pp. 263-280.

Peterlongo, A., Miotello, A., and Kelly, R., 1994, “Laser-pulse sputtering of aluminum: Vaporization, boiling, superheating, and gas-dynamics effects”, *Physical Review E,* vol. 50, no. 6, pp. 4716-4727.

Pierson, H.O., 1994, *Handbook of Carbon, Graphite, Diamonds and Fullerenes: Processing, Properties and Applications*, Noyes Publications, New Jersey, pp. 43.

Ptitsin, V.E., 2012, “On the theory of the electron beam ablation phenomenon”, *Physica Status Solidi C*, vol. 9, no. 1, pp. 15-18.

Proskurovsky, D.I., Rotshtein, V.P., Ozur, G.E., Markov, A.B., Nazarov, D.S., Shulov, V.A., Ivanov, Y.F., and Buchheit, R.G., 1998, “Pulsed electron-beam technology for surface modification of metallic materials”, *Journal of Vacuum Science and Technology A,* vol. 16, no. 4, pp. 2480-2488.

Qin, Y., Dong, C., Wang, X., Hao, S., Wu, A., Zou, J., and Liu, Y., 2003, “Temperature profile and crater formation induced in high-current pulsed electron beam processing”, *Journal of Vacuum Science & Technology A,* vol. 21, no. 6, pp. 1934-1938.

Qin, Y., Zou, J., Dong, C., Wang, X., Wu, A., Liu, Y., Hao, S., and Guan, Q., 2004, “Temperature-stress fields and related phenomena induced by a high current pulsed electron beam”, *Nuclear Instruments and Methods in Physics Research Section B: Beam Interactions with Materials and Atoms,* vol. 225, no. 4, pp. 544-554.

Ready, J.F., 1971, *Effects of High-Power Laser Radiation*, Academic Press, New York.

Reichelt, K., 1988, “Nucleation and growth of thin films”, *Vacuum,* vol. 38, no. 12, pp. 1083-1099.

Reynolds, W.N., 1968, *Physical Properties of Graphite*, Elsevier Publishing Co. Ltd., New York.

Rozman, R., Grabec, I., and Govekar, E., 2008, “Influence of absorption mechanisms on laser-induced plasma plume”, *Applied Surface Science,* vol. 254, no. 11, pp. 3295-3305.

Schiller, S., Heisig, U., and Panzer, S., 1982, *Electron beam technology,* John Wiley & Sons., New York, pp. 29.

Schou, J., Amoruso, S., and Lunney, J.G., 2007, "Plume Dynamics" in *Laser Ablation and its Applications*, ed. C. Phipps, Springer, New York, pp. 67-95.

Singh, R.K., Holland, O.W., and Narayan, J., 1990, “Theoretical model for deposition of superconducting thin films by using pulsed laser evaporation technique”, *Journal of Applied Physics,* vol. 68, no. 1, pp. 233-247.

Singh, R.K., and Narayan, J., 1990, “Pulsed-laser evaporation technique for deposition of thin films: Physics and theoretical model”, *Physical Review B,* vol. 41, no. 13, pp. 8844-8859.

Stafe, M., Negutu, C. and Popescu, I.M., 2007, “Theoretical determination of the ablation rate of metals in multiple-nanosecond laser pulses irradiation regime”, *Applied Surface Science,* vol. 253, no. 15, pp. 6353-6358.

Stapleton, M.W., McKiernan, A.P., and Mosnier, J.-P., 2005, “Expansion dynamics and equilibrium conditions in a laser ablation plume of lithium: Modeling and experiment”, *Journal of Applied Physics,* vol. 97, no. 6, pp. 064904.

Steinbeck, J., Braunstein, G., Dresselhaus, M.S., Venkatesan, T., and Jacobson, D.C., 1985, A model for pulsed laser melting of graphite, *Journal of Applied Physics*, vol. 58, no. 11, pp. 4374-4382.

Strikovski, M., and Harshavardhan, K.S., 2003, “Parameters that control pulsed electron beam ablation of materials and film deposition processes”, *Applied Physics Letters*, vol. 82, no. 6, pp. 853–855.

Strikovski, M., Kim, J., and Kolagani, S.H., 2010, "Plasma Energetics in Pulsed Laser and Pulsed Electron Deposition" in *Springer Handbook of Crystal Growth*, eds. G. Dhanaraj, K. Byrappa, V. Prasad and M. Dudley, Springer-Verlag, Berlin Heidelberg, pp. 1193-1211.

Thareja, R.K., Dwivedi, R.K., and Abhilasha, 1997, “Role of ambient gas on laser-ablated plumes for thin carbon film deposition”, *Physical Review B*, vol. 55, no. 4, pp. 2600-2605.

Tokarev, V.N., Lunney, J.G., Marine, W., and Sentis, M., 1995, “Analytical thermal model of ultraviolet laser ablation with single-photon absorption in the plume”, *Journal of Applied Physics*, vol. 78, no. 2, pp. 1241-1246.

Tricot, S., Boulmer-Leborgne C., Nistor, M., Million, E., and Perrière, J., 2008, “Dynamics of a pulsed-electron beam induced plasma: application to the growth of zinc oxide thin films”, *Journal of Physics D: Applied Physics*, vol. 41, no. 17, pp. 175205.

Tricot, S., Semmar N., Lebbah, L., and Boulmer-Leborgne C., 2010, “ZnO sublimation using a polyenergetic pulsed electron beam source: numerical simulation and validation”, *Journal of Physics D: Applied Physics*, vol. 43, no. 6, pp. 065301.

Venkatesan, T., Harshavardhan, K.S., Strikovski, M., and Kim, J., 2005, "Recent advances in the deposition of multi-component oxide films by pulsed energy deposition" in *Thin Films and Heterostructures for Oxide Electronics*, eds. S.B. Ogale, Springer, New York, pp. 385-413.

Venkatesan, T., Jacobson, D.C., Gibson, J.M., Elman, B.S., Braunstein, G., Dresselhaus, M.S., and Dresselhaus, G., 1984, "Measurement of thermodynamic parameters of graphite by pulsed-laser melting and ion channeling", *Physical Review Letters*, vol. 53, no. 4, pp. 360–363.

Voreades, D., 1976, "Secondary electron emission from thin carbon films", *Surface Science*, vol. 60, no. 2, pp. 325–348.

Witke, T., Lenk, A., Schultrich, B., and Schultheiss, C., 1995, "Investigation of plasma produced by laser and electron pulse ablation", *Surface and Coatings Technology*, vol. 74-75, no. 1, pp. 580–585.

Witke, T., Lenk, A., and Schultrich, B., 1996, "Investigation of plasma produced by electron pulse ablation", *IEEE Transactions on Plasma Science*, vol. 24, no. 1, pp. 61-62.

Wood, R.F., and Giles, G.E., 1981, "Macroscopic theory of pulsed–laser annealing. I. Thermal transport and melting", *Physical Review B,* vol. 23, no. 6, pp. 2923-2942.

Wasa, K., Kitabatake, M., and Adachi, H., 2004, *Thin Film Materials Technology: Sputtering of Compound Materials,* William Andrew Inc., Norwich, pp. 18-33.

Xie, J., and Kar, A., 1997, "Mathematical modeling of melting during laser materials processing", *Journal of Applied Physics,* vol. 81, no. 7, pp. 3015-3022.

Xu, X., Grigoropoulos, C.P., and Russo, R.E., 1995, "Heat transfer in excimer laser melting of thin polysilicon layers", *Journal of Heat Transfer,* vol. 117, no. 3, pp. 708-715.

Zazula, J.M., 1997, "On graphite transformation at high temperature and pressure induced by absorption of the LHC beam", Tec. Rep. LHC Project Note 78, CERN, Geneva, pp. 1-14.

Zel'dovich, Y.B., and Raizer, Y.P., 1966, *Physics of Shock Waves and High-Temperature Hydrodynamic Phenomena*, Academic Press Inc., New York, vol. 1, pp. 69-75.

Zhang, W., Yao, Y.L., and Chen, K., 2001, "Modelling and analysis of UV laser micromachining of copper", *The International Journal of Advanced Manufacturing Technology*, vol. 18, no.5, pp. 323-331.

Zhijian, L., Xiaoyun, L., Xingliu, J., and Lijun, H., 2005, "Preparation of nanometer thin films with intense pulsed electron beam ablation", *Surface and Coatings Technology*, vol. 193, no.1-3, pp. 325-328.

Zou, J., Zhang, K., Dong, C., Qin, Y., Hao, S., and Grosdidier, T., 2006, "Selective surface purification via crater eruption under pulsed electron beam irradiation", *Applied Physics Letters*, vol. 89, no. 4, pp. 041913.

Zweig A.D., 1991, "A thermomechanical model for laser ablation", *Journal of Applied Physics*, vol. 70, no. 3, pp. 1684-1691.